UNIVERSITY OF OKLAHOMA

GRADUATE COLLEGE

ANALYSIS OF TORNADIC SUPERCELLS USING TWO RAPID-SCAN, MOBILE DOPPLER RADARS

A THESIS

SUBMITTED TO THE GRADUATE FACULTY

in partial fulfillment of the requirements of the

Degree of

MASTER OF SCIENCE IN METEOROLOGY

By

TREY A. GREENWOOD
Norman, Oklahoma
2021

ANALYSIS OF TORNADIC SUPERCELLS USING TWO RAPID-SCAN, MOBILE DOPPLER RADARS

A THESIS APPROVED FOR THE

SCHOOL OF METEOROLOGY

BY THE COMMITTEE CONSISTING OF

Dr. Howard B. Bluestein, Chair

Dr. Naoko Sakaeda

Dr. Jeffrey C. Snyder

Dr. Louis J. Wicker

Acknowledgments

First, I would like to thank my mom and dad for their unwavering love and support, not just during my time at the University of Oklahoma, but throughout my entire life. From the moment I first fell in love with weather, they provided an atmosphere that fostered the growth of my weather knowledge, from providing me a collection of VHS tapes on hurricanes and tornadoes to listening intently as I impersonated Gary England providing severe weather coverage in front of the television. Even though my storm chasing yields numerous sleepless nights for them, they have only supported me to pursue my passion for severe weather, and I am extremely fortunate to have such loving parents.

I would also like to thank my friends for their support during this process. Cookouts and almost daily (pre-Coronavirus) basketball sessions with fellow School of Meteorology students Ryan Bunker, Jordan Laser, Ty Dickinson, Jacob Ohnstad, Kevin Thiel, Tyler Young, and Noah Brauer helped me blow off steam and remain sane during the school and thesis grind. My storm chasing friends Alec Scholten, Alexa Boswell, Micah Hart, Adri Mozeris, Max Olson, Stephen Jones, Brandi Dittrich, Kristen Pence, and Ethan Mofidi (to name just a few) are like a second family to me and made my transition to Oklahoma life a smooth one. Our weekly game nights, golf and tennis

matches, and, of course, expeditions to faraway places to track down tornadoes and hurricanes helped alleviate the stress of being a graduate student, for which I am thankful.

I am incredibly grateful to my advisor, Dr. Howie Bluestein, for giving me a chance to work for him. One of the VHS tapes I watched over and over again when I was little was a National Geographic documentary called *Cyclone*, which featured Dr. Bluestein and his fieldwork during the 1991 tornado season. I never thought I would go from a kid interested in tornadoes who looked up to Dr. Bluestein to a graduate student working for and studying tornadoes with him. I have enjoyed every one of our discussions, research meetings, and expeditions in RaXPol, as I am able to soak up bits and pieces of his immense meteorological knowledge and listen to his stories of successful storm chases past. Thank you, Dr. Bluestein, for giving me this opportunity, for being such an understanding advisor, and for helping me fulfill a lifelong goal.

In addition, I would like to thank my committee members, Drs. Naoko Sakaeda, Lou Wicker, and Jeff Snyder, for their willingness to be a part of my committee and for their help in this process. I very much appreciated our discussions and their constructive feedback, which helped make this a better thesis. Also, thank you to Dr. Snyder and Dr. Jana Houser of Ohio University for providing me with some of the radar data and key software programs that I used in this thesis.

My officemates and fellow Bluestein graduate students Zach Wienhoff (now at the University of Illinois) and Dylan Reif have made my research and time at OU much easier and more enjoyable. From taking time to teach me the ins and outs of RaXPol to being so open to helping me and answering my questions, Zach and Dylan have been

incredible resources in this process, and I would not have been able to complete a good portion of this thesis without their help. In addition, our daily conversations on topics from tornadoes to classes to sports, often with fellow officemate Ryan Pajela, always helped me get through the tedious process of unfolding radar data.

The work presented in this thesis was supported by National Science Foundation grants AGS-1262048, AGS-1560945, and AGS-1947146.

Table of Contents

List of Tables

List of Figures

Abstract

Mobile Doppler radar is a critical tool in studying microscale phenomena, including tornadoes, in supercell thunderstorms at close-range. However, a relative dearth of high-quality cases documenting the tornadic life cycle has hindered the advancement of our understanding of tornado evolution, storm-scale processes related to tornadogenesis and decay, and why some supercells produce tornadoes and others do not. Four tornadic events occurred in Oklahoma during the springs of 2015 and 2019, each documented by either the Mobile Weather Radar, 2005 X-Band, Phased Array (MWR-05XP), the Rapid X-band Polarimetric (RaXPol) radar, or both. In this study, these cases will be thoroughly analyzed with emphasis on the following points:

a. Tornadogenesis and decay (whether the tornado vortex signature (TVS) builds upward or downward with time) when applicable,
b. how the TVS as a function of height evolves over time,
c. vortex tilt as a function of height and its evolution over time, and
d. any unique features evident in the data, particularly those that yielded changes to the behavior of the vortex or that have rarely been documented in previous studies.

Among the four cases, both descending and nondescending tornadogenesis were documented, as was "inside-out" decay, as described in French et al. (2014) and Houser et al. (2015). A majority of the tornadic vortices were highly tilted; vortex tilt was compared to the environmental hodograph (either modeled or observed) in close proximity to each parent supercell, a technique that, to the author's knowledge, has not been employed previously. In addition, several interesting features were noted, including tornado debris signatures and weak-echo columns (the characteristics and behavior of which will be discussed), and the majority of the supercells exhibited subtornadic vortices that were, generally, only apparent aloft and displayed unique behavior.

Chapter 1

Introduction

The tornado is one of the most destructive phenomena on Earth. Every year, the United States averages over 1000 tornadoes (Grazulis 1993), the most damaging of which generate individual losses in excess of $1 billion (Brooks and Doswell 2001). In fact, between 1997 and 2016, tornadoes accounted for 39.9 percent of all insured catastrophe losses (Gunturi and Tippett 2017). Additionally, tornadoes kill approximately 60 people per year in the United States (Ashley 2007). These statistics provide impetus to improve how we study tornadoes and determine why one storm produces a tornado while another storm in a similar environment does not.

Mobile Doppler radar is a critical tool used to observe severe thunderstorms and help meteorologists understand the processes that create tornadoes. Prior to mobile Doppler radar, meteorologists relied on the National Weather Service's network of fixed-site radars to construct a clear picture of tornadogenesis in supercells. This was insufficient for multiple reasons: 1) near-surface data are virtually impossible to obtain from a fixed-site radar due to Earth's curvature and beam blockage from topography, vegetation, and structures (Wurman et al. 1997), and 2) a radar's beam spreads out as distance from the radar increases, deeming some important phenomena in radar-distant

supercells undetectable (Bluestein 2007). Only 0.1% of the NEXRAD network's coverage area can appreciably resolve near-surface, microscale phenomena[1] (Wurman et al. 1997). As a result, the need arose for portable radars that could be deployed in the vicinity of tornadic supercells, first espoused by Zrnic et al. (1985) and carried out by Bluestein and Unruh (1989), who used a portable, low-powered, 3-cm-wavelength (X-band) Doppler radar to collect data from severe convective storms from 1987-88. This radar, which was developed by the Los Alamos National Laboratory (LANL) for non-meteorological applications, collected complex time series data which were then converted into audio signals that indicated to radar operators which parts of the storm contained areas of interest. Despite its 5° beamwidth and resultant low azimuthal resolution, it was able to detect approaching and receding wind velocities coincident with cyclonic circulations in supercells, as well as dust and debris associated with a wall cloud or tornado. Thus, this preliminary fieldwork proved the practicality of transporting a portable radar and taking useful measurements near tornadic supercells.

During the spring of 1990 and 1991, Bluestein et al. (1993) deployed the LANL radar near six mesocyclonic tornadoes in the Southern Great Plains, including a long-track, F4 tornado near Red Rock, OK, on 26 April 1991. Winds of 120-125 m s^{-1} were documented in this tornado, which are likely the first measurements of F5 wind speeds ever made by a Doppler radar. Several relative maxima were also present in the wind spectra for the Red Rock tornado, which may have been manifestations of suction

[1] "Near-surface, microscale phenomena" are those on a scale of 100 m and within 100 m of the ground, which is the minimum resolution needed to resolve tornadic phenomena (Wurman et al. 1997), depending on the criteria used to define a tornadic vortex.

vortices within the parent tornado. In addition, several key findings emerged from these cases: 1) In most of the datasets, measured winds exceeded the thermodynamic speed limit—a hypothetical maximum tornado wind speed which assumes that the convective available energy (CAPE) is converted to a maximum wind speed using cyclostrophic balance, 2) observed tornadoes had strong winds even during their decay phase, and 3) the maximum radar reflectivity was well outside the radius of maximum wind in supercellular tornadoes, perhaps due to debris centrifuged out from a tornado's center or precipitation surrounding the vortex.

To address the need for a more sensitive radar when a tornado's condensation funnel or most intense portion consists of mostly small cloud droplets, Bluestein et al. (1995) tested the University of Massachusetts (UMass) W-band (3-mm-wavelength), pulsed Doppler radar near severe convective storms during the spring of 1993 and 1994. Its shorter wavelength yielded a much smaller beamwidth (0.7°) than the LANL radar, resulting in much greater spatial resolution and increased sensitivity to smaller targets. The radar was mounted inside of a University of Oklahoma (OU) van with the antenna protruding from a hatch in the roof; as a result, the radar could not operate in excessive precipitation. On 7-8 May 1993 and 25 May 1994, the radar operators intercepted tornadoes but could not collect any data because heavy rain was falling at the intercept location and/or the tornado was obscured by heavy precipitation. However, data was successfully collected on a low-precipitation supercell near Morton, TX, on 5 June 1993 and a mesocyclone at the intersection of two squall lines in Central Oklahoma on 9 June 1993. At the time, these were the highest-resolution datasets of severe convective storms

ever obtained, and they proved that the UMass W-band radar could be a valuable tool for studying supercellular tornadoes.

Detailed in Wurman et al. (1997), the first truck-mounted, X-band radar for studying severe convective storms was the Doppler on Wheels (DOW), which featured a 3-cm wavelength, pencil-beam, pulsed Doppler radar affixed to the bed of a light-duty panel truck. The DOW was initially deployed in 1995 during the Verification of the Origins of Rotation in Tornadoes Experiment (VORTEX), a two-year project that sought to test several new hypotheses on tornadogenesis and tornado dynamics using a fleet of upper-air and surface observation platforms, as well as mobile and airborne Doppler radars (Rasmussen et al. 1994). The UMass W-band radar discussed above was also a part of this project, collecting extremely fine-scale data of counterrotating vortices within a supercell's rear-flank downdraft on 17 May 1995 (Bluestein et al. 1997). On 2 June 1995, the DOW gathered data during the mature and dissipation stages of a violent tornado near Dimmitt, TX (Wurman et al. 1996). Several features coincident with the tornado were resolved, including a well-defined velocity couplet and a low-level weak-echo region surrounded by a region of enhanced reflectivity consistent with the extent of the observed debris cloud. Multiple semi-concentric to concentric rings surrounding the weak-echo region were evident with increasing elevation. Also, the data yielded evidence of a downdraft near the center of the tornado. Using these findings, Wurman and Gill (2000) provided the first direct comparison of wind measurements from a high-resolution, mobile Doppler radar to ratings from the damage-based Fujita Scale. This

built on the conclusions of Bluestein et al. (1993) and continued to prove the utility of mobile Doppler radar for studying tornadic supercells.

On 30 May 1998, the DOW collected close-range data from a supercell tornado that produced F4 damage in Spencer, SD (Alexander and Wurman 2005). Tornado-strength winds were detected at least 180 s prior to the appearance of a tornado debris cloud, suggesting that damaging tornadic surface winds may appear well before a debris cloud or condensation funnel develops. In addition, velocity data illustrated that variations in tornado wind speed as a function of height were most obvious in the lowest 200 m above ground level (AGL), and the highest wind speeds in the vortex existed in the lowest 50 m AGL with a potential decrease in wind speed below 30 m AGL. Wurman and Alexander (2005) compared DOW data to damage survey findings and determined that the tornado's wind field was asymmetric, exhibiting wind speeds 30 m s^{-1} higher on the right side of the tornado due to effects from the horizontal translation of the vortex. These data also provided the first direct evidence of sub-tornado-scale wind maxima within a parent tornadic circulation, likely caused by multiple vortices.

On 3 May 1999, a major outbreak of tornadic supercells occurred across Kansas and Oklahoma, highlighted by a long-track tornado that began near Amber, OK, and produced F5 damage in Bridge Creek and Moore, OK (Speheger et al. 2002). Both the DOW and the UMass W-band radar obtained data from this event (Burgess et al. 2002, Bluestein and Pazmany 2000). The UMass W-band radar collected multiple sector scans of an F3 tornado southeast of Verden, OK, the parent circulation of which would later produce the aforementioned Bridge Creek-Moore F5 tornado. The reflectivity data

exhibited a hurricane-like eye and spiral bands, supporting the findings of Wurman et al. (1996), and several wavelike features coincident with small-scale velocity couplets existed in the tornado's eyewall, suggesting the possibility of subvortices rotating around the main tornado vortex. Similarly, the DOW collected data on the Bridge Creek-Moore F5 tornado, which also exhibited an eye of weaker reflectivity surrounded by a ring of much stronger reflectivity. Because the DOW remained in motion while data was being collected, low-level velocity data was degraded in several volume scans; despite this, analysis of the velocity data revealed wind speeds slightly less than those that were determined through damage surveys. Several hours after the Bridge Creek/Moore F5, the DOW gathered data from another large, violent tornado near Mulhall, OK, in which Wurman (2002) analyzed numerous subvortices that featured annular or hook-shaped regions of reflectivity surrounding a clear eye, similar to the parent tornado. However, unlike the parent tornado, intense shear was concentrated in a small region at the center of most of the vortices, perhaps caused by the rapid tangential motion of the vortices or small-scale, transient updrafts. The vertical vorticity of these features, estimated to be 4-8 s^{-1}, were the highest ever measured in tornadic flows.

Tornadic phenomena evolve on the order of seconds; however, the National Weather Service's fixed-site Weather Surveillance Radar-1988 Doppler (WSR-88D) and the aforementioned mobile Doppler radars employ a mechanically rotating antenna atop a pedestal, which, together, are unable to complete volume scans at such fine temporal resolution. To address this issue, phased array radar was developed. In contrast to traditional radar that uses a rotating antenna, phased array radar uses an array of antennae

that can be steered electronically without moving the antennae, which increases the temporal resolution from about four minutes to less than a minute (Zrnic et al. 2007). This groundbreaking technology was soon introduced to the mobile radar arena with the construction of the Meteorological Weather Radar 2005 X-band Phased Array (MWR-05XP), which features a military phased array radar that can complete a volume scan up to 20° in elevation in approximately 25 seconds. The MWR-05XP underwent field testing on numerous severe convective storms, including tornadic and nontornadic supercells, from 2007-08, and it was found to successfully collect rapid-scan, storm-scale data, particularly in rapidly evolving tornadic supercells (Bluestein et al. 2010). The specifications and operating modes of the MWR-05XP will be discussed in greater detail in Chapter 2.

In 2009-10, the second VORTEX field campaign (VORTEX2) took place across the Great Plains. According to Wurman et al. (2012), the main goals of VORTEX2 were to improve our understanding of tornadogenesis and evolution, the environmental characteristics that support tornado maintenance, the low-level wind field in tornadoes and how it relates to damage, and how supercells and tornadoes should be modeled. To achieve these goals, a myriad of mobile observing platforms were employed, including a fleet of mobile mesonets, ground-based instrument probes, and multiple mobile radars, including the MWR-05XP.

The most comprehensively studied VORTEX2 case featured a supercell that produced a long-lived, strong tornado in Goshen County, WY, on 5 June 2009; data from multiple sources were collected from well before the tornado formed through its

dissipation. MWR-05XP and DOW data illustrate that, just prior to tornadogenesis, the supercell's rear-flank downdraft (RFD) intensified, followed by the formation of a secondary rear-flank gust front (RFGF), which stretched to the south and west of the low-level circulation and wrapped cyclonically around the vortex (Kosiba et al. 2013). Changes in intensification of the tornado vortex during tornadogenesis were closely tied to changes in the magnitude of the secondary RFD. Similar to previously observed supercells (Byko et al. 2009), the intensification of low-level rotation was accompanied by a descending reflectivity core (DRC), first described by Rasmussen et al. (2006) as an area of enhanced reflectivity that descends from the rear of the overhanging echo on the rear side of the weak-echo region of a supercell. In this case, a region of enhanced reflectivity formed between 4-7 km AGL just to the west of the main updraft and proceeded to descend in the area between the RFD and the backside of the updraft, within the hook echo (Markowski et al. 2012a). Subsequently, a weak-echo eye formed, coincident with the incipient tornado. In addition, the high-resolution radar data captured a thin band of very low reflectivity bifurcating the forward and rear flanks of the Goshen County supercell, as well as a few other supercell cases during VORTEX2 (Wurman et al. 2012, Snyder et al. 2013, Griffin et al. 2018). This previously undiscovered phenomenon was named the "low-reflectivity ribbon" (LRR). In the Goshen County storm, the LRR became more pronounced immediately antecedent to tornadogenesis, although air parcels feeding the tornado passed near but not through the LRR.

Despite the MWR-05XP's numerous advantages for studying severe convective phenomena, the development of dual polarization technology led scientists to consider

other alternatives. Most dual-polarization radars simultaneously emit radio waves with horizontal and vertical orientation, unlike typical radars that emit only horizontally polarized waves. As a result, they can determine the size, shape, and type of hydrometeors within a storm and can even detect tornado debris (Zrnic and Rhyzkov 1999, Bluestein et al. 2007). In turn, the Rapid X-band Polarimetric (RaXPol) radar became operational in 2011. RaXPol employs a truck-mounted, rotating antenna with dual polarization capability but, unlike traditional radars, uses a heavy-duty pedestal that can support a scanning rate of 180° s^{-1}. Therefore, it can complete a 10-elevation-angle volume scan in approximately 20 seconds, comparable to the MWR-05XP (Pazmany et al. 2013). The specifications and operating modes of RaXPol will be discussed in greater detail in Chapter 2.

Since its inception, RaXPol has proven successful at capturing high-resolution data of tornadoes. On 24 May 2011, RaXPol captured the entire life cycle of an EF3 tornado and the genesis and maturation of a subsequent tornado, rated EF5, near El Reno, OK. Houser et al. (2015) found that the EF3 tornado did not decay monotonically; instead, Δv_{max}—the difference between the maximum outbound and maximum inbound velocity measurements within a tornado vortex signature (TVS)—initially decreased rapidly and concurrently over the depth of the data before increasingly slightly above 3 km. Δv_{max} at all heights then decreased to subtornadic intensity within 30 s. This evolution suggested that processes modulating both tornado decay and intensification can occur simultaneously and that decay may not be a constant process. Furthermore, a surge in the parent supercell's RFGF helped initiate the dissipation of the EF3 tornado via

occlusion, and a SRFGF surge aided in the formation of the subsequent EF5 tornado whose mesocyclone likely developed from an updraft pulse associated with forced ascent along the SRFGF. Houser et al. (2015) did not find evidence that the TVS descended from the storm's midlevels as in French et al. (2013); instead, the vortex intensified simultaneously over the depth of the data above an area of pre-existing low-level vorticity. This opposed previous observations and hypotheses (e.g., Burgess et al. 1975, Brown et al. 1978) that a tornado forms when the vortex descends from the midlevels of a supercell.

1.1 Our Current Understanding of the Tornado Life Cycle

Tornadogenesis is a complex, scale-interactive process, one that meteorologists have yet to fully understand despite advances in technology. Only about one-quarter of supercells are tornadic; however, nearly all significant (EF-2+) tornadoes are associated with supercells (Trapp et al. 2005, Markowski and Richardson 2009). Supercells obtain their storm-scale rotation from the tilting of horizontal vorticity associated with ambient vertical wind shear. In general, veering and strengthening winds with height support supercells, and the degree of low-level wind shear can discriminate between tornadic and nontornadic supercells (Grams et al. 2012). Low-level wind shear can come from the environment or be generated in situ along baroclinic zones, such as a supercell's forward-flank downdraft (FFD) gust front. It also creates near-surface horizontal vorticity, which is "streamwise" if the horizontal vorticity vector ($\boldsymbol{\omega_h}$) is parallel to the storm-relative wind vector and "crosswise" if $\boldsymbol{\omega_h}$ is orthogonal to the storm-relative wind vector at a

given height (Davies-Jones 1984). Streamwise vorticity ingestion is most favorable for persistent updraft rotation and tornadogenesis in supercells. If an updraft coincides with a tube of near-surface, horizontal streamwise vorticity, that tube can be tilted and stretched in the vertical, allowing the updraft to rotate (Grazulis 2001).

In the absence of adequate vertical vorticity near the ground, a downdraft is key in advecting vertical vorticity to the surface, where it can be stretched into a tornado (Markowksi and Richardson 2009). When midlevel air collides with a supercell, it stagnates and is forced downward at the storm's rear (Barnes 1978); this process results in the formation of the RFD and provides the downdraft needed for tornadogenesis in the absence of near-surface vertical vorticity. Brandes (1981) and Klemp et al. (1981) hypothesized that the RFD is a product of negative buoyancy that results from water loading and precipitation evaporation aloft. In addition, Klemp and Rotunno (1983) postulated that, if the mesocyclone decreases in intensity with height (i.e. the speed of rotation decreases with height), a downward-directed component of the pressure gradient force (PGF) produces a more focused "occlusion downdraft." Shown in Fig. 1.1, the supercell's mesocyclone—a concentrated area of strong rotation within the broader rotating updraft—may manifest itself at cloud base via a wall cloud, located at the interface between the rain-free updraft base and the forward-flank precipitation core. The juncture between the RFD gust front and the FFD baroclinic zone is the most common location for tornado formation when coincident with the mesocyclone (see Fig. 1.2; Klemp 1987, Grazulis 2001).

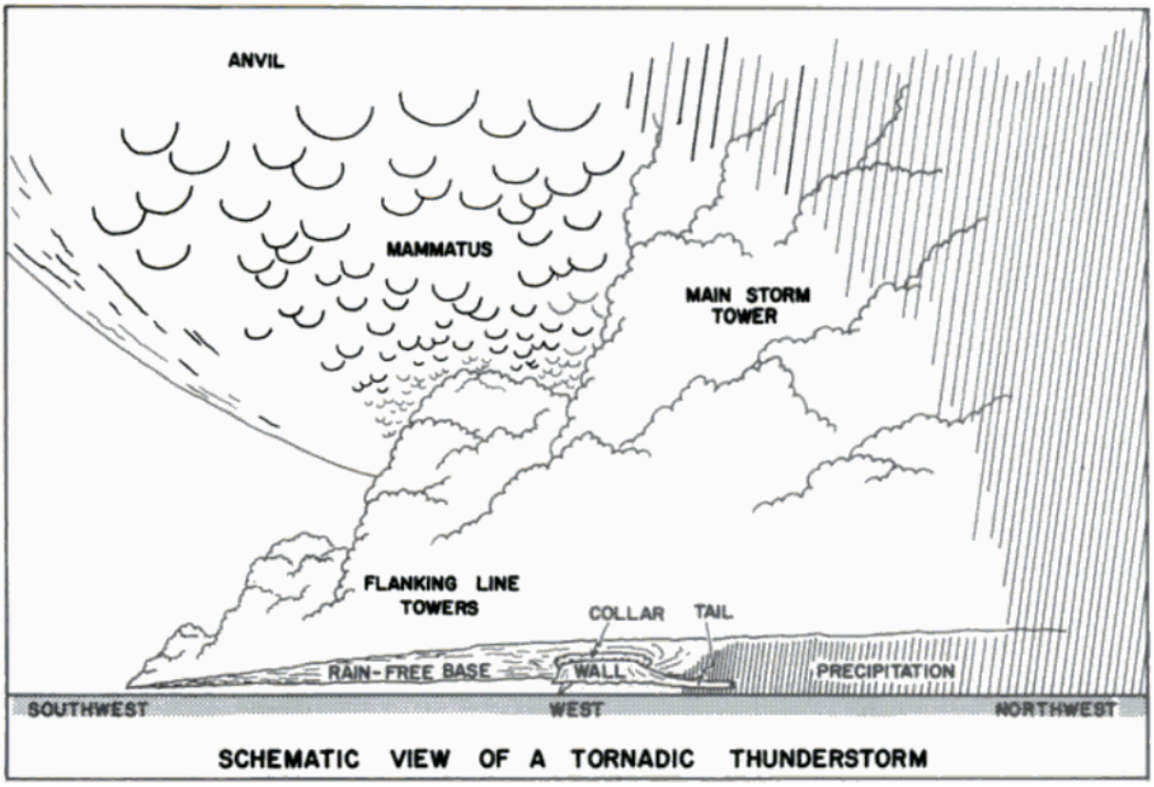

Figure 1.1: Schematic view of a supercell thunderstorm as drawn by Charles Doswell and Joseph Golden. Adapted from Grazulis (2001).

1.1.1 The Vertical Evolution of the TVS during Tornadogenesis

In recent years, the question of whether or not tornadogenesis begins at the surface and builds upward or descends from a storm's midlevels has arisen. Laboratory simulations by Leslie (1971) suggested that as cyclostrophic balance is achieved at the midlevels of a supercell, low pressure initially develops in the center of the mesocyclone aloft. Due to an upward-directed pressure gradient force, air begins to flow into the mesocyclone, cyclonically, at lower levels. Subsequently, the mesocyclone builds downward toward the surface until the effects of surface friction concentrate the cyclonic flow even further, generating a tornado. This process is called the "dynamic pipe effect" (DPE). These processes build downward, and a concentrated tornadic vortex

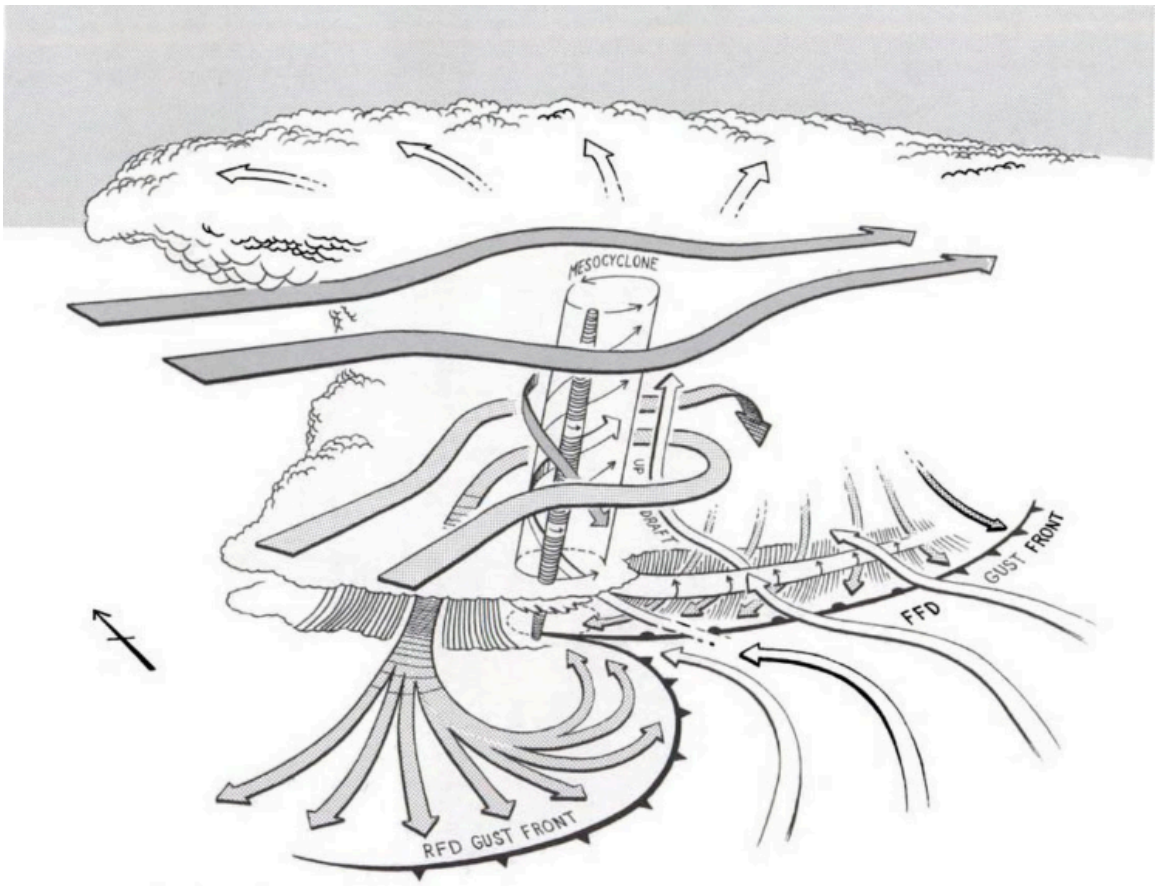

Figure 1.2: Schematic view of the airflow in and around a supercell thunderstorm as drawn by David Hoadley. Adapted from Grazulis (2001).

descends to the surface, where it rapidly strengthens before attaining a quasi-steady state. Burgess et al. (1975) and Brown et al. (1978) used Doppler radar observations of the 24 May 1973 Union City, OK, tornadic supercell to support this idea. However, Trapp and Davies-Jones (1997) found, using a numerical model, that DPE is only required for tornadogenesis when buoyancy is confined to midlevels, in which case air parcels with high angular momentum approach closest to the axis of the mesocyclone at its midlevels. As a result, the tornado vortex forms aloft and then descends to the surface through DPE. However, when ample buoyancy exists at low levels, air parcels that nearly conserve angular momentum approach the mesocyclone axis over a deeper layer, including the low

levels. In turn, the tornado vortex develops simultaneously at mid- and low-levels without DPE. Furthermore, Trapp et al. (1999) studied WSR-88D data of 52 tornadogenesis events and found that only 52% of these featured descending tornadogenesis, while the remaining 48% featured TVSs that were either first detected near the surface and built upward or appeared simultaneously over a significant depth.

Several studies using mobile Doppler radar data have lent credence to the hypothesis that tornadoes form near the ground and build upward. French et al. (2013) examined MWR-05XP data from the 2011 El Reno case, discussed above, as well as two other events: the Ellis-Plainsville, KS, tornado on 23 May 2008 and the aforementioned Goshen County, WY, tornado on 5 June 2009. In each of these cases, the TVS propagated upward with time, first identified near the surface before becoming apparent in midlevels. This study also suggests that DPE cannot occur in vortices that repeatedly form and dissipate; instead, only vortices that are continuous in height and time can build downward through DPE. In addition, Bluestein et al. (2019) utilized RaXPol data to determine that the TVS associated with the beginning stages of a large, violent tornado near El Reno, OK, on 31 May 2013 began near the ground and built upward in discrete bursts. Based on the analysis techniques of Rotunno and Klemp (1985) and in concert with the hypothesis proposed by Wicker and Wilhelmson (1995), the mesocyclone appears to have increased in intensity with height, leading to an upward-directed component of the pressure gradient force that, in turn, induced upward motion below the mesocyclone, augmenting tornadogenesis, during which the TVS built rapidly upward within one volume scan (approximately 20 s).

1.1.2 Selected Radar Signatures Associated with Tornadic Supercells

1.1.2.1 Differential Reflectivity Arc

The differential reflectivity (Z_{DR}) arc is a feature prevalent in right-moving supercells and is often a harbinger to tornadogenesis (Kumjian and Ryzhkov 2008). Z_{DR} is a logarithmic ratio of horizontally polarized radar reflectivity factor to vertically polarized radar reflectivity factor (Kumjian 2013); therefore, positive values of Z_{DR} indicate scatterers whose scattering cross-sections[2] are greater at horizontal polarization than vertical polarization. This generally indicates hydrometeors that are larger in the horizontal than the vertical, while the opposite is true for negative Z_{DR} values. As storm-relative wind sorts precipitation particles falling within the forward flank of a supercell, smaller particles are advected toward the supercell's core because they have lesser terminal fall velocities. As a result, an arc-shaped region of enhanced Z_{DR} encompassing larger, more oblate drops forms at the reflectivity gradient along the southern edge of a supercell's forward flank (Fig. 1.3; Kumjian and Ryzhkov 2008, Dawson et al. 2014).

Initially, the strength of a Z_{DR} arc was thought to be positively correlated to the degree of low-level, storm-relative helicity (SRH), a measure of the streamwise component of environmental vorticity (Kumjian and Ryzhkov 2007). In turn, a storm that develops a Z_{DR} arc was thought to be experiencing enhanced SRH and could, in turn, undergo increasing low-level rotation and, eventually, tornadogenesis. However, in his study of 109 supercells, Wilson (2019) found that instability and moisture control the

[2] As defined by Doviak and Zrnic (2014), the scattering cross-section of an object is "an apparent area that intercepts a power…which, if radiated isotropically, produces at the receiver a power density…equal to that scattered by the actual hydrometeor."

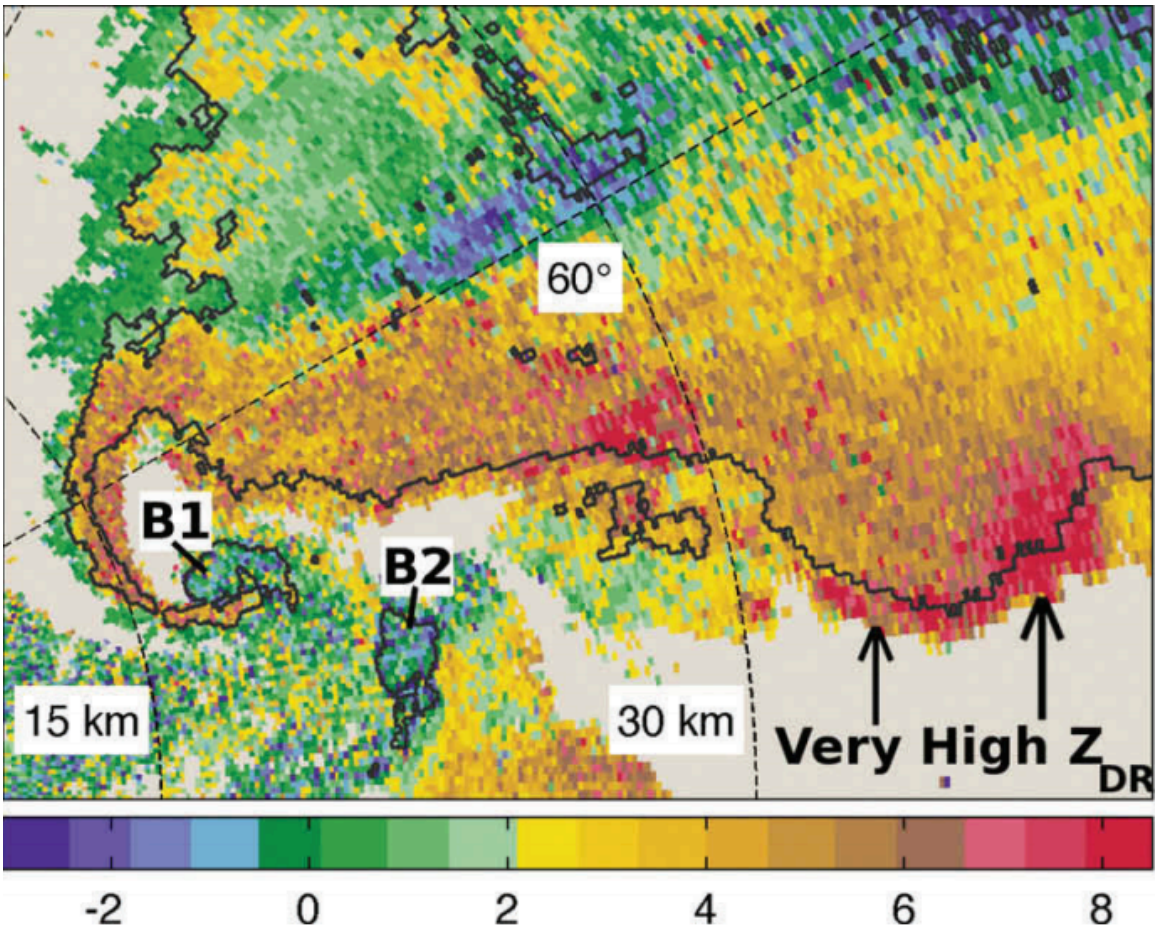

Figure 1.3: Z_{DR} imagery at 1° in elevation at 2245 UTC 10 May 2010 of a tornado-producing supercell near Norman, OK, from the OU Polarimetric Radar for Innovations in Meteorology and Engineering (OU-PRIME). B1 and B2 denote the location of simultaneous tornadoes ongoing at the time of data collection, and the Z_{DR} arc is denoted by the black arrows. Adapted from Palmer et al. (2011).

characteristics of Z_{DR} arcs more strongly than low-level shear and SRH. In fact, a slight negative correlation between Z_{DR} arc size and low-level shear was discovered. In addition, increases in Z_{DR} arc size and intensity were not found to be reliable precursors for increasing low-level rotation and tornadogenesis.

1.1.2.2 Weak-echo Hole

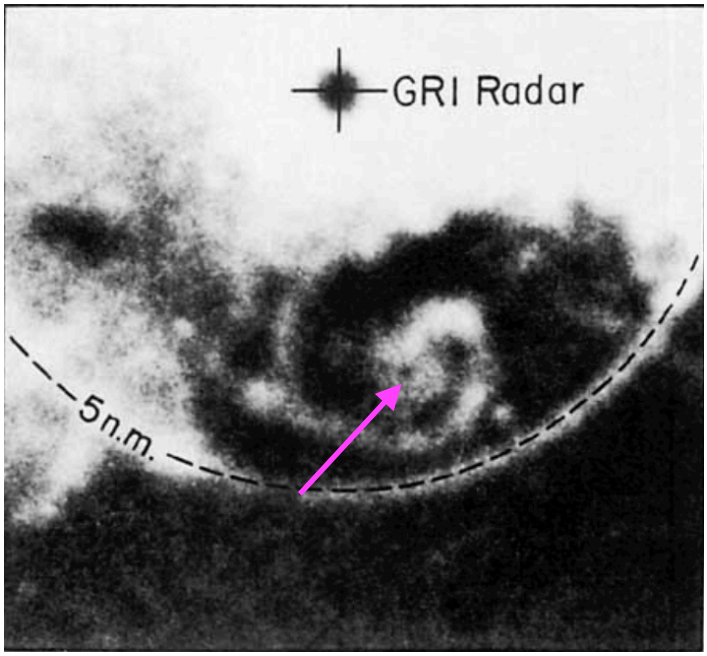

Figure 1.4: WSR-57 radar image of the hook echo of a tornadic supercell near Grand Island, NE, on 3 June 1980. The pink arrow denotes the WEH, which was associated with a tornado. Adapted from Fujita (1981).

A common radar signature that accompanies tornadic vortices is the weak-echo hole (WEH), a region of low reflectivity within the hook echo of a supercell that is, essentially, a small-scale version of a hurricane eye (Fig. 1.4; Wakimoto and Martner 1992, Bluestein et al. 2004). WEHs can form from the centrifuging of debris and hydrometeors away from a tornado's center (Dowell et al. 2005) or as a result of axial downdrafts within the tornado core (Wurman et al. 1996). Fujita (1958) authored the first description of a WEH in literature in his study of a tornado near Champaign, IL, on 9 April 1953. High-resolution, mobile radar data have shown that the center of a tornado is almost always coincident with a WEH (e.g. Wurman et al. 1996; Wurman and Gill 2000); however, the WEH often closes near the surface, owing to the overwhelming effects of frictional convergence (Bluestein et al. 2002, 2007; Houser et al. 2016). In addition, a

WEH does not guarantee the presence of a tornado. A WEH that extends through a vertical depth within a supercell is deemed to be a weak-echo column (WEC; Tanamachi et al. 2012). The bottom portion of a WEC may be caused by centrifuging, while the upper portion may be the result of a narrow-but-intense updraft at the center of the vortex. Using data from the ELDORA airborne radar taken during the VORTEX project, Wakimoto et al. (1996) found evidence of WEHs that extended to near the top of supercells, thus satisfying the definition of a WEC, in the Texas Panhandle in June 1995.

1.1.2.3 Tornado Debris Signature

Perhaps the most reliable radar-based indication of an ongoing tornado is the tornado debris signature (TDS), a distinct lowering in copolar cross-correlation coefficient (ρ_{HV})—a measure of the homogeneity of the shapes, sizes, and orientations of targets within the radar beam—and/or lowered Z_{DR} (to near zero) coincident with a TVS (Kumjian and Ryzhkov 2008), as shown in Fig. 1.5[3]. TDSs occur due to the random and irregular size, shape, and orientation of non-meteorological scatterers (i.e. debris) within a tornado. Tornadoes over open fields or those that are farther away from the radar may not display a TDS due to the lack of lofted debris and beam broadening, respectively. In the case of a rain-wrapped tornado, raindrops may mix with lofted debris, increasing Z_{DR} and, perhaps, negating a clear TDS in the Z_{DR} field (Bluestein et al. 2007); however, ρ_{HV} will still remain low given the heterogeneity of scatterers within the vortex.

[3] This figure was created by the author, although similar figures exist in Wienhoff et al. (2020).

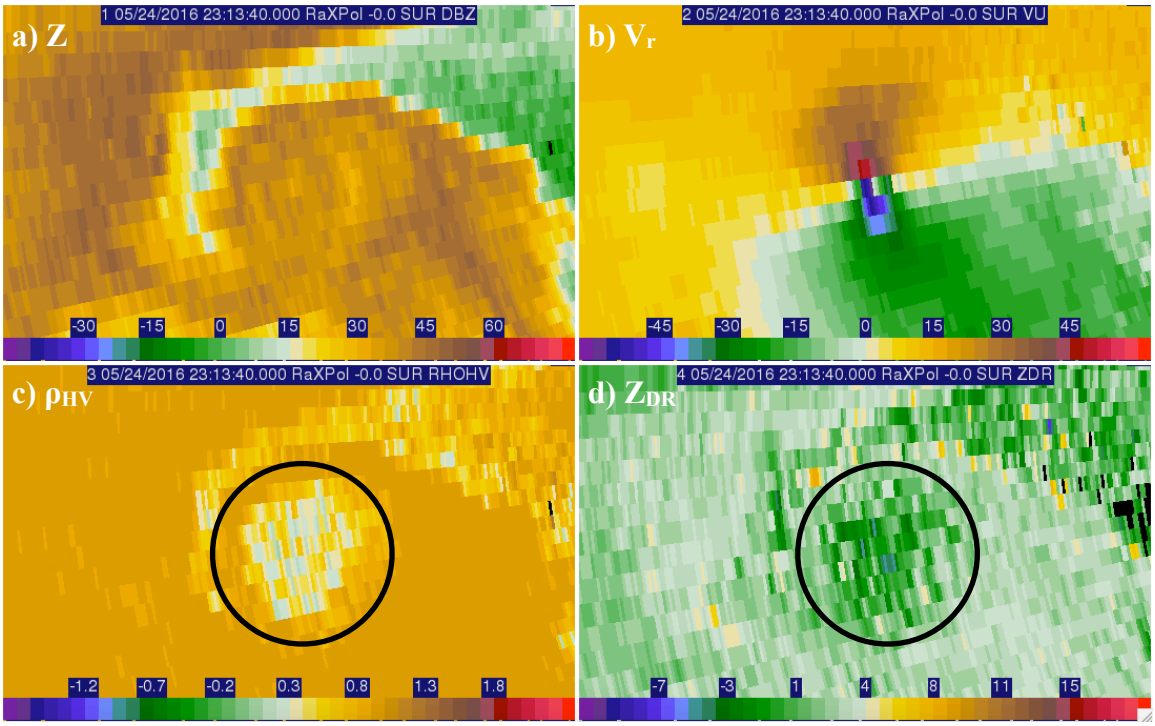

Figure 1.5: RaXPol imagery at 0° in elevation at 2313:40 UTC 24 May 2016 of a) reflectivity (dBZ), b) velocity (m s^{-1}), c) correlation coefficient (dimensionless), and d) differential reflectivity (dB) showing the TVS and TDS associated with a strong tornado near Dodge City, KS. The black circles in (c) and (d) are used to help denote the lowering in ρ_{HV} and Z_{DR} associated with the TDS.

In their study of dual-polarization radar data of a strong tornado in Oklahoma, Ryzhkov et al. (2002) were the first to associate a lowering in ρ_{HV} and Z_{DR} with tornado-lofted debris. Ryzhkov et al. (2005) found these signatures to be repeatable and reliable indicators of strong-to-violent (rated as a 3 or greater on the enhanced Fujita scale (EF3+)) tornadoes; however, Kumjian and Ryzhkov (2008) note several examples of weaker tornadoes producing TDSs. In any case, TDSs tend to correlate well with the degree of real-time tornado damage; Ryzhkov et al. (2005) found that, for three EF3+ tornadoes, as TDS size was maximized and ρ_{HV} and Z_{DR} were minimized, peak tornado

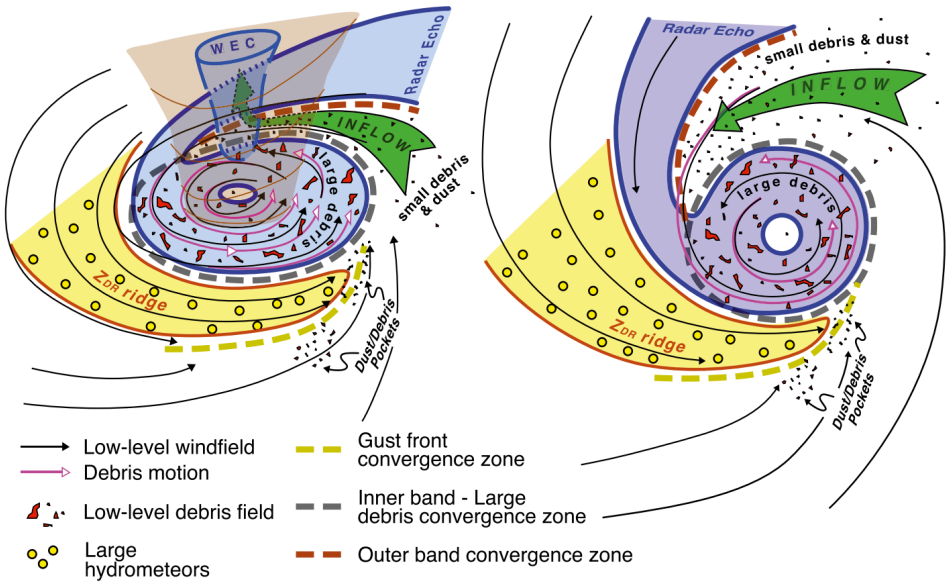

Figure 1.6: Schematic diagram of the low-level wind field and its relation to debris motion within a tornado near El Reno, OK, on 31 May 2013. Adapted from Wakimoto et al. (2016).

damage severity occurred. Schultz et al. (2012) and Bodine et al. (2013) also found a generally positive correlation between TDS diameter and height versus EF rating.

Fig. 1.6, adapted from Wakimoto et al. (2016), is a schematic diagram of the low-level wind field and its relation to debris motion within the aforementioned 2013 El Reno, OK, tornado. Wakimoto et al. (2016) found numerous convergence bands in the vicinity of the TVS, including an inner convergence band that likely was the result of positive bias in radial velocity due to the centrifuging of large debris rotating about the vortex. This debris-induced positive bias was also found in a tornado near Shawnee, OK, on 19 May 2013 (Wakimoto et al. 2020). In addition, as debris was lofted by the Shawnee tornado, reflectivity increased while ρ_{HV} and Z_{DR} both decreased, consistent with the findings of Kumjian and Ryzhkov (2008), and the areal extent of the TDS increased.

1.1.3 Tornado Decay

According to Dowell and Bluestein (2002), "tornado maintenance requires the continued collocation of vertical vorticity and horizontal convergence." If a disruption in either of these variables occurs, particularly if the low-level circulation or convergence near the updraft base decreases, the tornado may dissipate. More often, low-level convergence decreases when cold outflow from the supercell's downdraft wraps around the vortex and cuts off the supply of warm, moist air to the updraft (Lemon and Doswell 1979, Klemp 1987, Wicker and Wilhelmson 1995). In addition, if a tornadic vortex advects away from areas of vertical vorticity production, tornado maintenance ceases, especially in cases of cyclic tornadogenesis (Dowell and Bluestein 2002).

While numerous high-resolution, mobile radar studies have focused on tornadogenesis and evolution, fewer have discussed the tornado decay process. Marquis et al. (2012) employed numerical techniques on DOW data from four different tornadoes to determine additional factors that modulate tornado maintenance. They determined several agencies that promote tornado dissipation, including changes in RFD magnitude, occlusion via secondary RFD surges, and misalignment between the vortex and midlevel updraft. The aforementioned Goshen County, WY, tornado on 5 June 2009 exhibited the latter, partly caused by a decrease in buoyancy in air parcels within the low-level mesocyclone (Marquis et al. 2016). A conceptual model of tornado decay in supercells without secondary RFD gust fronts is given in Fig. 1.7. French et al. (2014) found that, in two of three tornadoes studied, the dissipation of the vortex began at 1.5 km above ground level (AGL) and then at progressively higher levels; TVS dissipation occurred

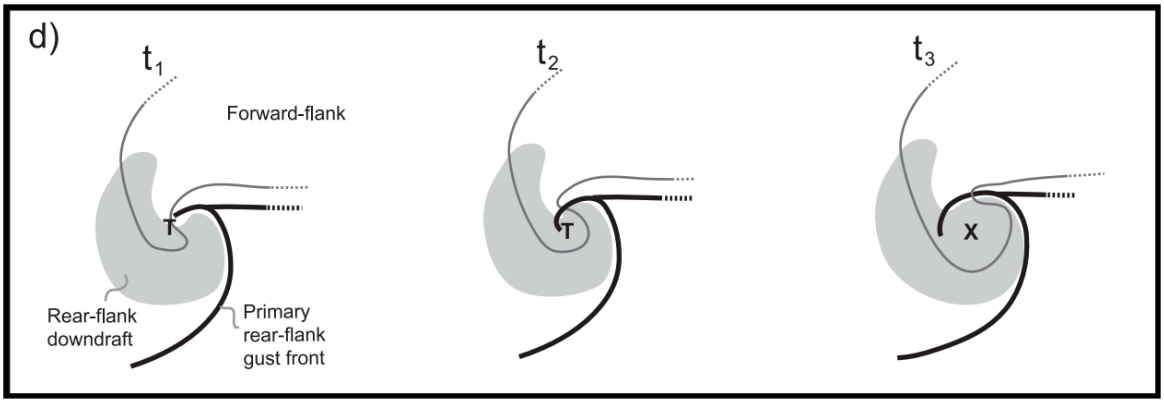

Figure 1.7: A schematic illustration from Marquis et al. (2012) of their conceptual model of the evolution of storm-scale features on the rear flank of a supercell with a single RFD gust front during tornado maturity (t_1-t_2) and dissipation (t_3). For t_1 and t_2, a "T" marks the tornado location, and an "X" marks the location of vortex dissipation at t_3. Solid black lines demarcate gust front boundaries, gray contours denote radar reflectivity, and gray shading denotes low-level divergence associated with the RFD. Fine dashed lines indicate that the feature continues beyond the area illustrated, and long dashed lines represent uncertainty in the location of the feature.

last in the lowest 1 km AGL in all three cases. In two of the cases, the TVS moved to the right of the storm motion vector below 1.5 km AGL and to the left above this level during dissipation. RFD gust front surges occurred around the time of dissipation in these cases, as well. Houser et al. (2015) and Griffin et al. (2019) also found that, in separate cases, dissipation ensued in a similar "inside-out" manner to the cases in French et al. (2014), even though dissipation characteristics are dependent on the Δv_{max} threshold one uses to define a TVS.

More recently, McKeown et al. (2020) authored an in-depth study of the dissipation of an EF3 tornado near Sulphur, OK, from 9 May 2016. They found that the tornado dissipated in two distinct phases, the first of which featured a rapid decline in low-level vortex intensity over a five-minute period followed by a more gradual decrease over a twelve-minute stretch. During decay, the vortex moved more toward the rear of the

parent supercell, and the tornado became increasingly displaced from the main updraft, as described in Dowell and Bluestein (2002) and Marquis et al. (2012). In addition, the tornado dissipated during a significant increase in overall drop size and, in turn, Z_{DR} within the hook echo of the supercell.

1.2 Study Overview

During the springs of 2015 and 2019, four tornadic supercells in Oklahoma were documented by the MWR-05XP and/or RaXPol radars. On 6 May and 16 May 2015, supercells produced strong, long-track tornadoes from Amber to Bridge Creek and from near Elmer to Tipton, OK, respectively. The MWR-05XP collected data from both of these storms, and the 16 May storm was probed by RaXPol, as well. On 1 May and 15 June 2019, RaXPol collected data on two supercells that produced multiple weak tornadoes near Marietta and Putnam, OK, respectively. The main purpose of this thesis is to analyze these storms to compare them with previous cases that were documented by high-resolution, mobile radar and to identify any new features or behaviors that have yet to be documented. Analysis of each case focuses on the following points: 1) the behavior of the TVS during tornadogenesis and decay to determine whether or not the TVS builds upward or downward with time, 2) how the TVS as a function of height evolves over time in terms of intensity and size, 3) the tilt of the TVS as a function of height and how it evolves over time, and 4) any other features, particularly those that have rarely been previously documented or that yielded changes to the behavior of the vortex in a certain case, such as RFD surges and secondary vortices. In addition, this study aims to identify

features and behaviors that have been documented in the past to lend more credence to their roles in the supercell and tornado life cycles. Chapter 2 will describe the instrumentation used in this study, as well as the methods behind how the data was collected, processed, and analyzed. Chapters 3-6 will discuss the results of the analyses for the Amber-Bridge Creek, Putnam, Elmer-Tipton, and Marietta tornadoes, respectively, and Chapter 7 will provide a discussion on the main takeaways from each case and how this work can be continued for future cases.

Chapter 2

Methodology

2.1 Overview of Instrumentation

2.1.1 A Mobile, Rapid-Scan, X-band, Polarimetric, Doppler Radar (RaXPol)

Maintained by the Advanced Radar Research Center at the University of Oklahoma, the Rapid X-band Polarimetric (RaXPol) mobile Doppler radar features a mechanically rotating, 2.4-m parabolic dish mounted on the modified bed of a Chevrolet C-5500 truck (Fig. 2.1; Pazmany et al. 2013). RaXPol was made operational in 2011 and quickly became a coveted tool for collecting data on tornadic supercells thanks to its rapid scanning rate and dual-polarization capability. Selected specifications for RaXPol are displayed in Table 2.1.

In rapid-scan mode, RaXPol employs its maximum azimuthal scanning rate of 180° s^{-1}. At this rate, the antenna moves one beamwidth in 5.6 ms and typically averages data from 12 transmitted pulse pairs in 4.8 ms. These pulse pairs undergo frequency hopping, in which each pair's frequency is shifted by at least the pulse bandwidth so that the backscattered signals may be treated as independent samples, allowing each radar

Figure 2.1: RaXPol photographed by the author near Tuttle, OK, on 12 May 2021.

parameter to converge upon its mean more quickly within the 4.8-ms averaging interval. This allows the radar to collect greater numbers of samples more quickly than it would be able to without frequency hopping (Wienhoff 2016). In addition, frequency hopping inhibits second-trip echoes from contaminating the first sample in each pair, from which correlation coefficient (ρ_{HV}) and power detected from the radar's horizontally and vertically polarized channels (P_H and P_V, respectively) are determined (Pazmany et al. 2013).

RaXPol can also be operated in "strobe" mode, which decreases the effects of beam smearing, a result of temporal averaging. The strobe technique reduces the averaging interval to the time required to transmit a single pulse pair, such that all the pulse pairs of the standard averaging interval (described above) are combined into a single, strobed pulse pair. The first strobe pulse consists of all the first pulses of the original pulse pairs, and the second strobe pulse contains all the second pulses (Pazmany

Table 2.1: Selected RaXPol specifications.

Center frequency	9.73 GHz ± 20 MHz
Maximum transmit power	20 kW
Half-power (3 dB) beamwidth	1.0°
Pulse repetition time	Uniform or staggered
Pulsewidth	0.1-40 μs
Range resolution	7.5-75 m
Maximum antenna rotation rate	180° s^{-1} (azimuth) 36° s^{-1} (elevation)
Antenna diameter	2.4 m

et al. 2013). As a result, independent samples can be collected at one time, thus preserving the angular resolution, which slightly degrades due to beam smearing in rapid-scan mode (Wienhoff 2016).

Given its 180° s^{-1} azimuthal scanning rate, RaXPol can perform a volume scan comprised of ten elevation angles (e.g., a volume scan of 10° in depth if elevation angle is incremented by 1°) in approximately 20-22 seconds. This makes RaXPol an extremely effective tool for probing tornadic supercells, vortices, and other sub-storm-scale phenomena, which evolve on the order of seconds. In addition, RaXPol's dual polarization capability yields numerous additional variables to consider, including correlation coefficient, which aids in tornado debris studies; spectrum width, which can

help identify tornadic and non-tornadic vortices; and differential reflectivity, which can be used to study supercell intensity (Ryzhkov et al. 2005, Yu et al. 2007, Dawson et al. 2014). However, RaXPol does have a few drawbacks. First, as with most X-band radars, data are significantly attenuated when the radar is operated in precipitation or when the radar beam travels through ample precipitation. To combat this, the attenuation correction techniques outlined in Snyder et al. (2010), which detect and correct for attenuation using dual polarization, must be applied to RaXPol data; however, attenuation remains an issue in heavy rain and hail, and if the signal is attenuated to extinction, it cannot be salvaged. Also, when RaXPol is operated in strobe mode, the blind range, which is the minimum distance a specific target must be from the radar to be detected, increases due to the lengthier transmission period before the radar switches to receive (Wienhoff 2016). Given RaXPol's close proximity to tornadic phenomena when collecting data, this can be problematic.

2.1.2 The Meteorological Weather Radar 2005 X-band Phased Array (MWR-05XP)

The Meteorological Weather Radar 2005 X-band Phased Array (MWR-05XP) consists of a modified Army tactical radar mounted on the bed of a heavy-duty truck (Fig. 2.2; Sandifer 2005). The radar can be deployed in approximately 5 minutes; this, combined with its phased array design, makes MWR-05XP a viable option for collecting rapid-scan data in the vicinity of tornadoes and supercells (Bluestein et al. 2010). Selected specifications for the MWR-05XP are displayed in Table 2.2.

Figure 2.2: The MWR-05XP. Photograph by H. Bluestein, adapted from Bluestein et al. (2010).

The MWR-05XP is a phased array radar that employs an array of antennae that can scan azimuthally and in elevation without mechanically rotating. Electronic scanning in azimuth is minimal and only used to minimize beam smearing by effectively keeping the beam in nearly the same location; actual azimuthal scanning is done mechanically. To scan vertically, the radar uses phase shifters to change the phase delay between the antenna elements, and when scanning azimuthally, the radar utilizes frequency hopping (discussed in section 2.1.1) with every other pulse so that the beams' phases change as their frequencies change (Bluestein et al. 2010). As with RaXPol, frequency hopping

Table 2.2: Selected MWR-05XP specifications.

Transmitted frequency	9.3-10 GHz
Maximum transmit power	≥ 15 kW
Half-power (3 dB) beamwidth	1.8°
Maximum pulse repetition frequency	10 kHz
Pulsewidth	1 μs
Range resolution	150 m[1]
Maximum azimuthal scanning rate	180° s^{-1}

decreases beam smearing and allows the MWR-05XP to collect a greater number of independent samples despite its rapid maximum azimuthal scanning rate of 180° s^{-1}.

As discussed in Bluestein et al. (2010), the MWR-05XP features two different scanning modes: stepped frequency spiral (STF-SP) and stepped frequency elevation (STF-E). In STF-SP mode, the radar collects data over 360° in azimuth with overlapping elevation angles whose increment is an angle less than the elevation beamwidth of the antenna. This is similar to how WSR-88D radars operate, only ten times faster; in this mode, the MWR-05XP can complete a volume scan up to 20° in elevation in approximately 25 seconds. STF-SP mode is most suited for situations in which the radar must scan multiple storms simultaneously or a large area of precipitation. In contrast, in

[1] The range resolution of the MWR-05XP data in this study appears to be 75 m; therefore, the data are oversampled.

STF-E mode, the radar scans electronically in elevation as it slowly rotates mechanically in azimuth (with some frequency hopping to enable backscanning to keep the beam "pointed" at the same azimuth as the antenna mechanically rotates). Specifically, the radar transmits a pulse pair at the lowest elevation angle and then at increasingly high elevation angles before reaching the desired maximum elevation angle. This process repeats such that each elevation angle is scanned using ten pulse pairs at each targeted azimuth angle. The ten pulse pairs are then averaged at each elevation angle to compute the radar moments. As this process continues for each subsequent azimuth angle, the antenna continues to slowly rotate in azimuth. In STF-E mode, the radar can complete a 90° sector scan up to 20° in elevation in approximately 13 seconds.

With its high temporal resolution, the MWR-05XP is a useful tool for studying severe convective storms at close range. However, it does have some limitations. First, unlike RaXPol, the MWR-05XP does not have dual polarization capability; therefore, information on the size, shape, orientation, and type of scatterers cannot be determined. In addition, the antenna array has a beamwidth (1.8°) that is nearly twice that of most mobile, X-band, Doppler radars. As a result, Bluestein et al. (2010) caution that the MWR-05XP is most suited for observing storm-scale phenomena rather than sub-storm-scale features, such as tornadoes. Given its azimuthal resolution of approximately 300-600 m at a range of 10-20 km, it can adequately sample mesocyclones greater than 2.5-5 km across but not tornadoes. The MWR-05XP can only begin to resolve airflow within a tornado if it collects data within 5 km of the vortex and if the tornado is approximately 2 km or greater in diameter. Though RaXPol has a narrower beam, it is

often smeared to near the resolution of the MWR-05XP; however, as previously discussed, techniques such as frequency hopping and the utilization of strobe mode can negate the effects of beam smearing.

2.2 Data Quality Control

Radar data quality depends on a number of variables, including the characteristics of the radar and the environment being sampled. To use the rapid-scan capability of both RaXPol and MWR-05XP, one must limit the number of samples that can be collected for a specific volume, and RaXPol's rapid rotation rate likely leads to beam smearing (Bluestein et al. 2010, Pazmany et al. 2013). In addition, turbulent motions and debris centrifuging within tornadic vortices often degrade data quality in these regions. As a result, data from each case were carefully inspected and, if necessary, edited using a stringent quality control process.

Data were manually edited using the National Center for Atmospheric Research's Solo3 software (Oye et al. 1995). Velocities were aliased within tornadic vortices and in regions of strong inflow where wind speeds exceeded the respective radar's Nyquist velocity. In cases using the MWR-05XP, Nyquist velocity was not recorded and, therefore, had to be calculated manually. However, in the Amber-Bridge Creek case, the Nyquist velocity could not be calculated explicitly due to missing wavelength and pulse repetition frequency (PRF) values. In turn, it was estimated to be 40 m s^{-1}, based on the PRF used in previous studies involving the MWR-05XP, such as French et al. (2014). During data collection on the Amber-Bridge Creek tornado, velocities appeared to alias

around a Nyquist velocity of 55.4 m s^{-1}; however, this is much higher than the expected Nyquist velocity of 40 m s^{-1} and produced erroneously large Δv_{max} values. Therefore, Δv_{max} values using dealiased velocities were scaled by a factor of 40/55.4, a technique that produced much more reasonable values that generally agreed with the intensity determined by damage surveys[2]. In previous studies (e.g. Snyder and Bluestein 2014), spectrum width (σ_v) and normalized coherent power (NCP), a signal quality index that is inversely proportional to σ_v, have been used to remove radar data of questionable coherency (low NCP/high σ_v). However, σ_v and NCP fields were either erroneous or unavailable for all cases except the Elmer-Tipton case, for which noise and ground clutter (a wind farm) were removed by both manually (subjectively) deleting non-meteorological pixels and thresholding data on NCP < 0.25 and σ_v > 12.

2.3 Tornado Vortex Signature Criteria

The TVS was first discovered by Burgess et al. (1975), who noted extreme shear between two Doppler radar range gates flanking the location of a tornado near Union City, OK, on 24 May 1973. Strong gate-to-gate (GTG) shear near the center of the parent mesocyclone aloft only often signifies a nascent tornado, while GTG shear near the surface extending aloft, assuming a supportive near-storm environment, may indicate a high probability of a tornado in progress (Brown et al. 1978). Since these initial studies, the definition of a TVS has broadened from strictly GTG shear, though continuity in both height and time remains a critical feature of a TVS. The criteria for defining TVSs varies

[2] These values could not be compared to those determined by other mobile Doppler radars collecting data concurrently, as only the MWR-05XP collected data on the Amber-Bridge Creek tornado.

based on the spatial resolution of the scanning radar. Alexander and Wurman (2008) determined that $\Delta v_{max} \geq 40$ m s^{-1} over a maximum distance of 2 km is, generally, an acceptable threshold for identifying tornadoes from high-resolution mobile Doppler radar datasets. Subsequent studies using DOW and RaXPol data, including those by Kosiba et al. (2013) and Bluestein et al. (2019), have employed this threshold, as well. However, French et al. (2013) defined a TVS as having *gate-to-gate* $\Delta v_{max} \geq 20$ m s^{-1}, suggesting that, for radars with coarser spatial resolution (e.g. the MWR-05XP), a lesser threshold should be considered.

In this study, the TVS criteria adopted in Alexander and Wurman (2008) was used for each of the four cases. For the two cases that employed the MWR-05XP (Amber-Bridge Creek and Elmer-Tipton), Δv_{max} was always well in excess of the 20 m s^{-1} threshold espoused in French et al. (2013), even when a tornado was not in progress; a 40 m s^{-1} Δv_{max} threshold better correlated with the boundary between tornadic and subtornadic vortices. As in Bluestein et al. (2019), Δv_{max} was doubled and then divided by Δr, the distance between the maximum inbound and outbound velocity within the TVS, for each radar image to determine pseudovorticity (ζ_{pseudo}), a proxy for vertical vorticity within the tornado if it were axisymmetric. Using the criteria from Alexander and Wurman (2008), a vortex signature is considered a TVS if it has $\zeta_{pseudo} \geq 0.04$ s^{-1}. ζ_{pseudo} was often a more accurate representation of whether or not a vortex signature was a TVS than Δv_{max} alone since, in many cases (usually in the storm's mid- and upper levels or during the pretornadic phase), Δv_{max} would greatly exceed the 40 m s^{-1} threshold but Δr would be much greater than 2 km.

Chapter 3

The Amber-Bridge Creek, OK, Tornado: 6 May 2015

3.1 Synoptic Overview

On 6 May 2015, a synoptic-scale, longwave trough was centered over the Pacific Northwest with multiple shortwaves rotating around its base (Fig. 3.1a). The most prominent of these was located from western Kansas to central Oklahoma at 1200 UTC (Fig. 3.1a) and ejected north-northeastward throughout the day, which promoted subsidence and weak height rises in its wake. Convection on the leading edge of this shortwave trough overturned the atmosphere across central Oklahoma during the morning, leaving only a weak capping inversion in place. Westerly flow associated with the large-scale trough had already promoted lee cyclogenesis, yielding broad cyclonic flow at 850 mb centered over eastern Colorado (Fig. 3.1b) that would be maintained throughout the day. This cyclogenesis induced strong, moist, southerly low-level flow across much of the central and southern Great Plains to the east of a dryline draped from western Kansas southward into the Texas Panhandle. Combined with daytime heating, the moist low levels yielded mixed-layer convective available potential energy (MLCAPE) of 1000-1500 J kg^{-1} in northern Kansas, increasing to 2000-2500 J kg^{-1} in central and

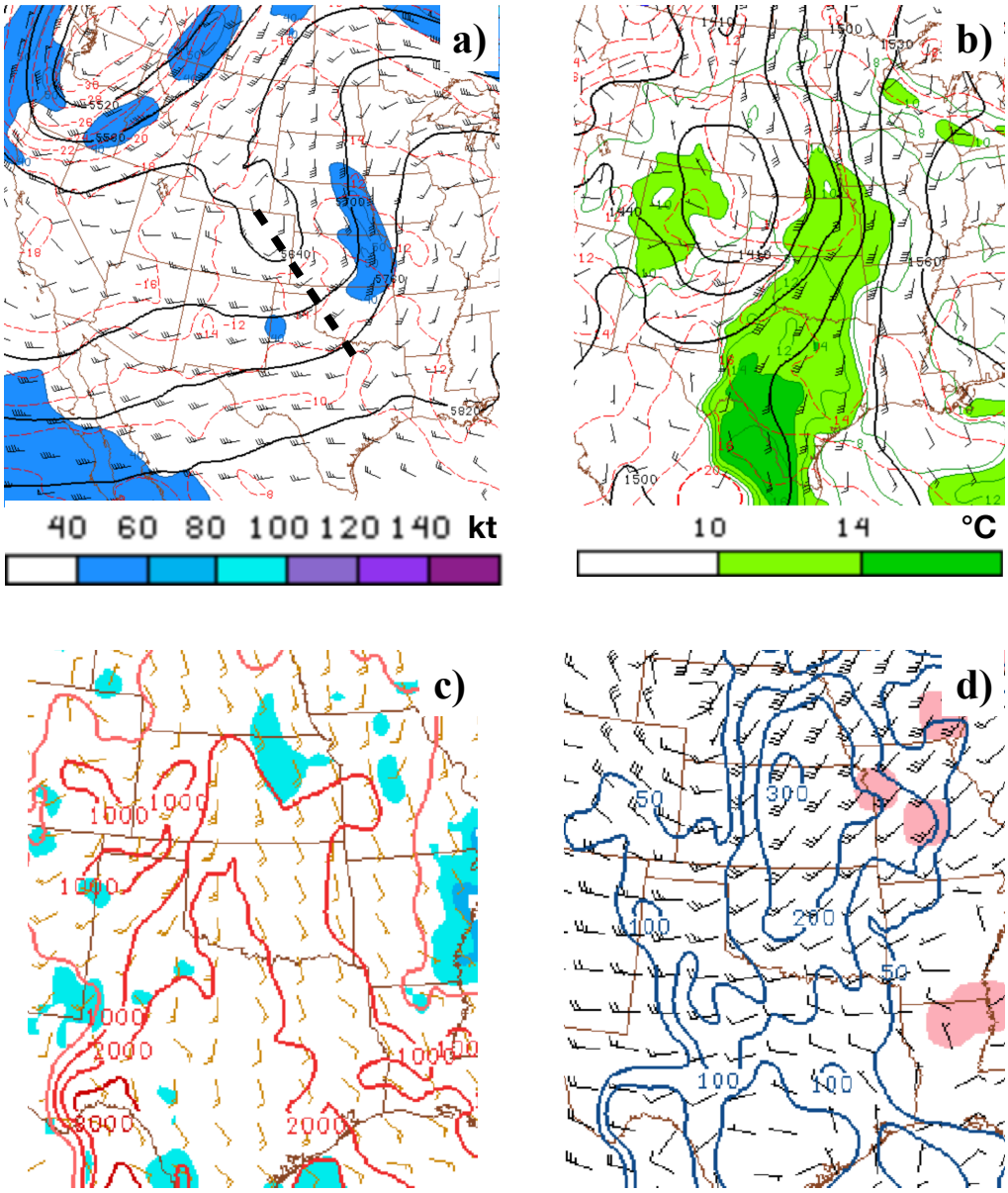

Figure 3.1: Overview of the synoptic environment on 6 May 2015. Pictured above are a) 500 mb winds (kt) valid at 1200 UTC, b) 850 mb winds (kt) and moisture (°C) valid at 1200 UTC, c) MLCAPE and MLCIN (J kg^{-1}) valid at 2100 UTC, and d) ESRH (m^2 s^{-2}) valid at 2100 UTC. The dashed black line in (a) shows the approximate location of the axis of the most prominent shortwave trough. Adapted from the Storm Prediction Center Mesoanalysis Archive.

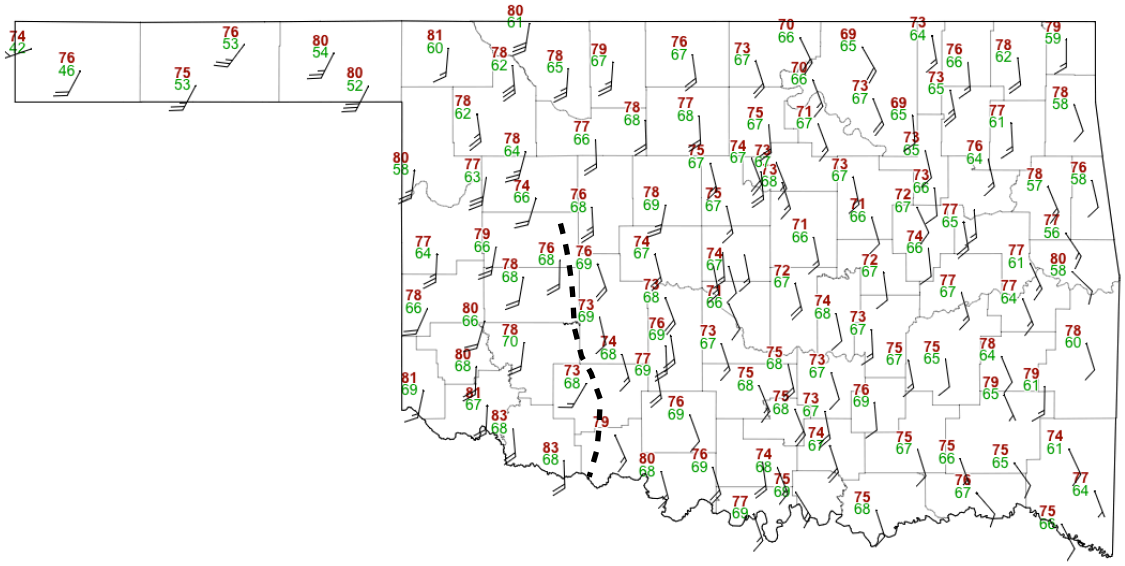

Figure 3.2: Map of surface temperature (°F, red values), dewpoint (°F, green values), and wind speed and direction from the Oklahoma Mesonet valid at 1900 UTC 6 May 2015. The dashed black line represents the approximate location of a surface convergence zone.

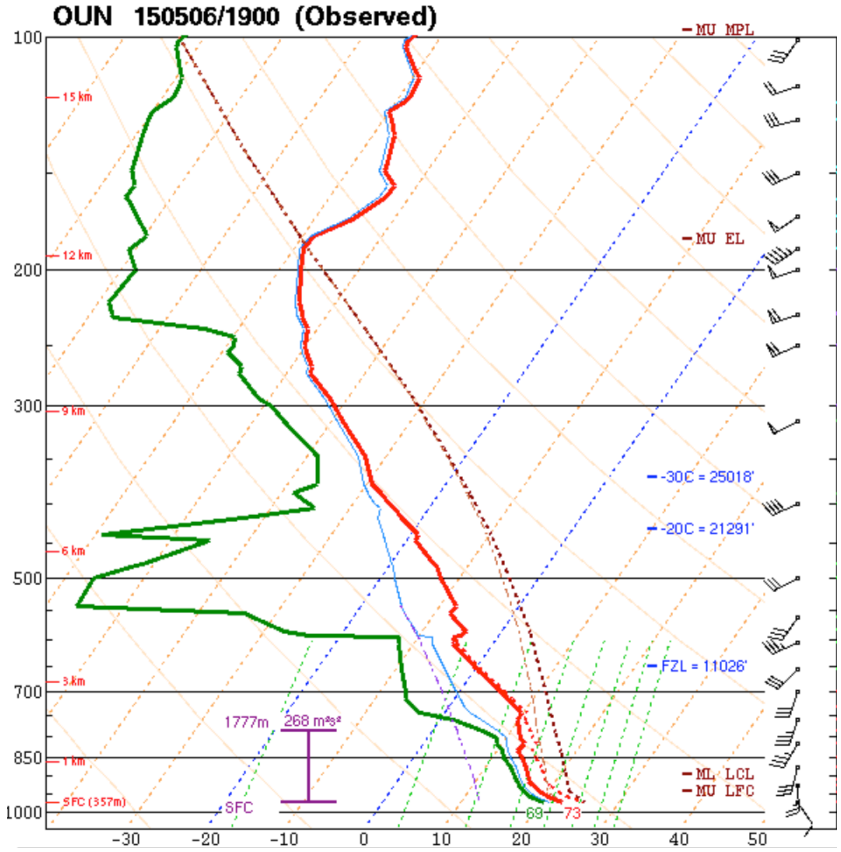

Figure 3.3: KOUN (Norman, OK) sounding taken at 1900 UTC 6 May 2015. Taken from the Storm Prediction Center Severe Weather Events Archive.

southwestern Oklahoma by 2100 UTC (Fig. 3.1c).

The 1900 UTC sounding from Norman, OK (Fig. 3.3), sampled a moist and unstable environment, with a deep moist layer extending from the surface to approximately 800 mb, a surface dewpoint of 69°F (21°C), and low- and midlevel lapse rates exceeding 6.5°C/km. Southeasterly surface winds veering to west-southwesterly at 500 mb promoted 0-6 km AGL wind shear values in excess of 20 m s^{-1}, adequate for supercells, and 850 mb winds in excess of 15 m s^{-1} yielded low-level shear supportive of tornadoes (Fig. 3.1d; effective storm-relative helicity (ESRH) values in excess of 200 m^2 s^{-2}). In addition, a generally north-to-south-oriented surface confluence zone was evident across southwestern Oklahoma, well ahead of the dryline, with warming into the low 80s °F to its west and southwest (Fig. 3.2). This confluence zone may have been caused by a number of phenomena. Perhaps most likely is that there was a strong inversion to the east and a much deeper mixed layer to the west. In turn, more southwesterly momentum may have been transported downward from aloft. Also, the strong upper-level trough may have yielded an increase in cyclonic vorticity with height, in turn increasing surface convergence, manifest by the surface wind shift. These hypotheses, though plausible, are unsubstantiated due to a lack of supporting data. Low-level winds would increase in magnitude throughout the afternoon, further enhancing low-level shear. By 1900 UTC, the remainder of the capping inversion had eroded almost completely (mixed-layer convective inhibition (MLCIN) of -9 J kg^{-1} exhibited in the 1900 UTC Norman sounding (Fig. 3.3)), and convective initiation was well underway along the dryline in southwest Oklahoma.

3.2 Supercell Formation and Evolution

The supercell that produced the Amber-Bridge Creek tornado initiated within a broken line of showers and thunderstorms that developed in the vicinity of Lawton, OK, around 1800 UTC. As it moved northeast, a storm near the southern end of the line began to strengthen while the other storms dissipated. Between 1928-1955 UTC, this storm appeared to merge with a shower approaching from the south, after which the shower's updraft intensified and the original storm's updraft weakened. This is similar to the findings of Hastings and Richardson (2016), who simulated numerous mergers between a mature supercell and a nascent storm, including a configuration similar to this case in which the updraft maxima of the nascent storm and the supercell were in close proximity. After the merger occurred, the shower quickly evolved into a supercell, developing strong low-level rotation and a well-defined hook echo by 2011 UTC. The supercell produced its first tornado approximately 4 km east of Apache, OK, at 2042 UTC, followed by a brief tornado 6.5 km northwest of Cyril, OK, at 2053 UTC (NWS Norman 2015). Fig. 3.4 documents the evolution of the Amber-Bridge Creek supercell using reflectivity imagery from the WSR-88D radar at Oklahoma City, OK (KTLX).

3.3 The Amber-Bridge Creek Tornado

The MWR-05XP was deployed just north of Blanchard, OK, and collected data from 2213:21-2216:19 UTC and again from 2216:56-2240:44 UTC. Between these two intervals, the scanning strategy was changed so that the MWR-05XP scanned higher in elevation (from 20° in the first interval to 30° in the second). For simplicity, each

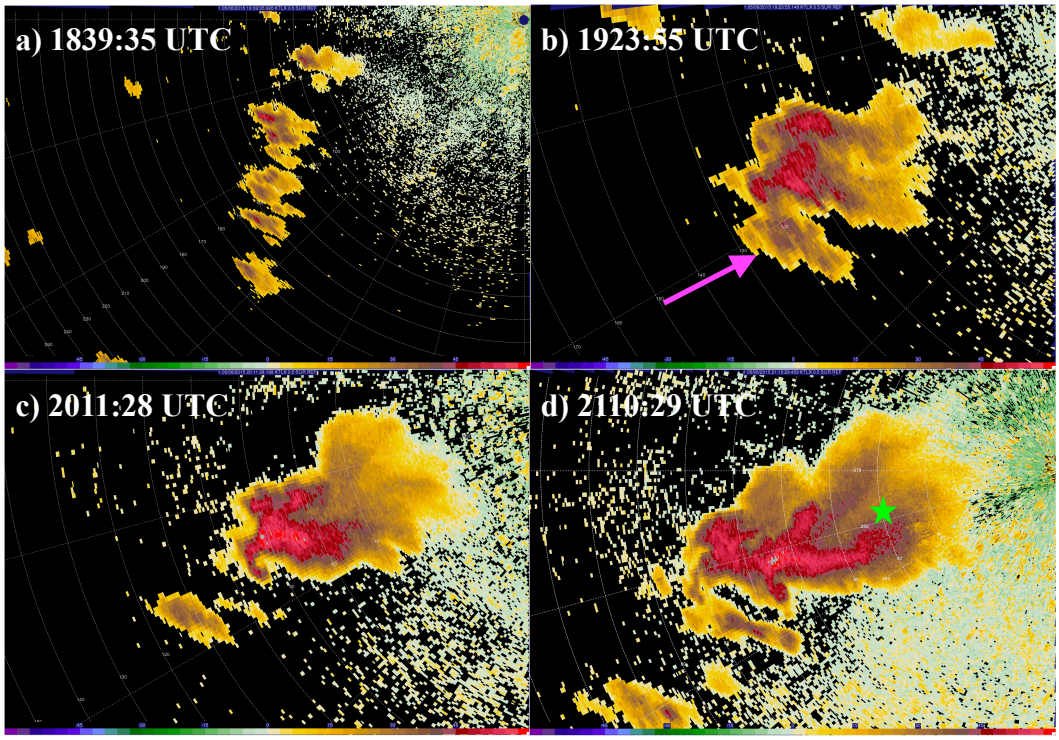

Figure 3.4: Evolution of the supercell that produced the Amber-Bridge Creek tornado using 0.5° reflectivity (dBZ) data from the KTLX radar. Included are a) the initial broken line of showers and storms at 1839:35 UTC, b) the beginning of the storm merger between the mature storm and the nascent shower (denoted by the pink arrow) at 1923:55 UTC, c) the newly formed, post-merger supercell with well-defined hook echo at 2011:28 UTC, and d) the supercell at 2110:29 UTC, several minutes before it produced the Amber-Bridge Creek tornado. The green star in (d) denotes the location of the town of Bridge Creek. Each panel follows the storm as it moves; therefore, the area displayed in each panel is different.

deployment interval will be referred to as Deployment 1 (D1) and Deployment 2 (D2), respectively. Due to a malfunctioning global positioning system (GPS) unit, the exact location and altitude of the MWR-05XP are unknown; therefore, height and distance measurements reported in the upcoming sections are radar-relative.

According to NWS Norman damage surveys (NWS Norman 2015), the Amber-Bridge Creek tornado began approximately 7 km east of Amber at 2133 UTC and dissipated at 2226 UTC approximately 6.5 km north-northeast of Bridge Creek (Fig. 3.5);

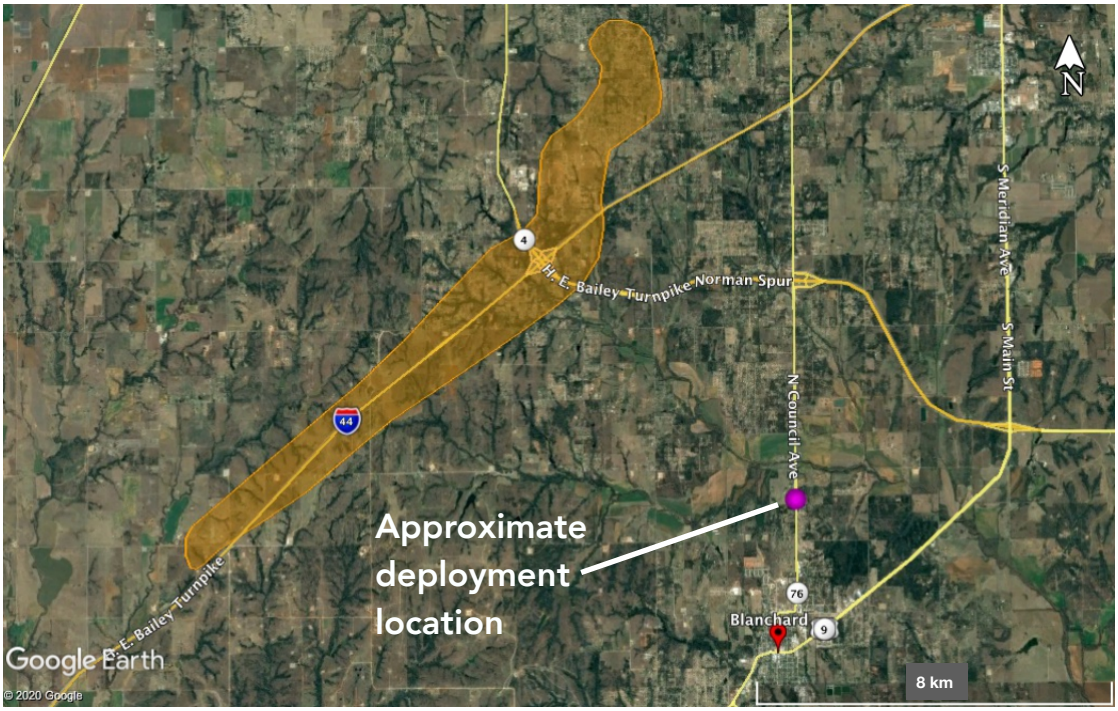

Figure 3.5: Damage path of the Amber-Bridge Creek tornado, denoted by the orange outline, identified from damage surveys. The approximate location of the MWR-05XP during deployment has been labeled. Adapted from NWS Norman (2015).

it produced EF3 damage. MWR-05XP data collection began well into the tornado's life cycle; a vortex signature that exceeded the threshold for tornadic intensity ($\Delta v_{max} \geq 40$ m s^{-1} and $\Delta r \leq 2$ km, based on the criteria given in Alexander 2010), was present at 2.4° in elevation[1] (approximately 0.3 km above radar level (ARL)) for the entirety of D1 and D2 (Fig. 3.6). At this elevation, Δv_{max} weakened, although still maintaining tornadic intensity, from approximately 71 m s^{-1} at 2223:06 UTC to 41 m s^{-1} at 2238:59 UTC. Therefore, it appears that MWR-05XP captured tornado decay; however, the low-level vortex remained at tornado strength well after the dissipation time identified in damage surveys.

[1] Beam blockage prevented accurate analysis of the vortex signature at the lowest elevation angles (0.0°-1.6°) after 2127 UTC; therefore, data from the 2.4° elevation angle were used to identify the TVS.

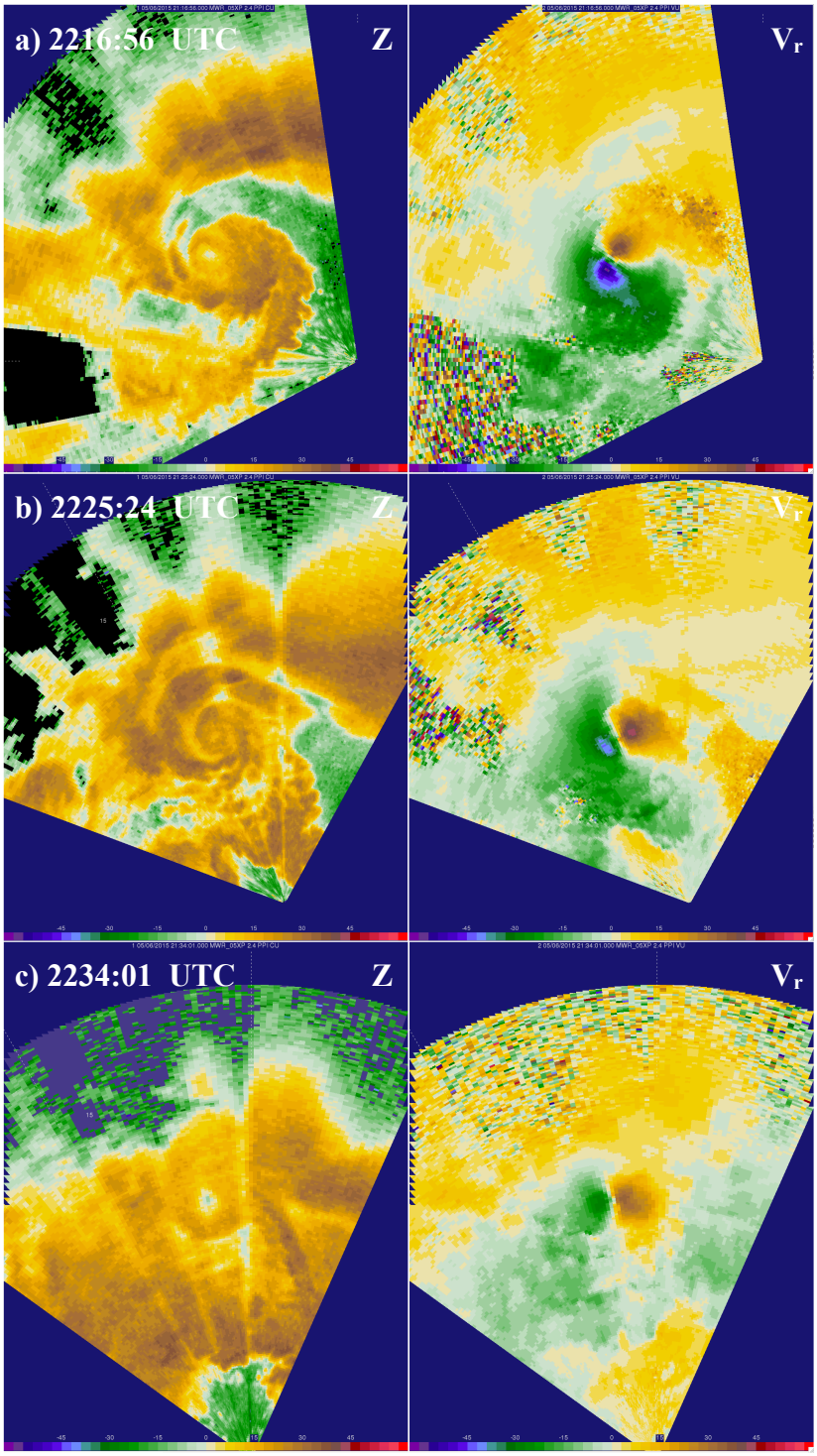

Figure 3.6: From left to right, MWR-05XP reflectivity factor (dBZ, left) and radial velocity (m s^{-1}, right) images of the Amber-Bridge Creek tornado/mesocyclone at 2.4° at a) 2216:56 UTC, b) 2225:24 UTC, and c) 2234:01 UTC.

3.3.1 Evolution of the TVS with Height and Time

Produced to analyze the behavior of the TVS through the observed depth of the supercell over each deployment period, Figs. 3.7 and 3.8 feature plots of Δv_{max} and Δr as a function of height versus time for D1 and D2, respectively. Between 2213:41 and 2214:41 UTC, a decrease followed by an immediate, rapid increase in Δv_{max} to a relative maximum of about 80 m s^{-1} occurs at approximately 2.5 km ARL (Fig. 3.7a). This feature is coincident with the beginning of a period of strengthening of the low-level vortex; however, the increased Δv_{max} neither built upward from the surface nor downward from aloft. This concurrence in low-level and midlevel vortex intensification has previously been identified during tornadogenesis (e.g. Trapp and Davies-Jones 1997); however, in tornadogenesis cases, the vortex builds through a deep layer, as opposed to separately at low- and midlevels. Immediately preceding the period between 2215:41 and 2216:01 UTC in which near-surface Δv_{max} reached its relative maximum (Fig. 3.7a), the near-surface vortex contracted to a relative minimum diameter of less than 0.4 km (Fig. 3.7b). Over this same period, and continuing through the end of D1, the upper-level vortex widened; in fact, the local maximum in upper-level vortex diameter (exceeding 1.6 km) is colocated above the aforementioned local minimum in near-surface vortex diameter between 2215:21 and 2215:41 UTC. Similar widening of the tornadic vortex with height has previously been documented in both numerical vortex models (Lewellen 1993) and high-resolution, mobile radar observations (Burgess et al. 2002).

The first signs of significant decay occur at approximately 2221 UTC (Fig. 3.8a), when Δv_{max} decreases abruptly by about 15 m s^{-1} in the 1-1.5 km ARL layer and,

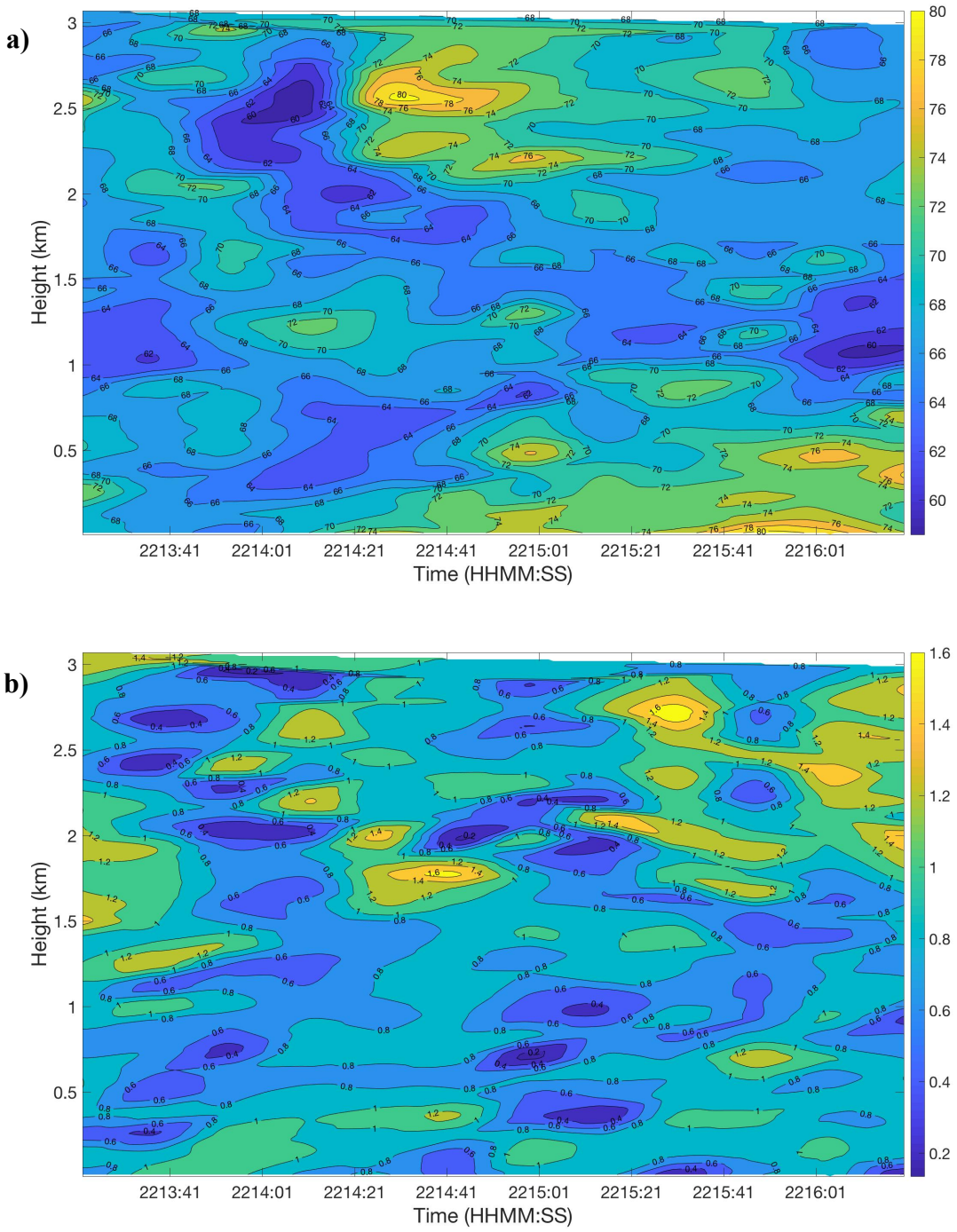

Figure 3.7: Contour plots of a) Δv_{max} (in m s^{-1}) and b) vortex diameter (in km) as a function of time versus height for D1.

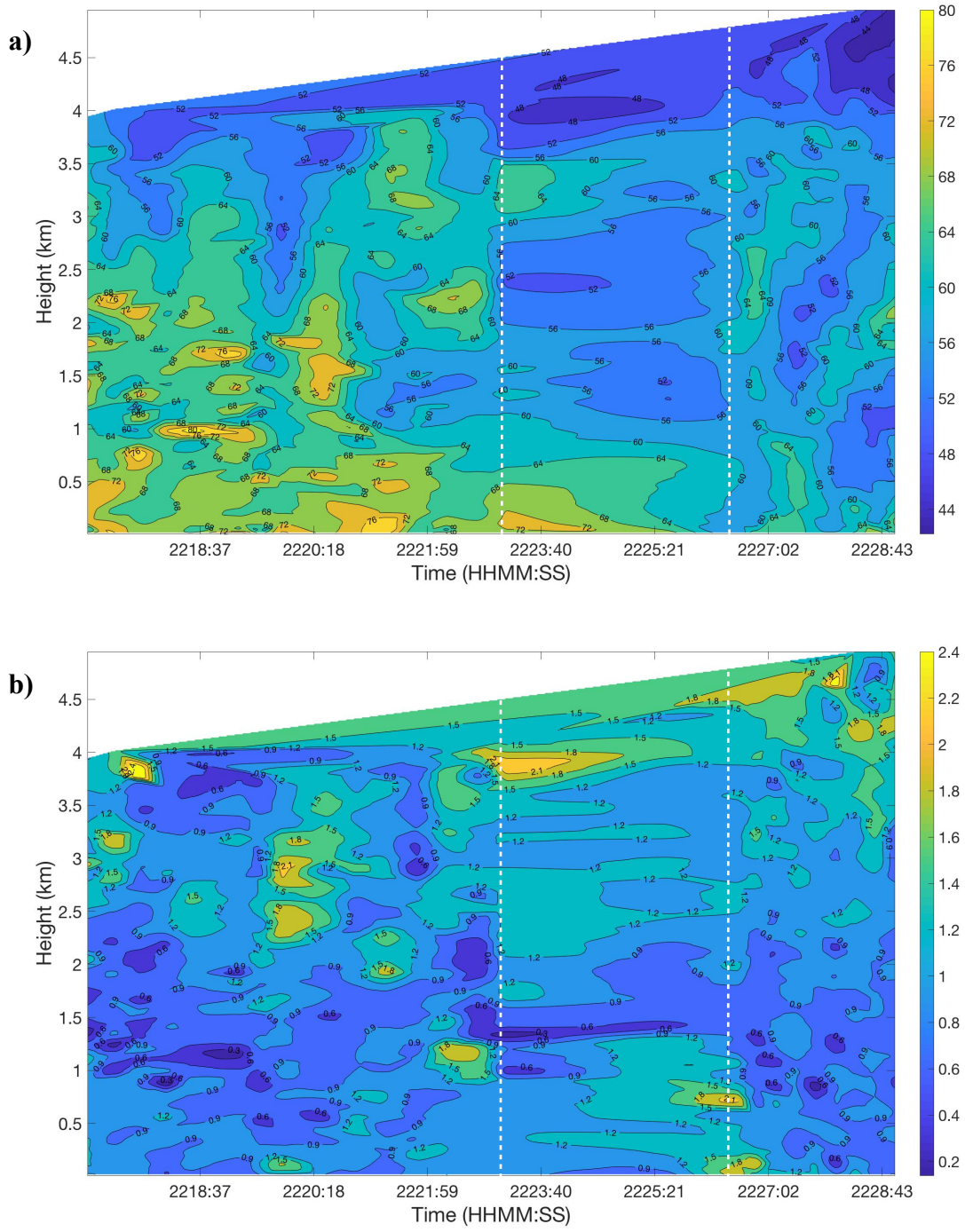

Figure 3.8: As in Figure 3.7, but for D2. The dashed white lines demarcate the beginning (2223:06 UTC) and end (2226:27 UTC) of the period during which the MWR-05XP did not collect any data other than one volume at 2225:24 UTC; the data in between these lines are purely interpolated.

subsequently, in the 2-3 km ARL layer. During this weakening aloft, the low-level vortex remained strong (Δv_{max} generally above 70 m s^{-1}) until 2225:24 UTC. Therefore, it appears that the vortex dissipated in an "inside-out" manner, first in the midlevels, then at slightly higher levels, and finally in the low-levels. This "inside-out" dissipation was also identified by French et al. (2014) in the 5 June 2009 Goshen County, WY, tornado and a tornado near Kingfisher, OK, on 19 May 2010, as well as by Houser et al. (2015) in the 24 May 2011 El Reno, OK, tornado. In addition, as low-level Δv_{max} decayed to less than 60 m s^{-1} by 2226 UTC (Fig. 3.8a), the diameter of the near-surface vortex increased to nearly 2 km (Fig. 3.8b). Broadening of the low-level vortex has previously been determined to be a characteristic of tornado dissipation (Wicker and Wilhemson 1995). The TVS remained at tornado strength for several minutes after the time of decay noted by NWS Norman (2015), which highlights the need for, perhaps, more stringent Δv_{max} and Δr criteria in this case or that the tornado lasted longer than damage surveys indicated.

The author notes one caveat in interpreting the above conclusions associated with vortex decay: for unknown reasons, the MWR-05XP did not collect data from 2223:06-2225:24 UTC and again from 2225:24-2226:27 UTC (one volume was collected at 2225:24 UTC, and normal data collection resumed at 2226:27 UTC). As a result, the data are entirely interpolated during these periods, and the accuracy of the plots in Fig. 3.8 may be slightly compromised. Furthermore, the "inside-out" decay described above may be somewhat of an artifact of the lack of data collected during these periods, although Δv_{max} clearly decreases first in the 1-1.5 km ARL layer. However, the cubic

interpolation scheme used to produce these plots offers numerical stability and greater accuracy than other available types of interpolation methods (Prasad et al. 2018). In addition, French et al. (2014) suggest that the tornado decay process occurs on the order of a few minutes. Thus, while fine-scale fluctuations in the decay process may have been omitted due to the gaps in the data, the author is confident that the decay process was adequately sampled and that the conclusions presented above are accurate.

3.3.2 Vortex Tilt with Height

Throughout the deployment periods, the Amber-Bridge Creek tornado leaned significantly toward the northeast with height, generally above approximately 0.6 km ARL (3.9°; Fig. 3.9). This finding is consistent with the observations and analyses of tornadoes studied by Wakimoto and Martner (1992), Wurman and Gill (2000), Alexander and Wurman (2005), Tanamachi et al. (2012), and French et al. (2014). However, the Amber-Bridge Creek tornado exhibited much greater tilt than that noted in these cases; in general, the vortex was tilted between roughly 50-60° from due north, whereas Alexander and Wurman (2005), for example, analyzed tilt of only about 20° in the 30 May 1998 Spencer, SD, tornado. Along with the 27 May 2015 Canadian, TX, tornado, in which Griffin et al. (2019) identified vortex tilt of up to 55°, as well as the 31 May 2013 El Reno, OK, tornado that tilted up to 45° (Bluestein et al. 2019), this tornado may be one of the most tilted to be analyzed using high-resolution, mobile Doppler radar. The tilt of a tornadic vortex was initially believed to be a product of tornado dissipation (Golden and Purcell 1977, Moller 1978, Wakimoto and Martner 1992); however, as in French et al.

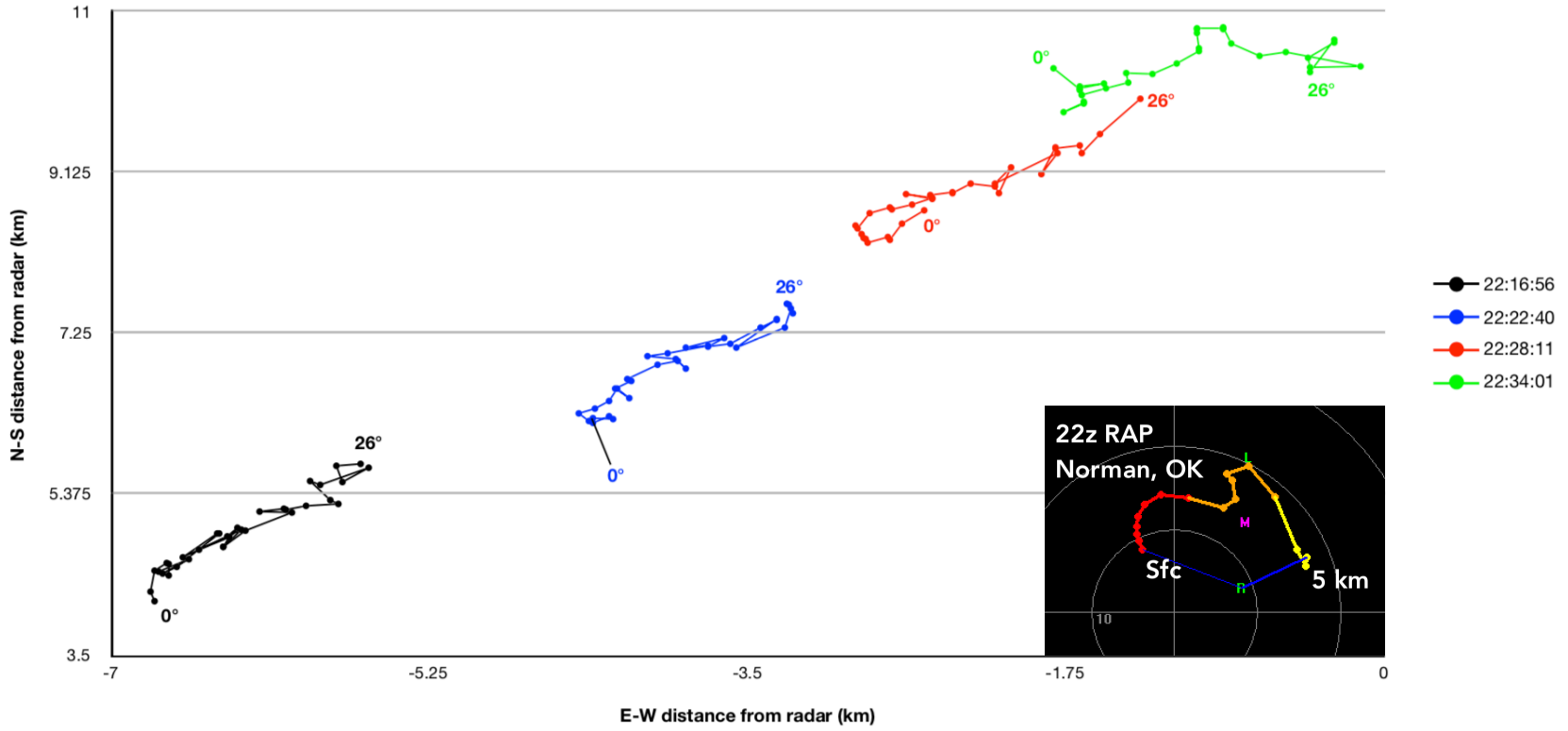

Figure 3.9: Graph of vortex tilt with height for the Amber-Bridge Creek tornado at four different times during its life cycle (2216:56, 2222:40, 2228:11, and 2234:01 UTC). Each colored line represents a different time (see legend for the time corresponding to each color), and each point on each line represents a different elevation angle from 0°-26°. Distances given are radar-relative; the x-axis represents the vortex's east-west distance from the MWR-05XP, and the y-axis represents its north-south distance from the MWR-05XP. The inset image is a proximity hodograph for Norman, OK, from the RAP model valid at 2200 UTC 6 May 2015.

(2014) and Griffin et al. (2019), the Amber-Bridge Creek tornado exhibited significant tilt well before dissipation. Also as in Griffin et al. (2019), the northeastward tilt of the vortex, which is a common trait in Northern Hemisphere supercellular tornadoes, closely followed the direction of the 0-6 km environmental wind shear vector (not shown) and, in a broad and qualitative sense, the Rapid Refresh (RAP) model proximity hodograph at Norman, OK, valid at 2200 UTC 6 May 2015 (Fig. 3.9).

In the lowest levels, vortex tilt was often chaotic and varying, including tilt toward the northwest at 2216:56 UTC and tilt toward the west or southwest at 2222:40 and 2228:11 UTC (Fig. 3.9). This could be due to the increasing effects of surface friction as the tornado encountered buildings and homes within Bridge Creek after traversing lower-friction terrain southwest of town. Debris accumulation within a vortex's surface layer has been shown to alter the flow structure of the vortex within a few hundred meters of the surface (Lewellen et al. 2008). As the tornado weakened, the motion of the low-level vortex attained a northward (leftward) component, in contrast to the movement of the upper levels of the vortex, which continued to move toward the east-northeast. In turn, the overall vortex became more tilted, exhibiting approximately 65° of tilt from due north in its lowest half and 90° (nearly due east) in its upper half at 2234:01 UTC (Fig. 3.9). It appears as if the tornado was becoming sheared out, perhaps owing to influences of the RFGF (to be discussed in section 3.3.5) on the near-surface vortex.

3.3.3 Vortex Periodicity

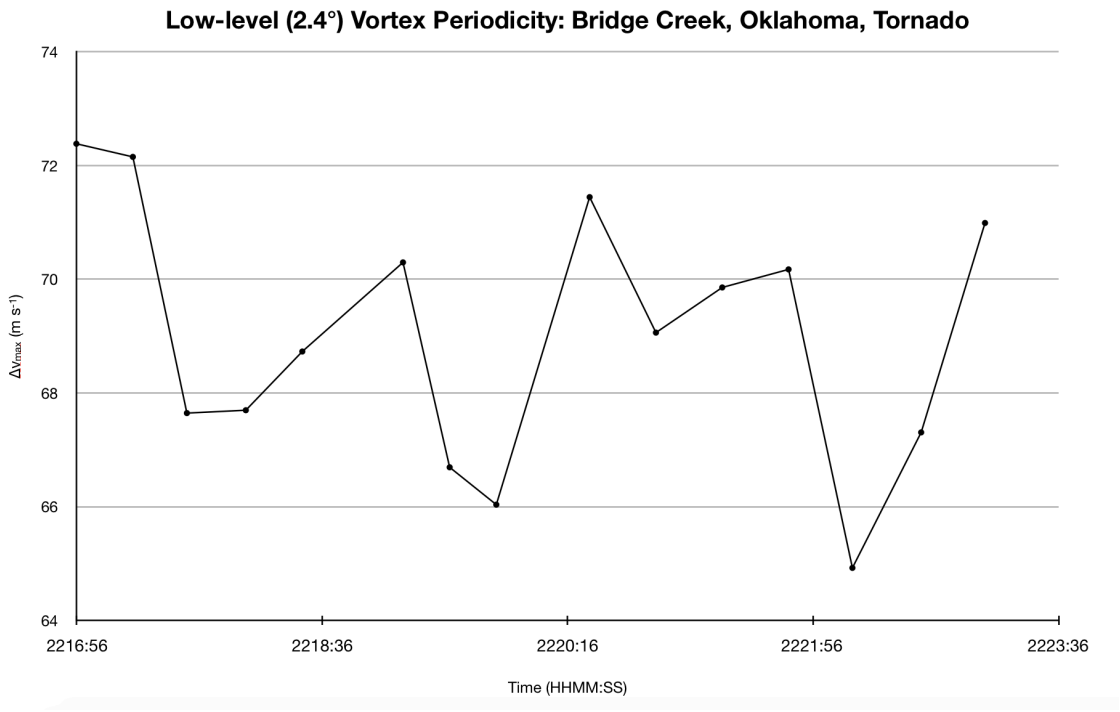

Figure 3.10: Graph of Δv_{max} at 2.4° (0.3 km ARL) from 2216:56-2223:06 UTC.

Between 2216:56 and 2223:06 UTC, the TVS exhibited slight periodicity in low-level (2.4°; 0.3 km ARL) vortex intensity, as illustrated in Fig. 3.10. The oscillations were characterized by an amplitude that varied between 2 and 3 m s^{-1} at a period of 100-145 s. Similar periodicity was observed in the Goshen County, WY, tornado during VORTEX2, as discussed in Wurman et al. (2013). In that study, a DOW radar documented periodicity with an amplitude of approximately 4 m s^{-1} at a period of 66-108 s within the Goshen County tornado. As hypothesized by Wurman et al. (2013), these fluctuations appeared to be the result of longer-wavelength, Rossby-type waves slowly revolving around the vortex, rather than subvortices that orbit the main tornadic vortex at much higher speeds. The oscillations in the RaXPol Doppler velocity data could also be the result of centrifugal waves (Fiedler 1998, Shapiro 2001); however, this cannot be determined quantitatively in this case.

Despite the observed periodicity, the oscillations within the Amber-Bridge Creek tornado may not be significant. Between 2216:56 and 2223:06 UTC, the tornado was moving over the town of Bridge Creek, which suggests that the periodicity may have been the result of lofted debris impacting the flow within the vortex, or changing velocity biases caused by debris centrifuging, rather than self-imposed changes in vortex dynamics. In addition, as the tornado traversed the radar domain, the geometry of its flow field relative to the radar volumes may have changed (e.g., the peak winds within the TVS at a given time may have ended up on the edge of a radial, yielding potentially weaker Δv_{max}). These hypotheses, coupled with the low-amplitude nature of the oscillations, could suggest that the periodicity was an artifact; however, it bears consideration and perhaps further investigation nonetheless.

3.3.4 Weak-echo Column

A weak-echo hole (WEH) was coincident with the TVS at all elevation angles through the entirety of D1 and much of D2, comprising a weak-echo column (WEC). WEHs were surrounded by annuli of high reflectivity, similar to Wurman and Gill (2000), and exhibited negative reflectivity at their centers. Therefore, for simplicity and due to the higher beamwidth (and resultant coarser resolution relative to RaXPol) of the MWR-05XP, WEHs were subjectively demarcated by the region surrounded by the 0-dBZ isoecho coincident with the TVS evident in radial velocity data. The greatest diameter normal to the radar beam across the 0-dBZ isoecho will be reported as a particular WEH's width (Bluestein et al. 2004).

Throughout the deployment periods, the WEH underwent several fluctuations in size. During D1, the WEH at 0.3 km ARL (2.4°)[2] expanded from approximately 250 m at 2213:21 UTC to its relative widest within D1 of 600 m at 2214:58 UTC (Fig. 3.11). This is coincident with a slight increase in Δv_{max} and the beginning of the strengthening phase discussed in section 3.3.2. As the strengthening phase continued, the width of the WEH at 0.3 km ARL (2.4°) decreased for the remainder of D1 to about 250 m at 2216:19 UTC (Fig. 3.11), perhaps because of an increase in lofted debris or convergence of debris within the surface friction layer (Bluestein et al. 2007, 2019). At nearly all scan times in D1 (with the exception of 2214:58 and 2215:14 UTC), the vortex diameter exceeded the width of the WEH at this height, which is consistent with the findings of Bluestein et al. (2007). In general, the WEH was slightly wider and did not undergo as significant fluctuations in size in the mid- and upper levels of the column (Fig. 3.11) as it did in the low-levels throughout the deployment periods. Fig. 3.12 illustrates the associated velocity imagery at the same times and elevation angles as the reflectivity imagery in Fig. 3.11, showing that the intensity of the TVS remained fairly steady at all levels throughout D1.

Sequences of reflectivity and velocity images featuring the WEH at 0.3, 1.5, and 3 km ARL (2.4°, 10.2°, and 19.7°, respectively) from the beginning of D2 through several minutes after tornado dissipation are shown in Figs. 3.13 and 3.14. At 0.3 km ARL (2.4°), the WEH dissipates by 2218:05 UTC, reappears at 2219:09 UTC, and then dissipates once again by 2221:46 UTC. The initial dissipation of the low-level WEH was coincident with an efflux of precipitation from the hook echo toward the radar, which appears to be a

[2] The lowest elevation angle is not low enough to detect any filling of the WEH due to frictional inflow.

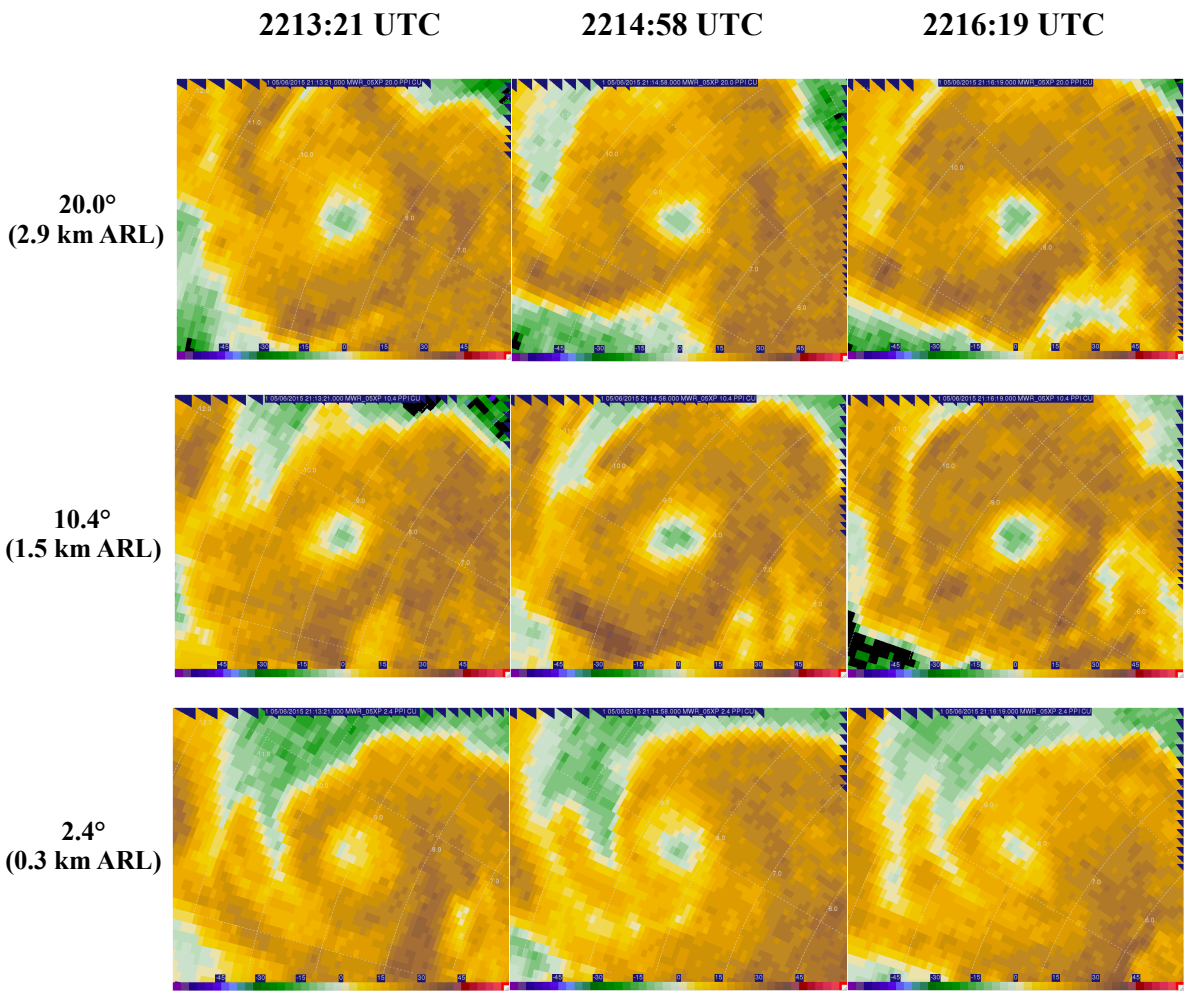

Figure 3.11: Evolution of the weak-echo hole coincident with the Amber-Bridge Creek tornado at three different times during D1 (2213:21, 2214:58, and 2216:19 UTC) using reflectivity imagery (from bottom to top) at 2.4°, 10.4°, and 20.0°. Range rings are included at 1-km increments.

secondary RFD surge. This feature will be discussed in depth in section 3.3.4. No low-level WEHs were evident for the remainder of the tornado's life cycle; however, after the tornado dissipated, a WEH reappeared from 2227:36-2231:59 UTC and then again from 2233:09-2234:19 UTC. The provides additional evidence that the mesocyclone remained at tornadic intensity well after the dissipation of the tornado and, likely, was simply cycling (NWS Norman (2015) confirmed three subsequent tornadoes that occurred from

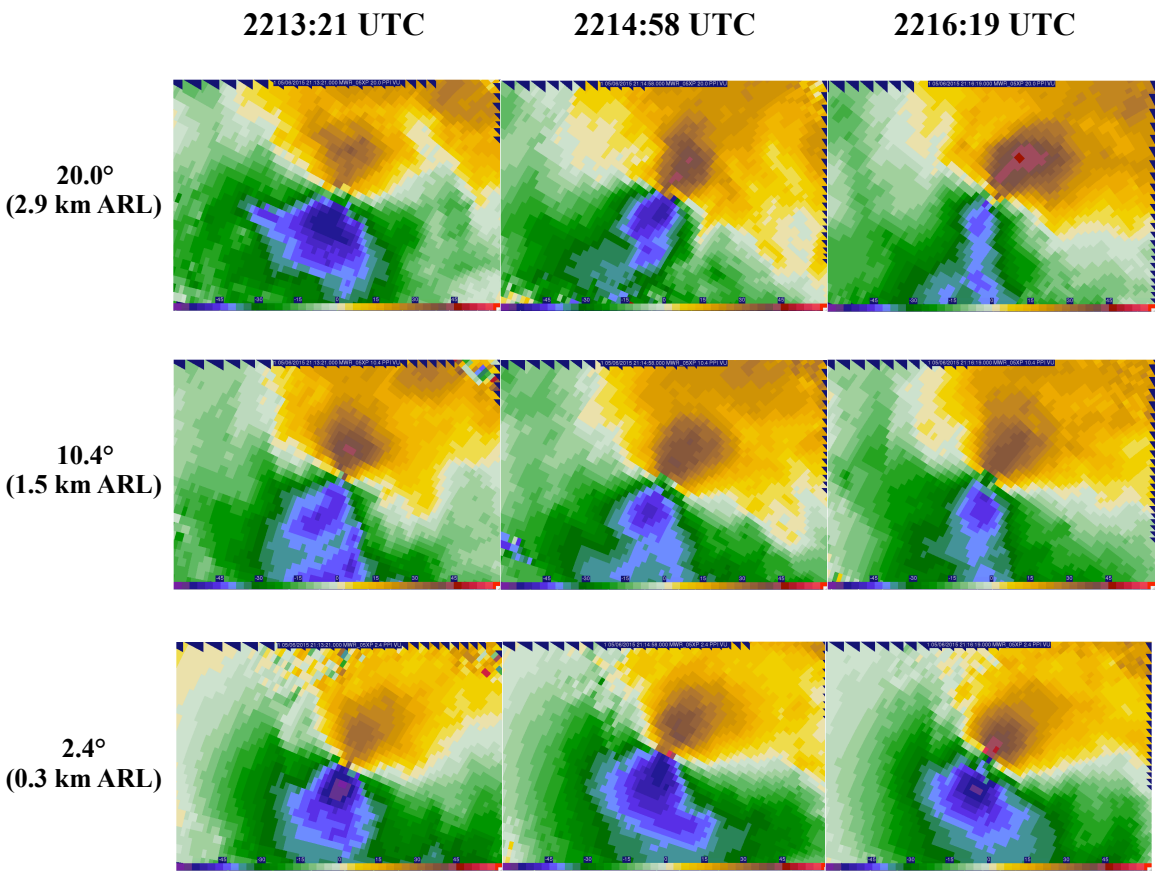

Figure 3.12: As in Fig. 3.11, but with velocity imagery.

this storm from 2233-2235 UTC, at 2246 UTC, and from 2253-2310 UTC, none of which were analyzed in this study). In addition, the resurgence of the WEH may be the result of a downdraft of echo-free air from aloft, signifying sinking motion within the vortex. The WEHs at 1.5 km ARL (10.2°) and 3 km ARL (19.7°) were much wider (maximum diameter of approximately 1 km at each elevation) than that at 0.3 km ARL (2.4°) throughout D2 (except for around 2230 UTC); of these three elevations, measurements of the diameter of the WEH at 3 km ARL (19.7°) generally featured were the widest, followed by 1.5 km ARL (10.2°) and then 0.3 km ARL (2.4°). This may have occurred because the vortex was highly tilted, yielding horizontal smearing of the WEH. In

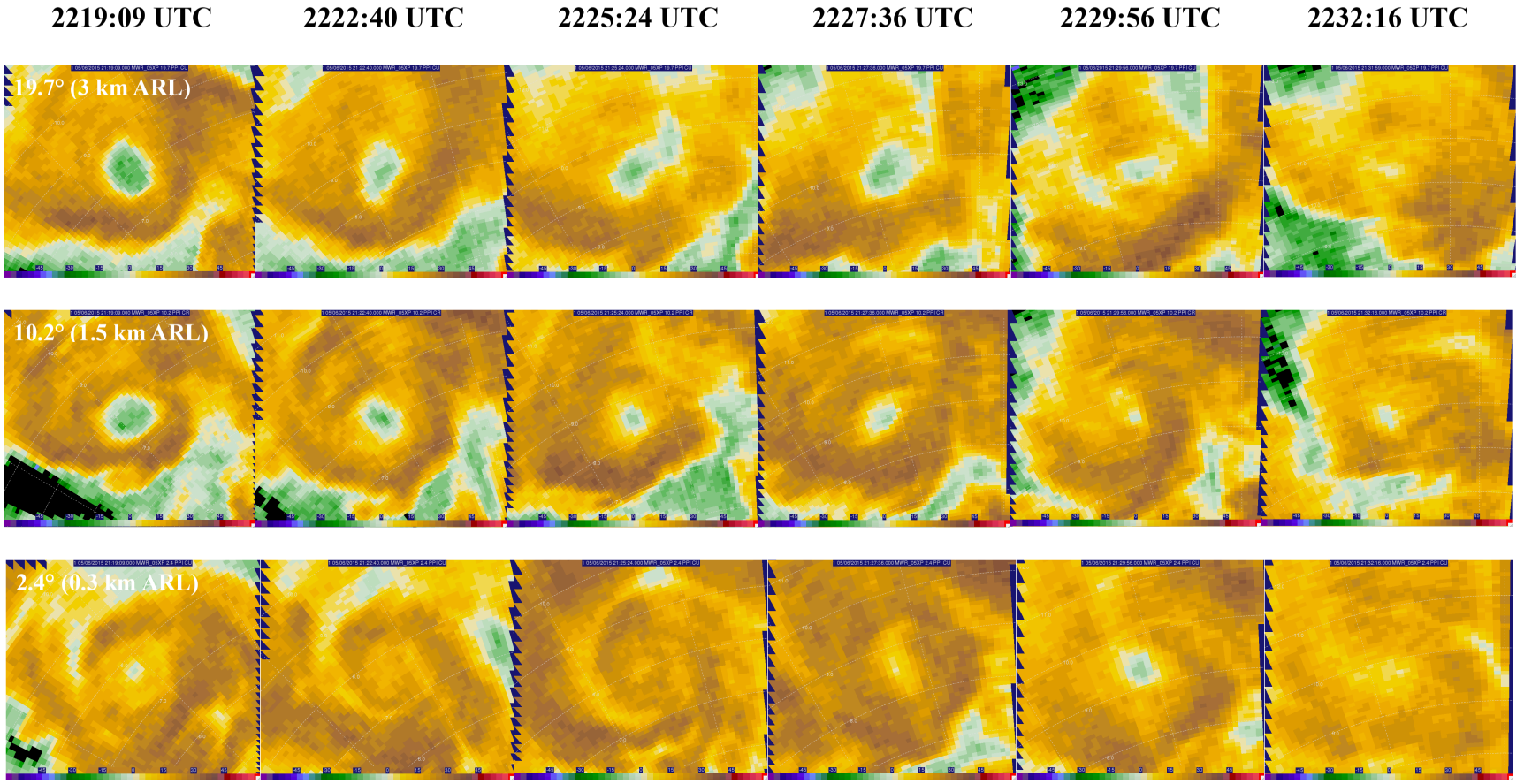

Figure 3.13: As in Fig. 3.11, but for six different times during D2 (2219:09, 2222:40, 2225:24, 2227:36, 2229:56, and 2232:16 UTC) at (from bottom to top) 2.4°, 10.2°, and 19.7°. Range rings are included at 1-km increments.

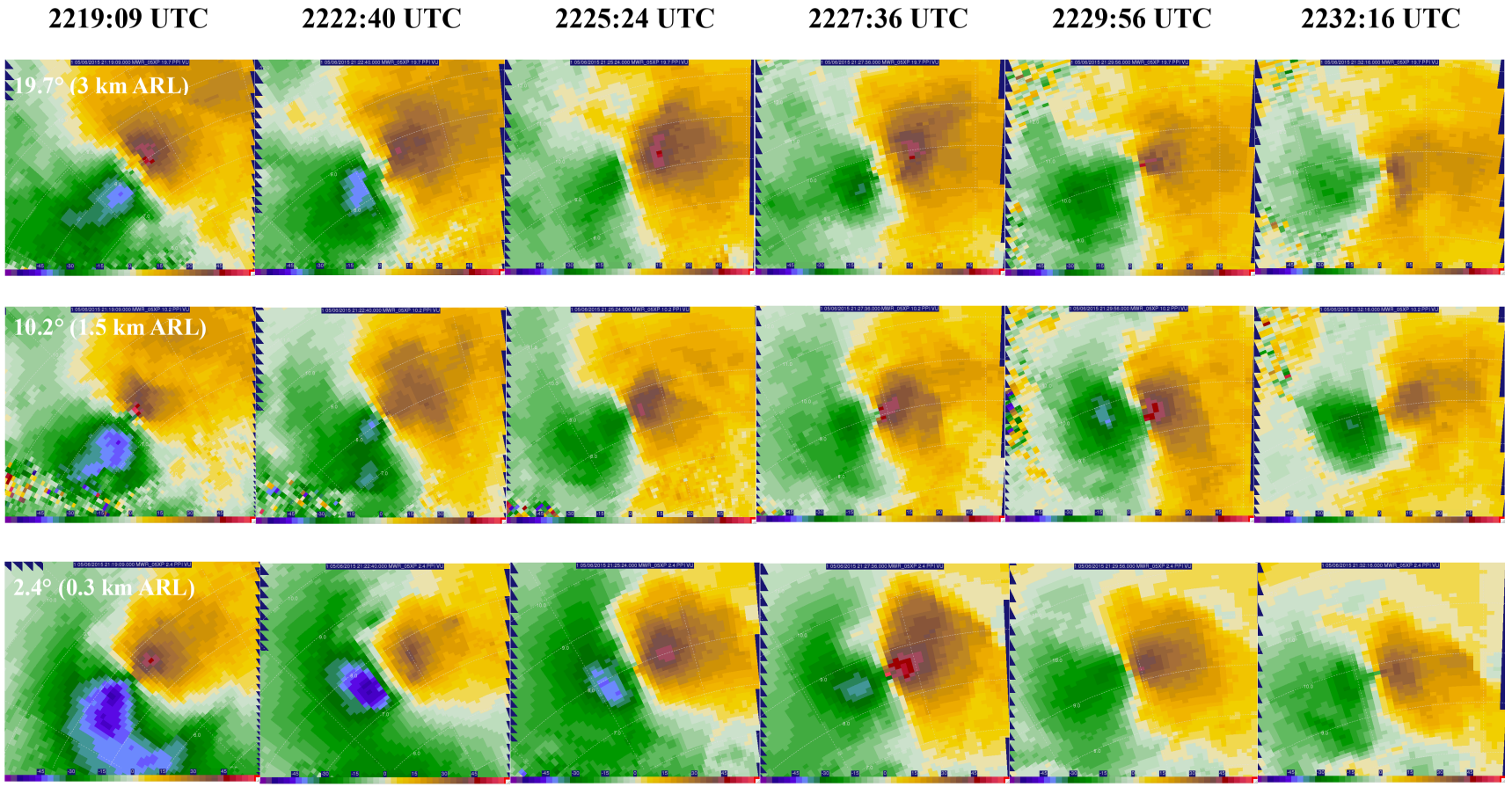

Figure 3.14: As in Fig. 3.13, but with velocity imagery.

contrast, Bluestein et al. (2004) discovered a pear-shaped WEC coincident with a tornado near Happy, TX, on 5 May 2002 that was 40% wider approximately 100 m AGL than it was above.

3.3.5 Secondary RFD Surge

From 2217:41-2222:40 UTC, an area of enhanced reflectivity and velocity surged outward (toward the radar) from the southern and eastern flanks of the hook echo. This appears to be a clear example of a secondary rear-flank downdraft (SRFD) surge, as previously documented by Marquis et al. (2008), Lee et al. (2012), Schenkman et al. (2014), Skinner et al. (2014), Mashiko (2016), and others. Fig. 3.15 illustrates the progression of the SRFD surge over its approximately 5-minute duration at 0.3 km ARL (2.4°). Initially, a band of slightly enhanced reflectivity becomes apparent within the hook echo in the vicinity of the ongoing tornado at 2217:41 UTC (Fig. 3.15a). By 2219:09 UTC, this band detaches from the hook echo (Fig. 3.15b) and then surges outward over the remainder of its duration (Fig. 3.15c-e), eventually overtaking the southern portion of the primary RFD gust front (PRFGF) by 2221:19 UTC. The composite RFD gust front then bulges outward (Fig. 3.15e). Lee et al. (2012) identified a minimum difference in radial velocity across the SRFD gust front (SRFGF) of 13 m s^{-1} as the threshold for deeming a momentum surge within the primary RFD as a SRFD surge. In the case of the Amber-Bridge Creek supercell, this threshold was easily exceeded[3]. The position of the PRFGF and SRFGF were determined using this criterion, which was

[3] In some spots, the velocity associated with the SRFD surge was normal to the radar beam and, thus, was not directly detectable here.

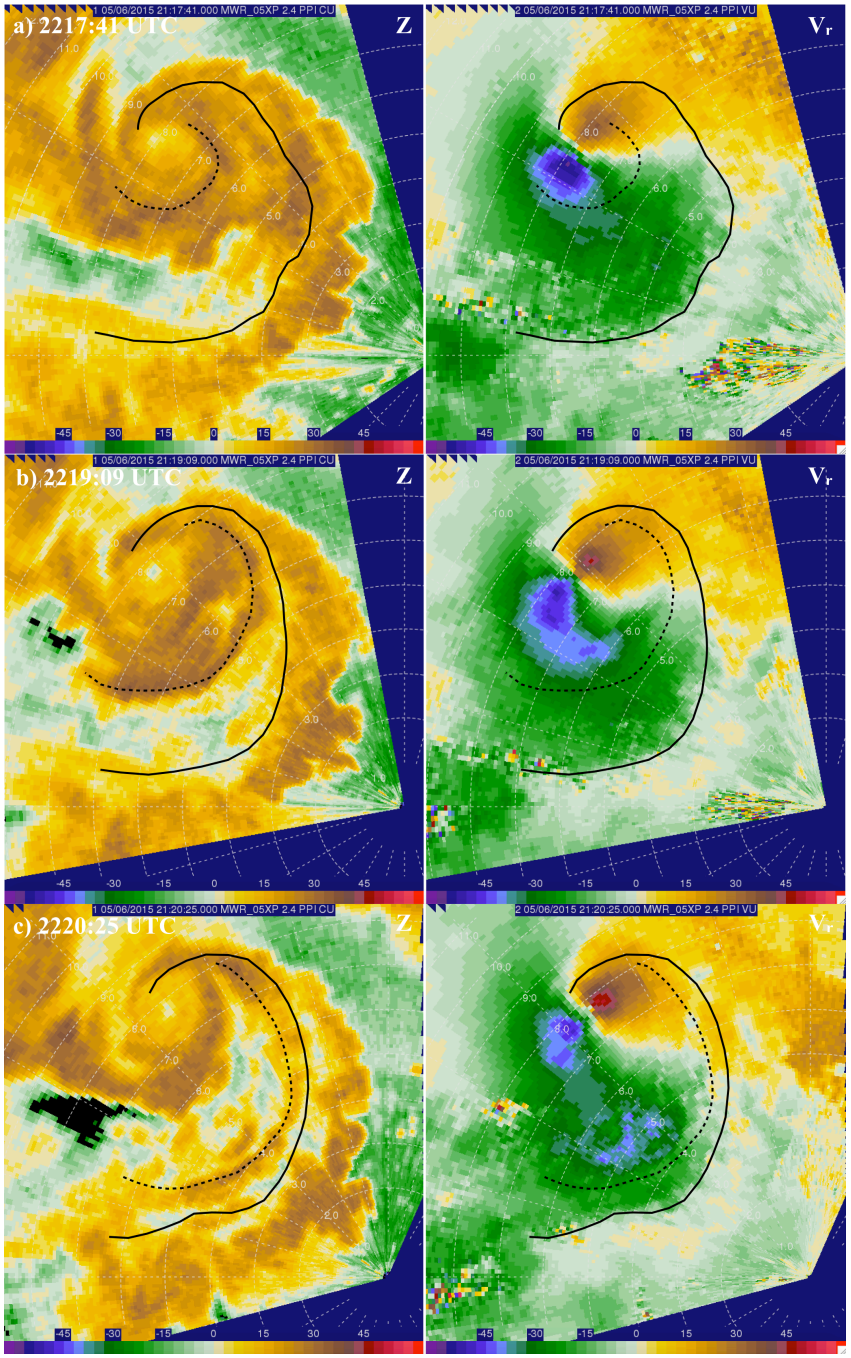

Figure 3.15: Evolution of the SRFD surge using reflectivity (dBZ, left) and radial velocity (m s^{-1}, right) images from 0.3 km ARL (2.4°) at five different times throughout the duration of the surge: a) 2217:41, b) 2219:09, c) 2220:25, d) 2221:19, and e) 2222:40 UTC. The dashed (solid) black line indicated the approximate location of the SRFGF (PRFGF). Note the bulge in the composite RFD gust front in (e). Range rings are included at 1-km increments.

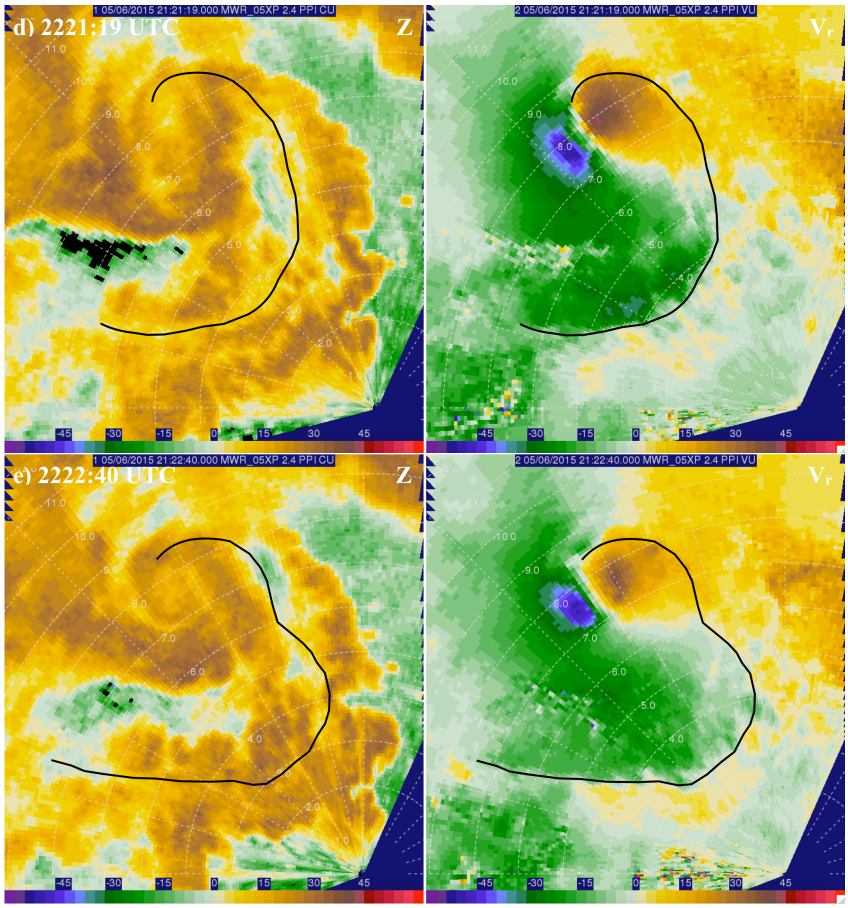

Figure 3.15 (continued).

satisfied for approximately half of the points on each boundary. The remainder of the points were determined through subjective analysis by the author.

During the SRFD surge, the TVS underwent some changes in behavior and composition. Inbound velocities within the TVS decreased from 43 m s^{-1} at 2216:56 UTC (prior to the start of the SRFD surge) to 32 m s^{-1} at 2219:47 UTC (2 min after the surge began). Meanwhile, outbound velocities increased from 26 to 33 m s^{-1} over the same period. Perhaps the increased low-level convergence along the SRFGF aided in tornado maintenance (Marquis et al. 2012), but it is unclear why only the outbound velocities increased. Approximately 2 min after the onset of the SRFD surge, the TVS attained a

slightly greater northward component of motion and moved to the left of its previous track, at which point the first signs of the tornado decay process appeared. It is unclear whether or not the SRFD surge caused this left turn. SRFD surges have been associated with tornado dissipation when the SRFGF wraps completely around a tornado or when the SRFD surge contains more hostile thermodynamic properties than those of the primary RFD (Marquis et al. 2012, Lee et al. 2012). However, the former was not apparent in the radar data, and, as previously mentioned, the tornado decay phase did not begin until about 2221 UTC, when midlevel Δv_{max} first began to decrease. At this point, the SRFGF was well removed from the hook echo and was about to merge with the PRFGF. Therefore, it does not appear that the SRFD surge played a significant role in tornado decay, although the SRFGF may have been associated with the leading edge of a less hospitable thermodynamic environment that may have eventually aided in tornado dissipation.

3.3.6 (Scalloped) Primary RFD Gust Front and Associated Vortices

The PRFGF of the Amber-Bridge Creek supercell was unique in that it featured significant scalloping of the leading edge of the region of high reflectivity associated with it and numerous attendant vortices. Scalloping occurred through the entirety of D1 and much of D2, while vortices were only evident during D1. After 2223:06 UTC, the MWR-05XP did not record data in the PRFGF due to changes in which sectors were being scanned. Some degree of scalloping was also evident through the entire depth of

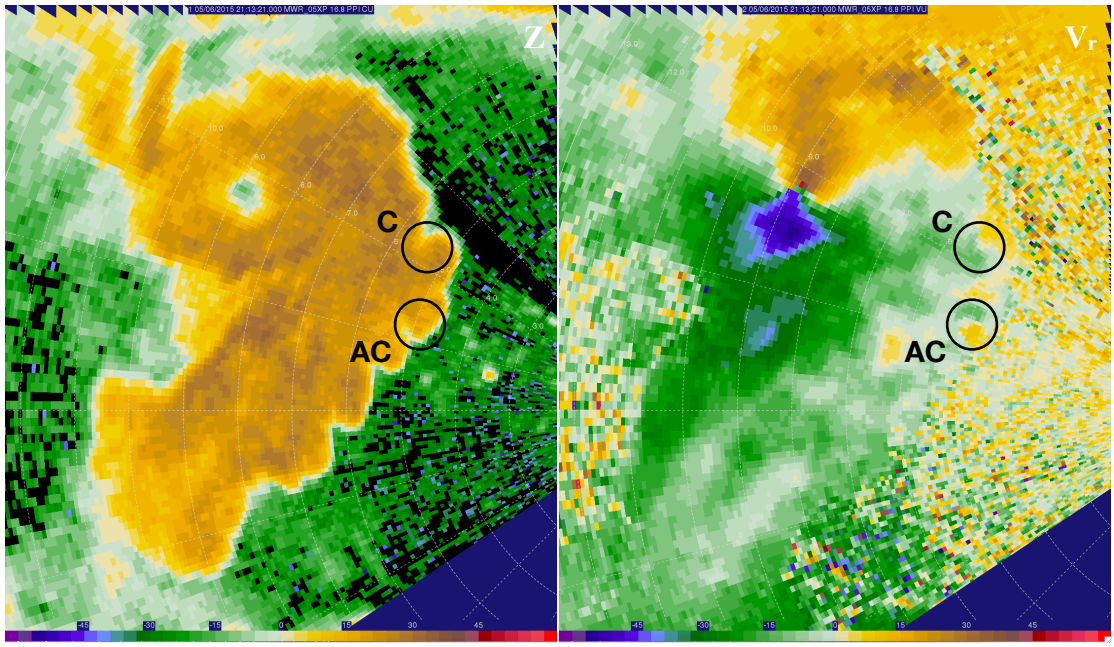

Figure 3.16: Reflectivity (dBZ, left) and radial velocity (m s^{-1}, right) at the 16.8° elevation angle (2.5 km ARL) at 2213:21 UTC. Counterrotating vortices are denoted by black circles, the cyclonic member labeled "C" and the anticyclonic member labeled "AC." Range rings are included at 1-km increments.

the radar volumes in each deployment period, and vortices were apparent above approximately 1.5 km ARL (10.4°) and most evident at about 2.5 km ARL (16.8°).

As in Bluestein et al. (1997) and Straka et al. (2007), there was at least one instance of counterrotating vortices occurring simultaneously along the PRFGF (Fig. 3.16). Both vortices were coincident with kinks in the PRFGF, and their diameters varied between 300 and 700 m. From the beginning of D1, these vortices lasted approximately 1.5 min, and, although vortices of this type can sometimes attain tornado intensity (Bluestein et al. 1997), they remained subtornadic throughout their lifespan. The cyclonic vortex was located approximately 3.5 km east-southeast of the Amber-Bridge Creek tornado, and the anticyclonic vortex was located about 2 km south of its cyclonic counterpart. As these vortices dissipated, three new vortices, all cyclonic, formed along

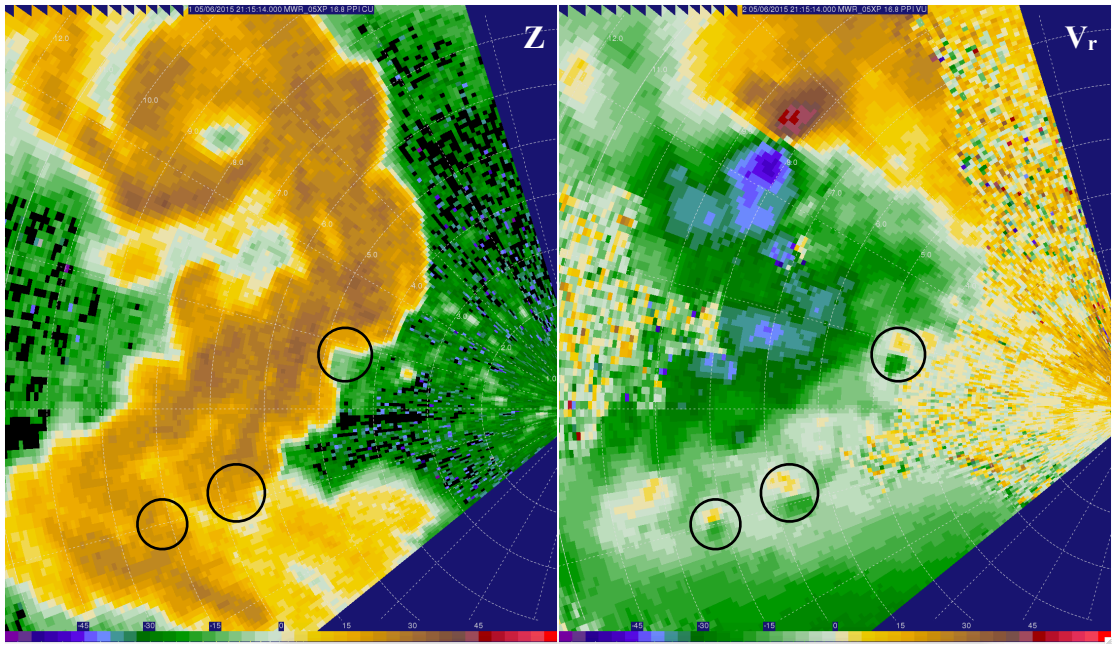

Figure 3.17: Reflectivity (dBZ, left) and radial velocity (m s^{-1}, right) at the 16.8° elevation angle (2.5 km ARL) at 2215:14 UTC. Vortices along the PRFGF are denoted by black circles. Range rings are included at 1-km increments.

the southern portion of the PRFGF (Fig. 3.17). By 2215:14 UTC, precipitation from storms to the south of the Amber-Bridge Creek supercell began to degrade the structure of the PRFGF where the southernmost two vortices were located; however, kinks in the PRFGF were present prior to the formation of these two vortices. Each of the three vortices were on the order of 200-400 m and remained subtornadic; the northernmost vortex was the strongest, exhibiting Δv_{max} of 33 m s^{-1} at 2215:14 UTC, and was coincident with a significant reflectivity notch. Similar to the counterrotating vortices, these vortices were transient, lasting between 1-1.5 min.

Vortices along RFD gust fronts in supercells have previously been observed (e.g. Bluestein et al. 2003, Tanamachi et al. 2013) and simulated (Straka 2007); however, in many cases, they are most prominent near the surface and may manifest as gust-front tornadoes (Finley and Lee 2004, 2008). In the case of the Amber-Bridge Creek supercell,

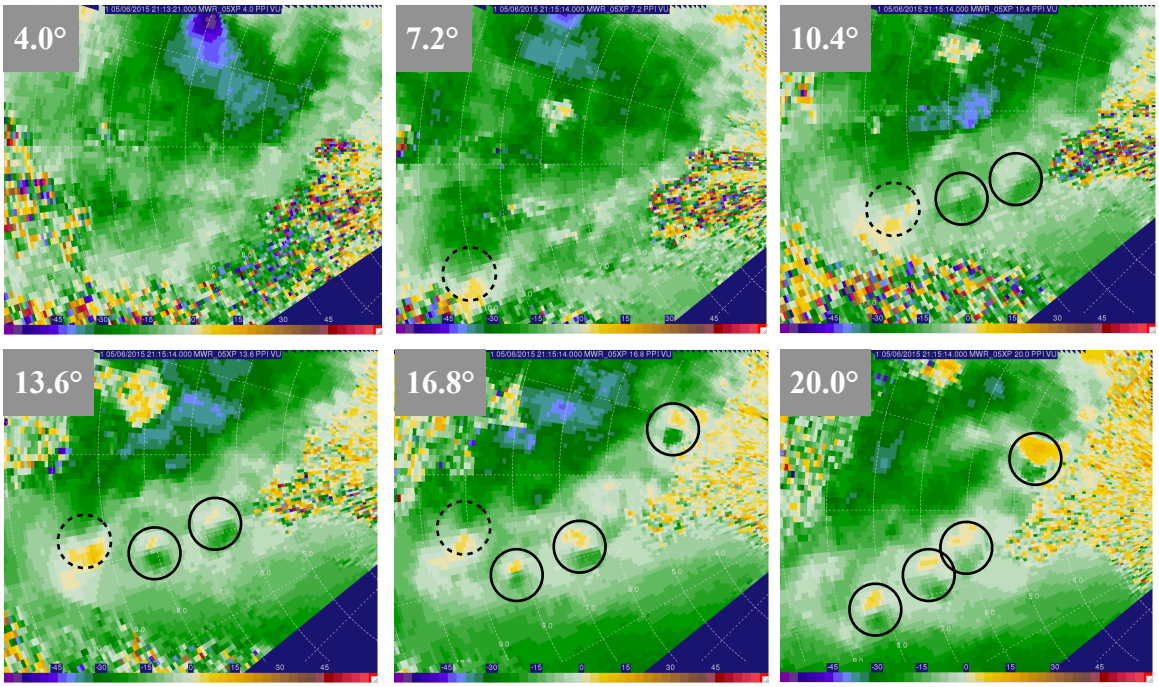

Figure 3.18: Radial velocity (m s^{-1}) at 3.2° increments from 4.0-20.0° at 2215:14 UTC. Cyclonic (anticyclonic) vortices along the PRFGF are denoted by solid (dashed) black circles. Range rings are included at 1-km increments.

PRFGF vortices were only apparent in the mid- and upper-levels of the radar volumes (Fig. 3.18). While the specific genesis mechanism for these vortices is unknown, it is plausible that they resulted from shearing instability along the leading edge of the PRFGF, as in Tanamachi et al. (2013), since the vortices were only evident aloft and the effects of surface friction, which has been found to create near-surface horizontal vorticity and attendant mesovortices (Schenkman et al. 2012), decrease with height. For the counterrotating vortices shown in Fig. 3.16, perhaps more likely is that they were the result of the tilting of horizontal vorticity into the vertical by horizontal gradients in vertical velocity. In addition, since the PRFGF extends to at least 3 km ARL, it may actually be a deep convergence zone as described by Lemon and Burgess (1993), Lemon and Parker (1996), and Bluestein and Gaddy (2001).

Chapter 4

The Putnam, OK, Tornadic Supercell: 15 June 2019

4.1 Synoptic Overview

Unlike the 6 May 2015 case, the 15 June 2019 event featured weak (10 m s^{-1} or less), quasi-zonal 500-mb flow across the western half of the United States, save for a low-amplitude, eastward-moving impulse encroaching upon the Texas Panhandle by 0000 UTC 16 June (Fig. 4.1a). Southeasterly surface flow of 5 m s^{-1} and southerly 850-mb flow of 10-12 m s^{-1} (Fig. 4.1b) contributed to only modest deep-layer and low-level wind shear (Fig. 4.1c and d), supportive of mainly multicells, across Oklahoma. Despite the lack of a concentrated lee cyclone, a seasonably moist low-level airmass was already in place across the southern Great Plains. The 0000 UTC sounding from Norman, OK (Fig. 4.3), sampled a surface dewpoint of 74°F (23°C) beneath a deep elevated mixed layer (EML; 700-500 mb lapse rate of 8.2°C km^{-1}), which yielded an extremely unstable environment (MLCAPE of 4235 J kg^{-1}).

At the surface, a stationary front was located across northwestern Oklahoma, and a diffuse outflow boundary from overnight convection, evident in mesoscale but not synoptic-scale observations, was draped, roughly, from west to east across northwest and

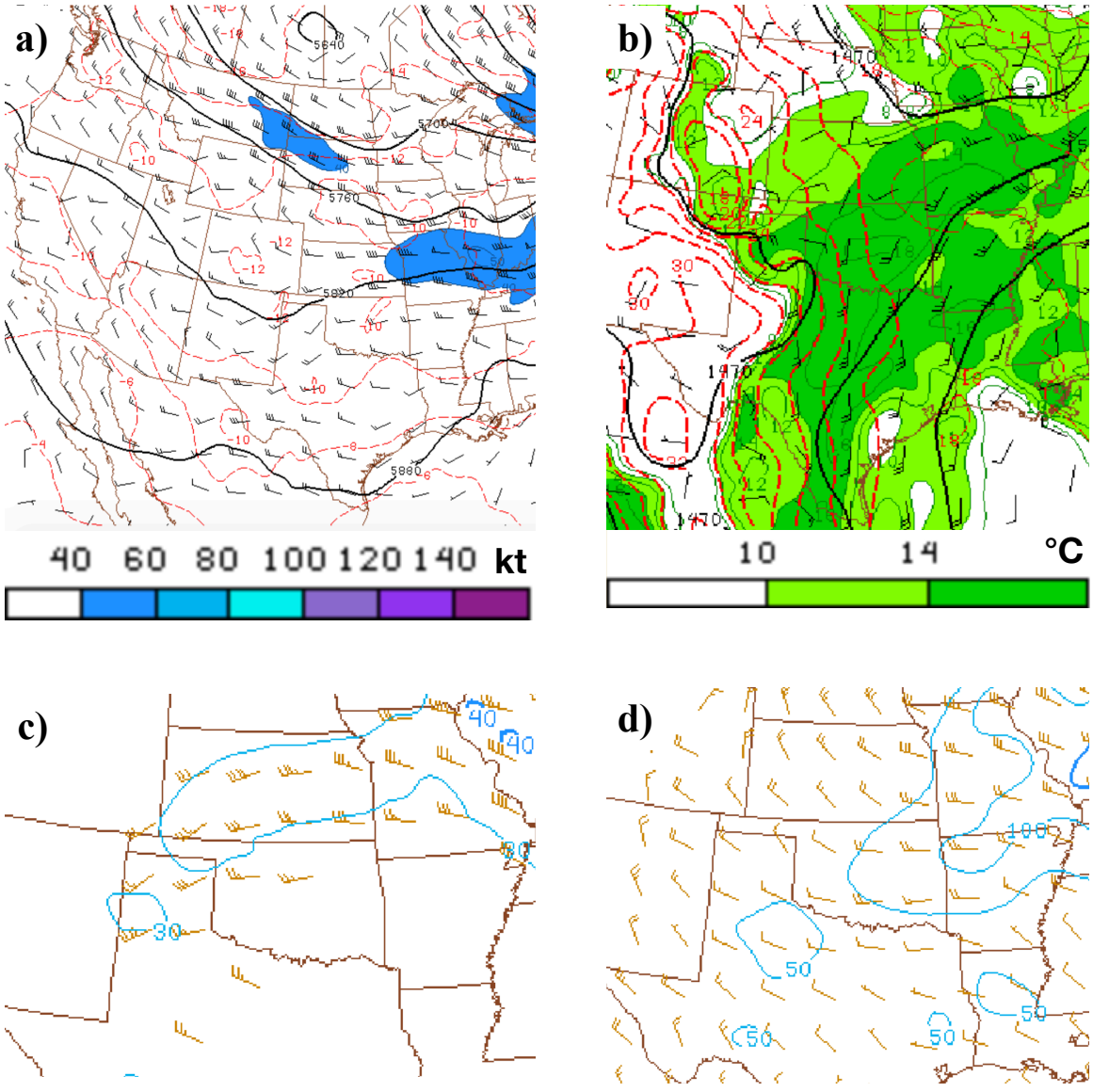

Figure 4.1: Overview of the synoptic environment at 0000 UTC 16 June 2019. Pictured above are a) 500 mb winds, b) 850 mb winds and moisture, c) effective bulk wind shear, and d) 0-1 km storm-relative helicity. Adapted from the Storm Prediction Center Mesoanalysis Archive.

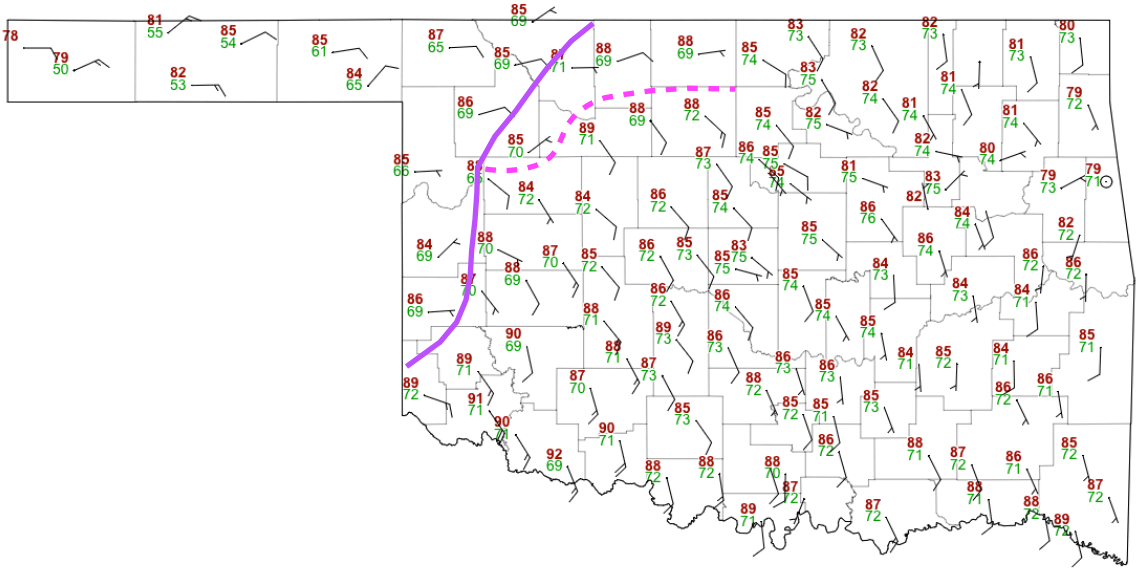

Figure 4.2: Map of surface temperature (°F, red values), dewpoint (°F, green values), and wind speed and direction from the Oklahoma Mesonet valid at 0007 UTC 16 June 2019. The solid purple line represents the approximate location of the stationary front, and the dashed pink line denotes the approximate location of the diffuse mesoscale boundary.

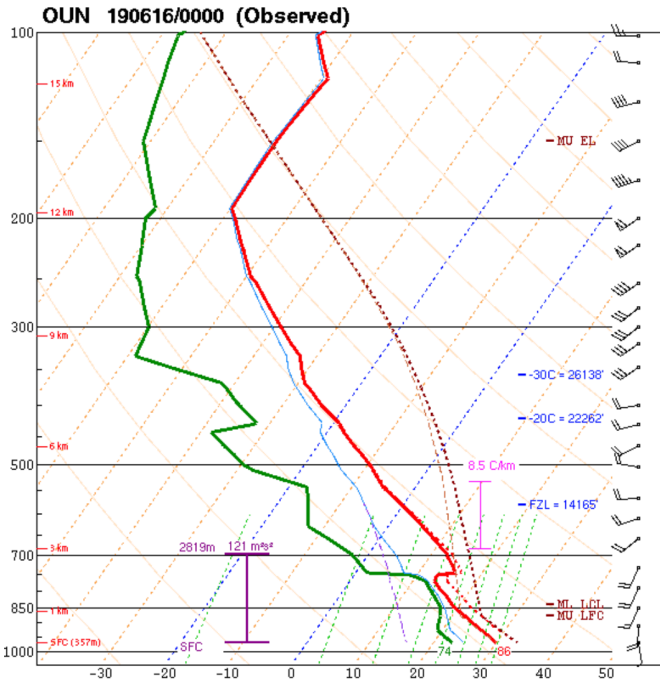

Figure 4.3: KOUN (Norman, OK) sounding taken at 0000 UTC 16 June 2019. Taken from the Storm Prediction Center Severe Weather Events Archive.

northern Oklahoma (Fig. 4.2). This boundary was represented by solely a wind shift and surface convergence, rather than the interface between air masses with differing characteristics, as described in Sanders and Doswell (1995), and it may have locally enhanced low-level shear in its vicinity amid the overall dearth of deep-layer shear, producing an environment more favorable for supercells. The EML suppressed convective initiation until 2300 UTC after a combination of daytime heating and ascent associated with the aforementioned weak shortwave impulse eroded the capping inversion.

4.2 Supercell Formation and Evolution

An area of showers first developed just north of Weatherford, OK by 2300 UTC, followed by more isolated development to the northeast near Fairview, OK, by 2330 UTC. Given the highly unstable environment, these showers rapidly developed into strong multicell storms. The northern storm very slowly intensified after splitting, while the storms to its south further strengthened, organizing into semi-discrete storms with marginal supercell characteristics by 0035 UTC 16 June. A new storm along the forward flank of the southernmost supercell sprouted and quickly became dominant, undergoing a rapid increase in low- and midlevel rotation and developing an appendage on its southwestern flank between 0121 and 0132 UTC. Often a precursor to tornadogenesis (Perez et al. 1997), cloud-to-ground lightning activity then increased significantly, and a rotating wall cloud became visible (Fig. 4.4). With only weak upper-level flow, this storm was nearly stationary; however, once low-level rotation increased, it began to propagate

Figure 4.4: Wide-angle image taken at 0159:43 UTC of the Putnam supercell with a positive cloud-to-ground lightning bolt. Note the wall cloud at the lower right of the image. Photograph courtesy of Brett Wright.

very slowly to the south. The supercell produced an EF1 tornado from 0140-0150 UTC 4 km southeast of Putnam, OK, and low-level rotation remained intense after it dissipated. Fig. 4.5 shows the evolution of the Putnam supercell using reflectivity imagery from the KVNX radar.

4.3 The Putnam Tornadoes

RaXPol initially targeted the isolated development northeast of Fairview, OK; however, once this storm split and began to decay, the storm intercept crew abandoned it

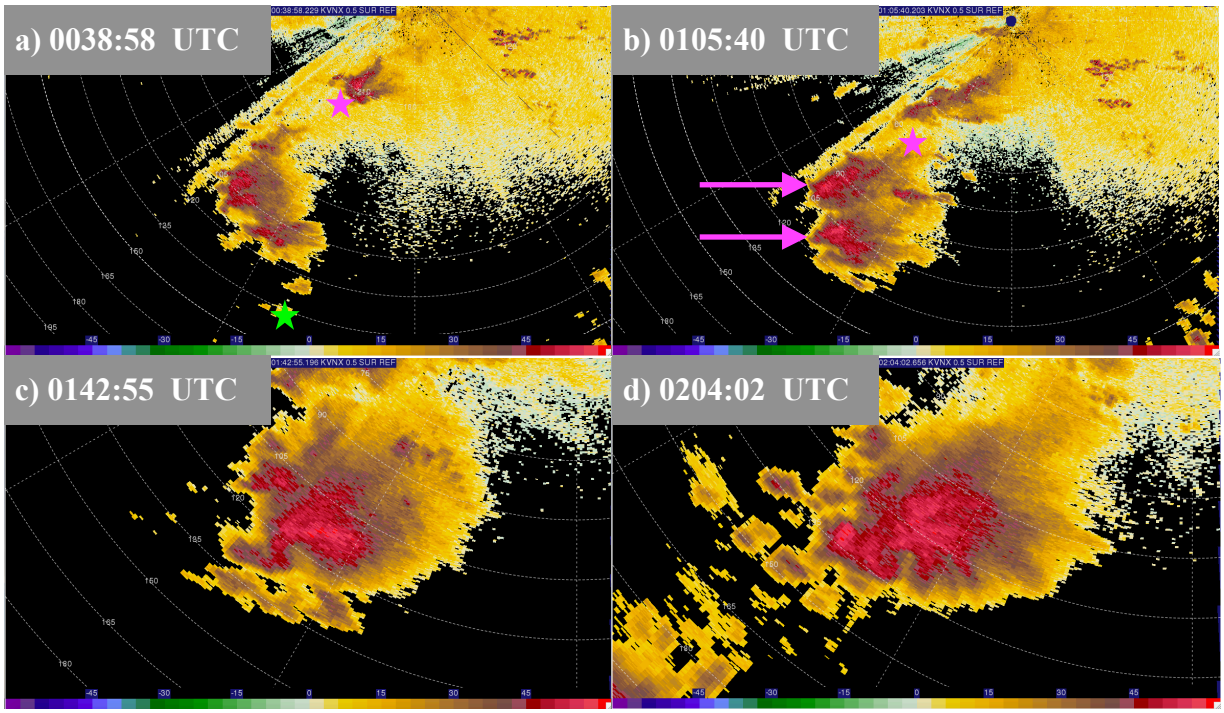

Figure 4.5: Evolution of the Putnam supercell using 0.5° reflectivity (dBZ) data from the KVNX radar. Included are a) the initial storms north of Weatherford, OK (green star), and the isolated storm near Fairview, OK (pink star), at 0038:58 UTC, b) the organization of the southern storms into two semi-discrete supercells (pink arrows) at 0105:40 UTC, c) the Putnam supercell with well-defined hook echo as it was producing its first tornado at 0142:55 UTC, and d) the supercell at 0204:02 UTC, immediately prior to the genesis of the first tornado analyzed in this study. Each panel follows the storm as it moves; therefore, the area displayed in each panel is different.

and repositioned to intercept the southern supercell (this storm will be referred to as the "Putnam supercell"). While in transit, the aforementioned EF1 tornado southeast of Putnam occurred; therefore, no data encompassing tornadogenesis were collected. RaXPol was deployed three different times along Oklahoma State Highway 54 as shown in Fig. 4.6. The first deployment (D1) occurred 2.5 km east of Thomas, OK, from 0157:14-0206:20 UTC, the second (D2) occurred 5.8 km southeast of Thomas from 0211:31-0217:46 UTC, and the third (D3) occurred 10.4 km south-southeast of Thomas from 0223:38-0236:59 UTC. At 0202:34 UTC, RaXPol began scanning up to 20° in

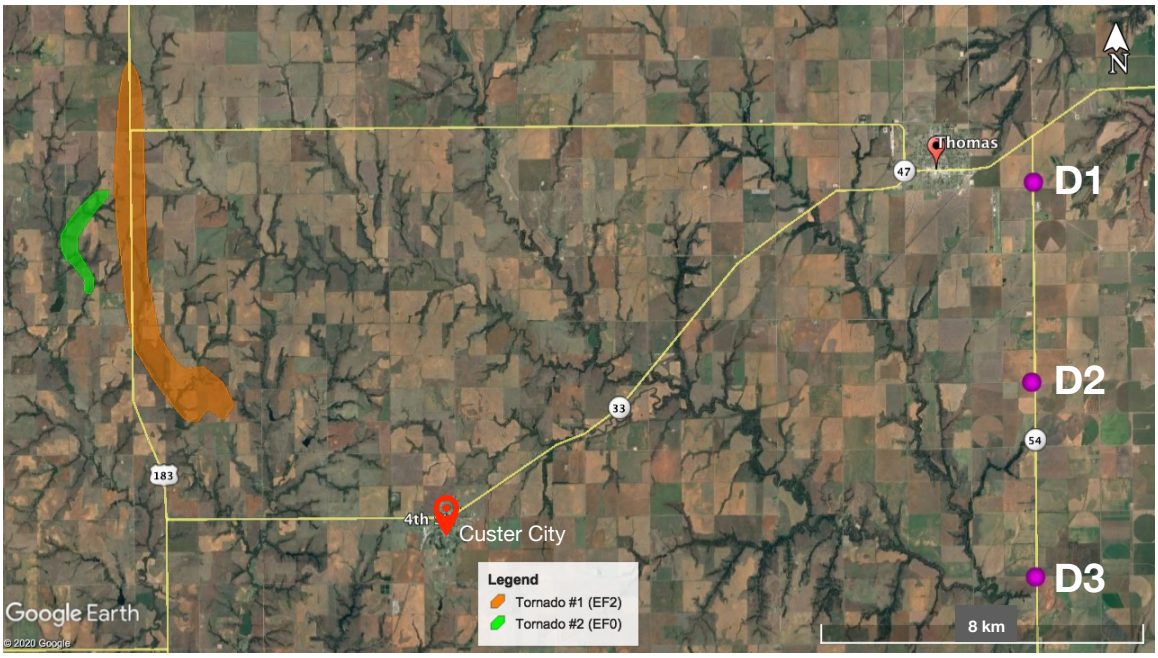

Figure 4.6: RaXPol deployment map for 15 June 2019. Pink dots represent the locations of each RaXPol deployment, which are labeled. The surveyed damage paths of the tornadoes documented by RaXPol are overlaid; the orange polygon is the path of tornado #1, and the green polygon is the path of tornado #2.

elevation (in increments of 2°), as opposed to the previous maximum height of 8° (in increments of 1°); at 0215:32 UTC, the scanning strategy was changed back to the original 8° mode. During D3, the Putnam supercell was absorbed by an eastward-moving mesoscale convective system (MCS), and tornadic activity was not observed; therefore, D3 will be omitted from this study.

According to NWS Norman (2019), the Putnam supercell spawned two tornadoes during the RaXPol deployment period: an EF2 (referred to as tornado #1 herein) that traveled from 14.5 km north-northwest to 6.5 km west-northwest of Custer City, OK, from 0205-0213 UTC, and an EF0 (referred to as tornado #2 herein) that traveled from 13 km northwest to 11 km northwest of Custer City from 0216-0217 UTC (Fig. 4.7). The vortex signature associated with the first tornado (TVS1) exceeded the threshold ($\Delta v_{max} \geq$

Figure 4.7: Video still taken by the author at 0216 UTC 16 June 2019 of tornado #2 (background; pink arrow) and the remnant mesocyclone associated with tornado #1 (foreground; white arrow).

40 m s^{-1}) established by Alexander (2010) from the time that data collection began; however, it did not meet the vortex diameter criterion ($\Delta r \leq 2$ km) until about 0205 UTC. Also, RaXPol was at a range of approximately 20 km or greater from TVS1 (and the vortex signature associated with tornado #2, TVS2) for the entirety of D1 and D2. As a result, the 0° elevation angle corresponded to heights of 40-60 m ARL, whereas in the Amber-Bridge Creek case, for example, the 0° elevation angle corresponded to heights generally 6-9 m ARL[1]. Therefore, near-surface TVS intensity was likely about 25% less than TVS intensity observed at the lowest elevation angle of RaXPol data (Wurman et al. 2007). Also, sporadic data loss within TVS1 at the 0-2° elevation angles during D1 may have resulted in some degree of error in recorded Δv_{max} values. It is possible that tornado

[1] These values are accurate for the theoretical beam centerline; however, the actual mean power height of the radar beam was likely higher than the theoretical height due to ground effects (Snyder et al. 2015).

#1 may have been ongoing before damage surveys indicated, but this cannot be assessed with certainty given these issues. In addition, an increase in Δv_{max} of about 18 m s^{-1} at 0.4 km ARL (2°) occurred between 0205:00 and 0206:12 UTC, suggesting that RaXPol may have captured tornadogenesis during D1. Due to the approaching forward-flank precipitation region of the supercell, RaXPol repositioned as tornado #1 evolved; however, in the first 2-3 min of D2, RaXPol documented a decrease in Δv_{max} of 13 m s^{-1}. Thus, the decay of tornado #1 appears to have been captured, as well. RaXPol also appears to have collected data during the brief life cycle of tornado #2, including genesis and decay.

4.3.1 Evolution of the TVSs with Height and Time

Figs. 4.8-4.10 feature scatterplots[2] that illustrate the progression of Δv_{max}, Δr, and ζ_{pseudo} during the life cycle of each TVS. Δv_{max} within TVS1 first increased from 70-75 m s^{-1} to 80-85 m s^{-1} in the 6-8 km ARL layer at 0204:02 UTC (Fig. 4.8a). This was coincident with the beginning of vortex constriction, particularly at low-levels, where it decreased in width from a relative maximum of 4.04 km at 400 m ARL at 0203:24 UTC (Fig. 4.8b). However, low-level Δv_{max} remained fairly steady. Subsequently, the region of increased Δv_{max} aloft built downward to approximately 4 km ARL by 0205:08 UTC, after which both low-level Δv_{max} and ζ_{pseudo} began increasing rapidly (Fig. 4.8a, c). TVS1 first met the Δr threshold between 0204:36 and 0205:00 UTC and continued to constrict even

[2] In this case, scatter plots more clearly conveyed changes in Δv_{max}, Δr, and ζ_{pseudo} with time than contour plots did; therefore, they were used in lieu of contour plots.

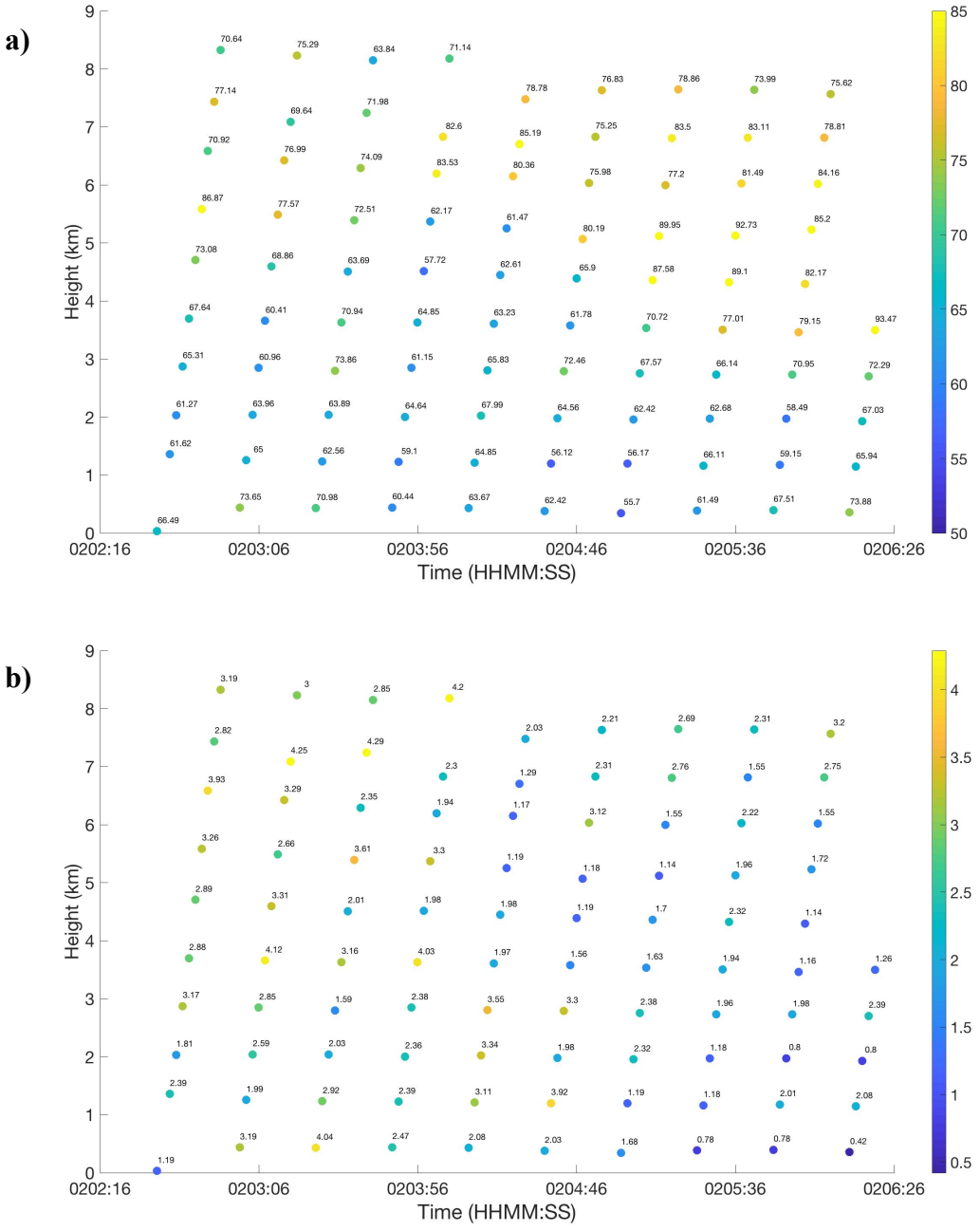

Figure 4.8: Scatterplots for TVS1 of a) Δv_{max} (in m s^{-1}), b) Δr (in km), and c) ζ_{pseudo} (in s^{-1}; next page) as a function of time versus height during D1.

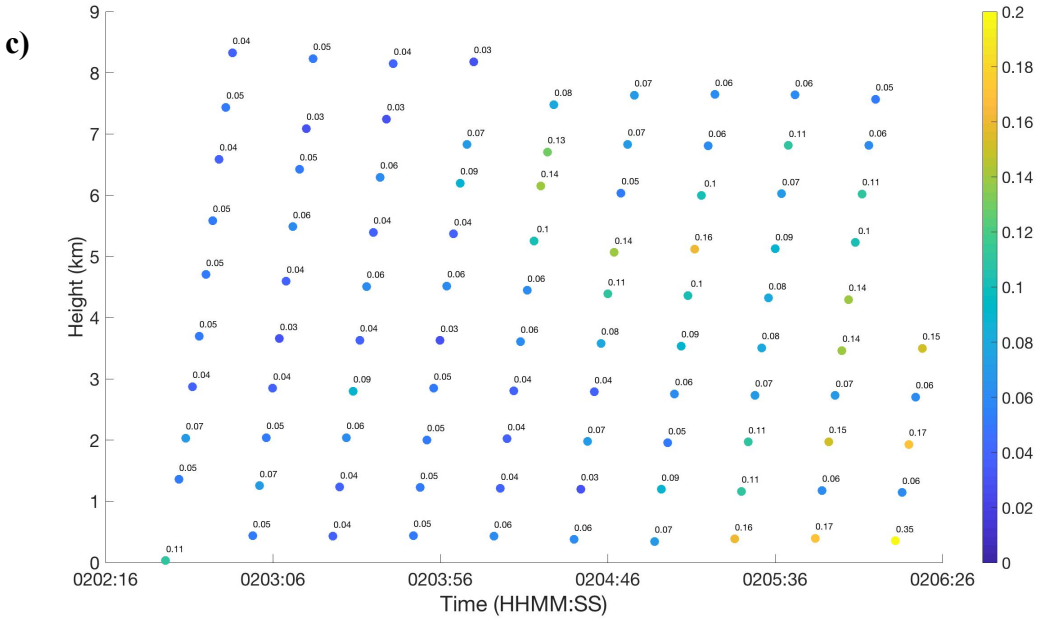

Figure 4.8 (continued).

further to 420 m wide at 0.4 km ARL at 0206:10 UTC (Fig. 4.8b). Therefore, tornado #1 may have begun slightly earlier than damage surveys indicated (0206 UTC), and it appears that tornadogenesis associated with TVS1 first began aloft and built downward with time, in contrast to the findings of French et al. (2013), Bluestein et al. (2019), and others. As discussed in Chapter 1, Trapp and Davies-Jones (1997) determined that a tornadic vortex that builds downward from aloft via DPE occurs when buoyancy is confined to the midlevels. Despite an increase in 0-3 km convective available potential energy (CAPE), a measure of positive buoyancy in the lowest 3 km of the atmosphere and a proxy for low-level vortex stretching potential (Rasmussen 2003), surface-based convective inhibition also increased as the evening progressed (not shown). However, the environment sampled by the 0000 UTC 16 June sounding from Norman, OK (Fig. 4.2), was extremely unstable, especially in the midlevels, which likely helped storm updrafts

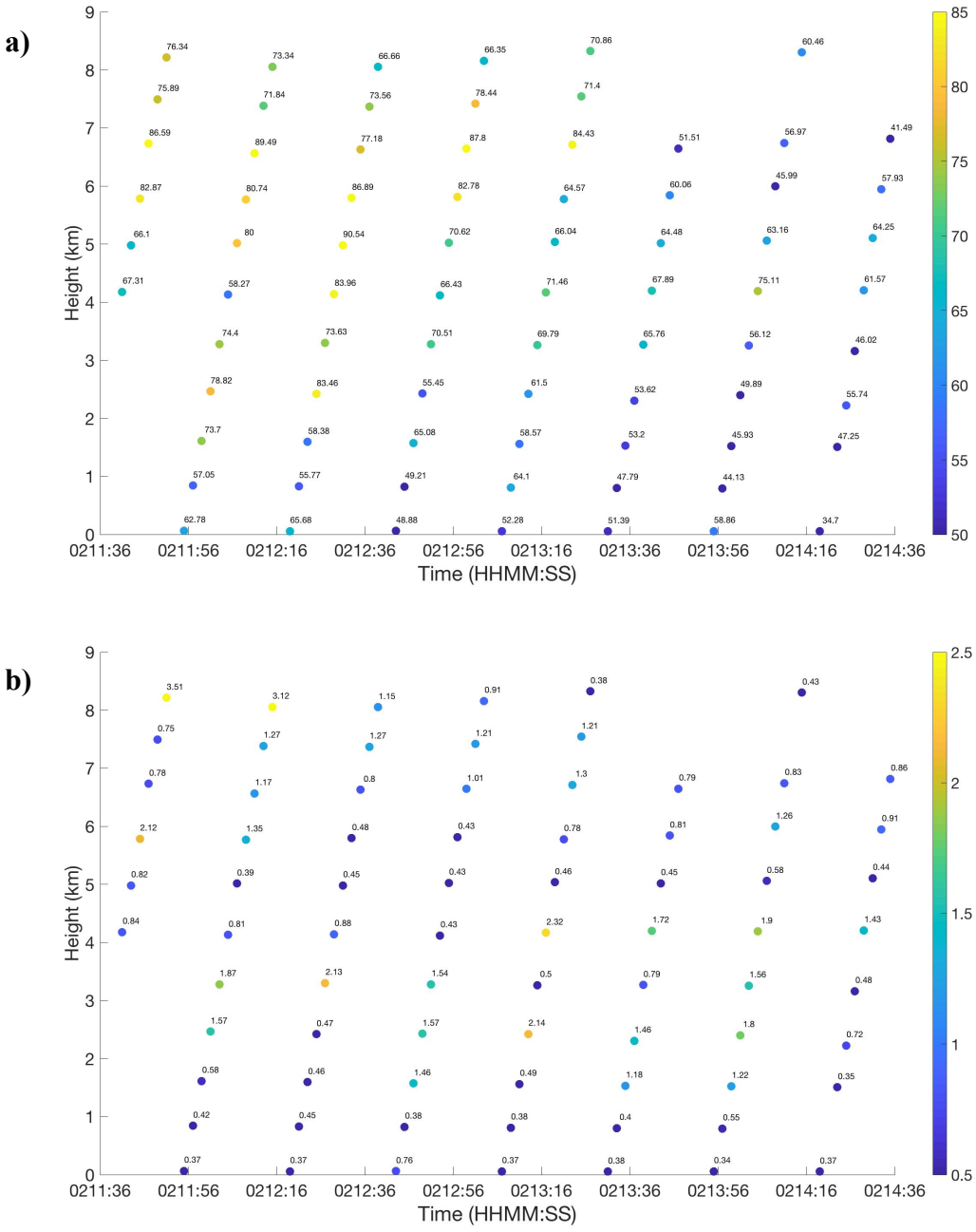

Figure 4.9: As in Fig. 4.8, but for the portion of TVS1 in D2.

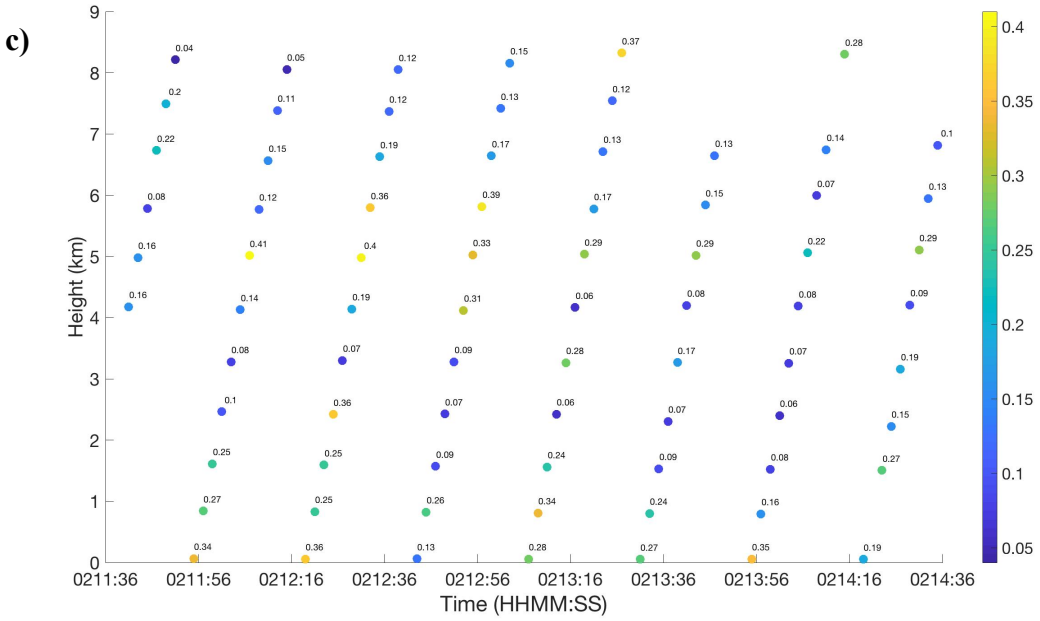

Figure 4.9 (continued).

overcome the increasing convective inhibition and fostered DPE-induced, descending tornadogenesis.

As in the Amber-Bridge Creek case, TVS1 appears to have decayed in an "inside-out" manner, as in French et al. (2014) and Houser et al. (2015). As seen in Fig. 4.9a, the vortex first weakens between 2.5 and 5 km ARL by approximately 0212:50 UTC, then simultaneously from 1-2.5 km ARL and above 5 km ARL[3], and then finally at the lowest elevation (50 m ARL) between 0213:55 and 0214:19 UTC. TVS1 maintained both tornadic intensity and size until 0214:19 UTC, at which point Δv_{max} was 34.7 m s^{-1} despite Δr of 370 m and ζ_{pseudo} of 0.19 s^{-1}. Also, a tornado debris signature (TDS) was evident in correlation coefficient data until 0215:30 UTC; this will be discussed further in section 4.3.3. Therefore, it is possible that tornado #1 may have persisted for a greater

[3] The missing data above 7 km ARL between 0213:36 and 0214:36 in Fig. 4.9 is a result of TVS1 becoming ambiguous at these levels.

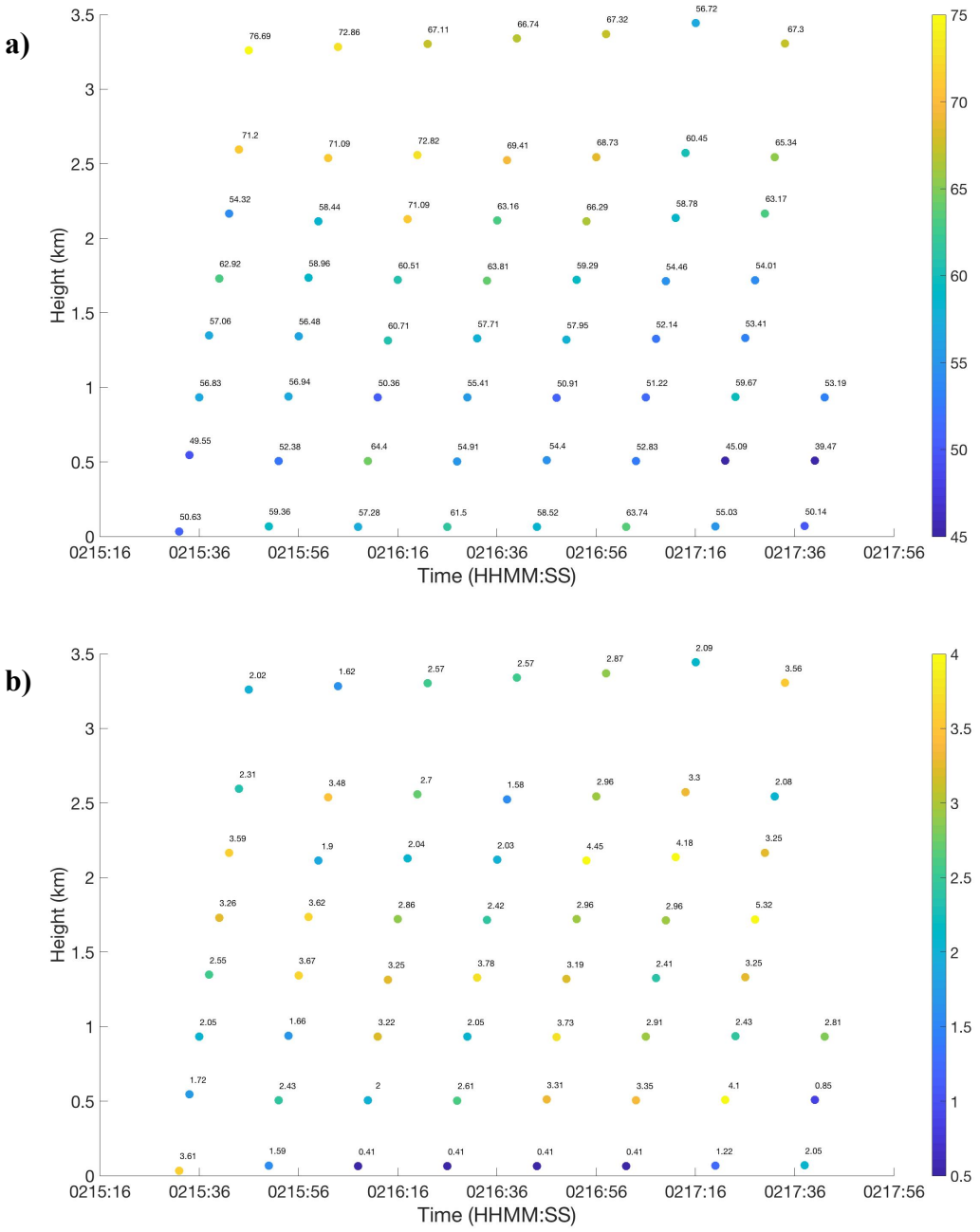

Figure 4.10: As in Fig. 4.8, but for TVS2.

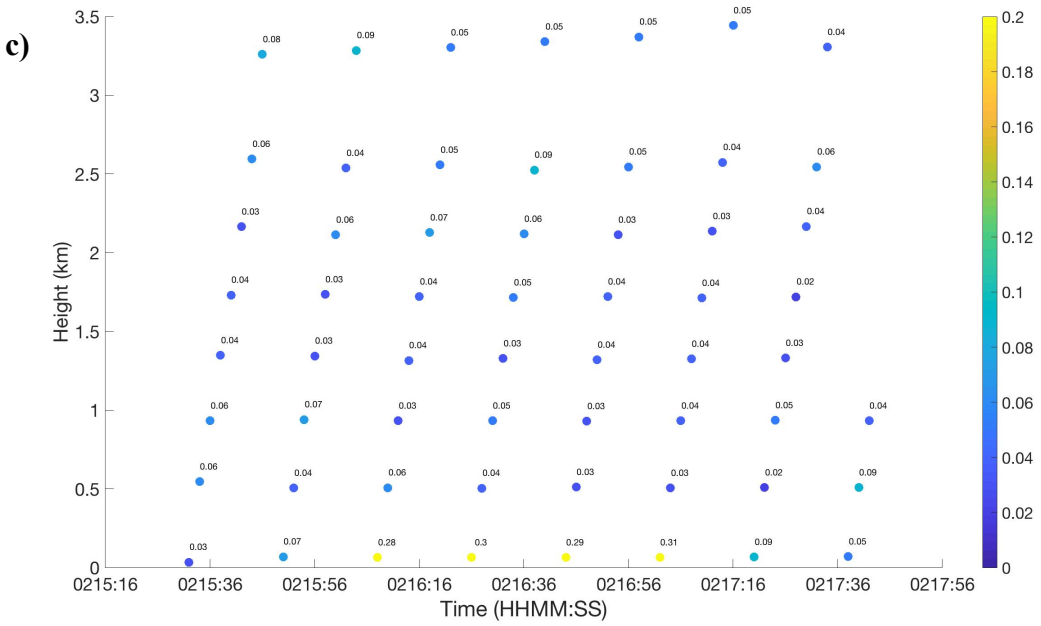

Figure 4.10 (continued).

period of time than damage surveys indicated. TVS1 was also wider at midlevels than it was at upper or low-levels (Fig. 4.9b), signifying somewhat of a pear-shaped vortex. This was documented by Bluestein et al. (2004) in a tornado near Happy, TX, on 5 May 2002, although the bulge in the vortex and associated WEH was apparent at about 100 m ARL.

TVS2 was characterized by a narrow near-surface vortex that widened considerably just above in the lowest 0.5 km ARL. This was apparent both in Fig. 4.10b and visually (Fig. 4.7), as video of the tornado reveals a condensation funnel that narrows significantly as it approaches the surface. It is unclear whether TVS2 built upward or downward with time during tornadogenesis; however, trends in the low-level vortex can be discerned from the data. The vortex first intensifies rapidly at low-levels from 0215:32-0216:08 UTC; over this period, Δv_{max} increases from 50 to 59 m s^{-1}, Δr decreases from 3.61 to 0.41 km, and ζ_{pseudo} increases from 0.03 to 0.28 s^{-1}. Thus, it appears that the

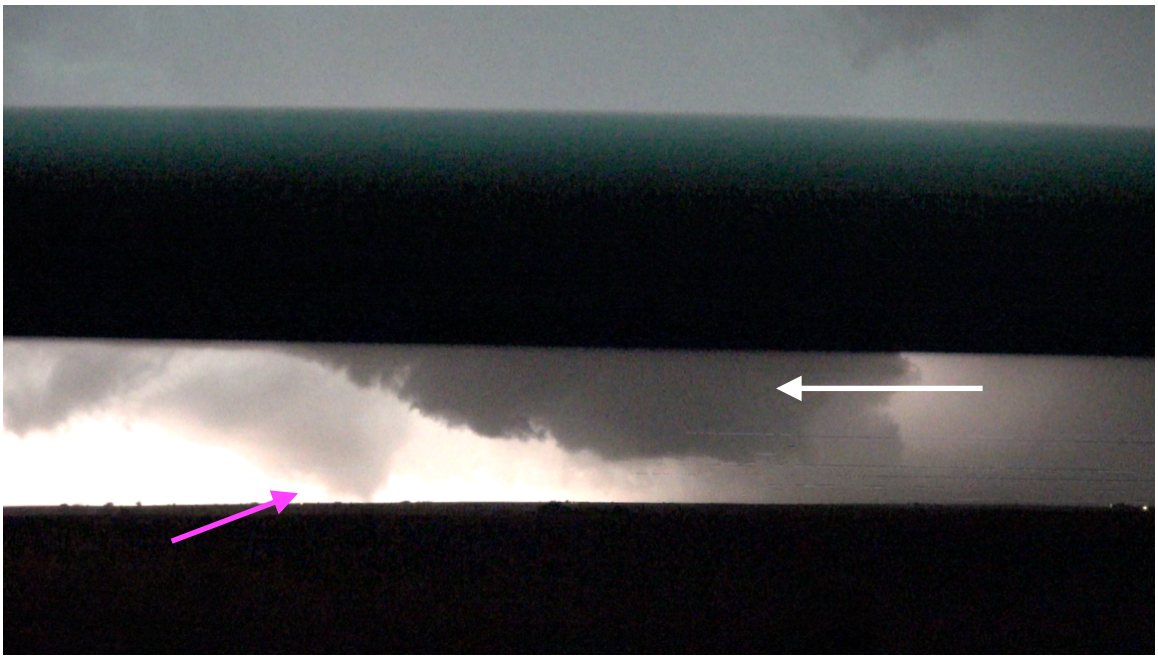

Figure 4.11: Video still taken by the author at 0218 UTC 16 June 2019 of tornado #2 (background; pink arrow) and the remnant mesocyclone associated with tornado #1 (foreground; white arrow). The white bar at the top of the image is an artifact of the desynchronization of the camera's shutter speed with the frequency of the lightning.

tornado was in progress slightly before 0216 UTC, as damage surveys indicated. After 0217:02 UTC, the low-level vortex weakens, as both Δv_{max} and ζ_{pseudo} decrease and Δr increases. At 0217:38 UTC, TVS2 no longer met the Alexander (2010) criteria (Δr had increased to 2.05 km); however, video evidence suggests that the tornado persisted through at least 0218:00 UTC (Fig. 4.11).

The Putnam supercell appeared to undergo non-occluding cyclic mesocyclogenesis (NOCM) as described by Adlerman and Droegemeier (2005). NOCM involves the repeated generation of low-level mesocyclones that do not occlude as they dissipate. Instead, "near-ground mesocyclones move down the gust front, and away from the main updraft, rather than wrapping back into the precipitation core. They then become separated from the main updraft and a new mesocyclone forms farther northward, near

a)

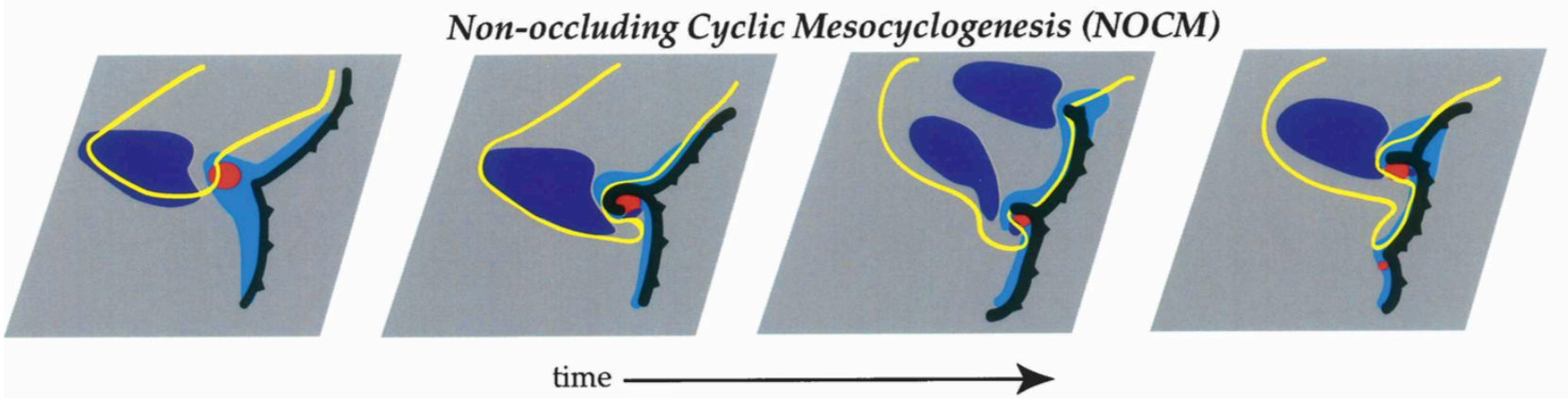

b)

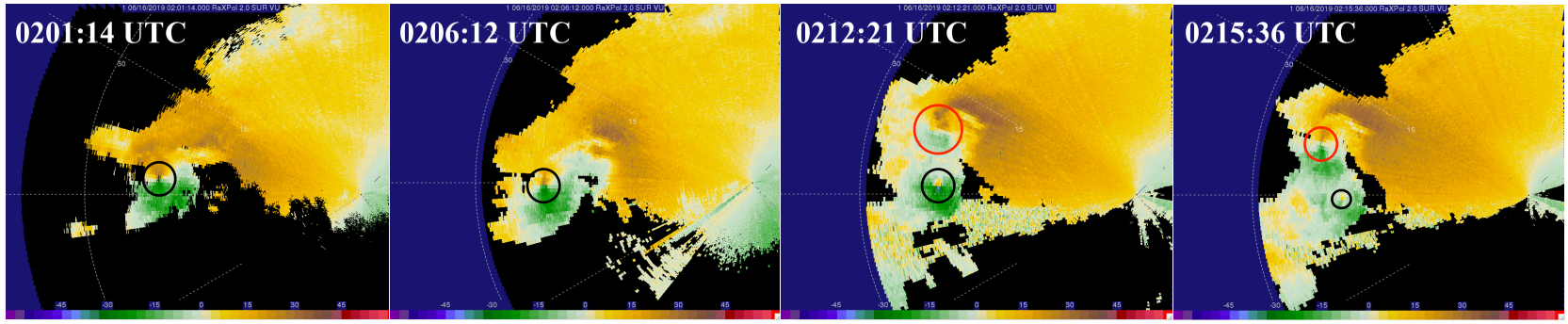

Figure 4.12: a) Schematic diagram of non-occluding cyclic mesocyclogenesis adapted from Adlerman and Droegemeier (2005), and b) a progression of mesocyclogenesis using radial velocity imagery, including (from left to right) 0201:14, 0206:12, 0212:21, and 0215:36 UTC. The black circle denotes the location of the TVS1, and the red circle denotes the location of TVS2.

the forward-flank precipitation boundary." This process is illustrated in Fig. 4.12a. As TVS1 dissipated, it traveled southward, away from the main updraft; subsequently, the mesocyclone to the north began to intensify, and tornado #2 occurred (Fig. 4.12b).

Adlerman and Droegemeier (2005) note that caution should be used when applying this theory directly to observed supercells because the wind shear profiles used in their study are idealized; however, it gives a viable baseline for examining the behavior of mesocyclones in observed supercells. In addition, the lack of data between 0206:20 and 0211:31 UTC while RaXPol was repositioning is problematic when diagnosing the mesocyclogenetic behavior of the Putnam supercell, as the mesocyclone associated with TVS2 initially developed during this time period. Still, the behavior of the TVSs in the Putnam supercell most closely matches the NOCM model, especially given the meager hodograph curvature and overall weak ambient wind shear, which, according to Adlerman and Droegemeier (2005), increases the probability of NOCM in simulated supercells.

4.3.2 Vortex Tilt with Height

In the period leading up to the genesis of tornado #1, TVS1 underwent a significant change in its orientation. At 0203:24 UTC, TVS1 was tilted toward the northwest with height at an angle of approximately 40° from due north (Fig. 4.13a). By 0203:48 UTC, tilt was highly variable but generally due north (Fig. 4.13b), except in the uppermost portion of the vortex (6-8 km ARL). Subsequently, TVS1 began to tilt significantly toward the northeast, acquiring about 55° of tilt by 0204:12 UTC. This

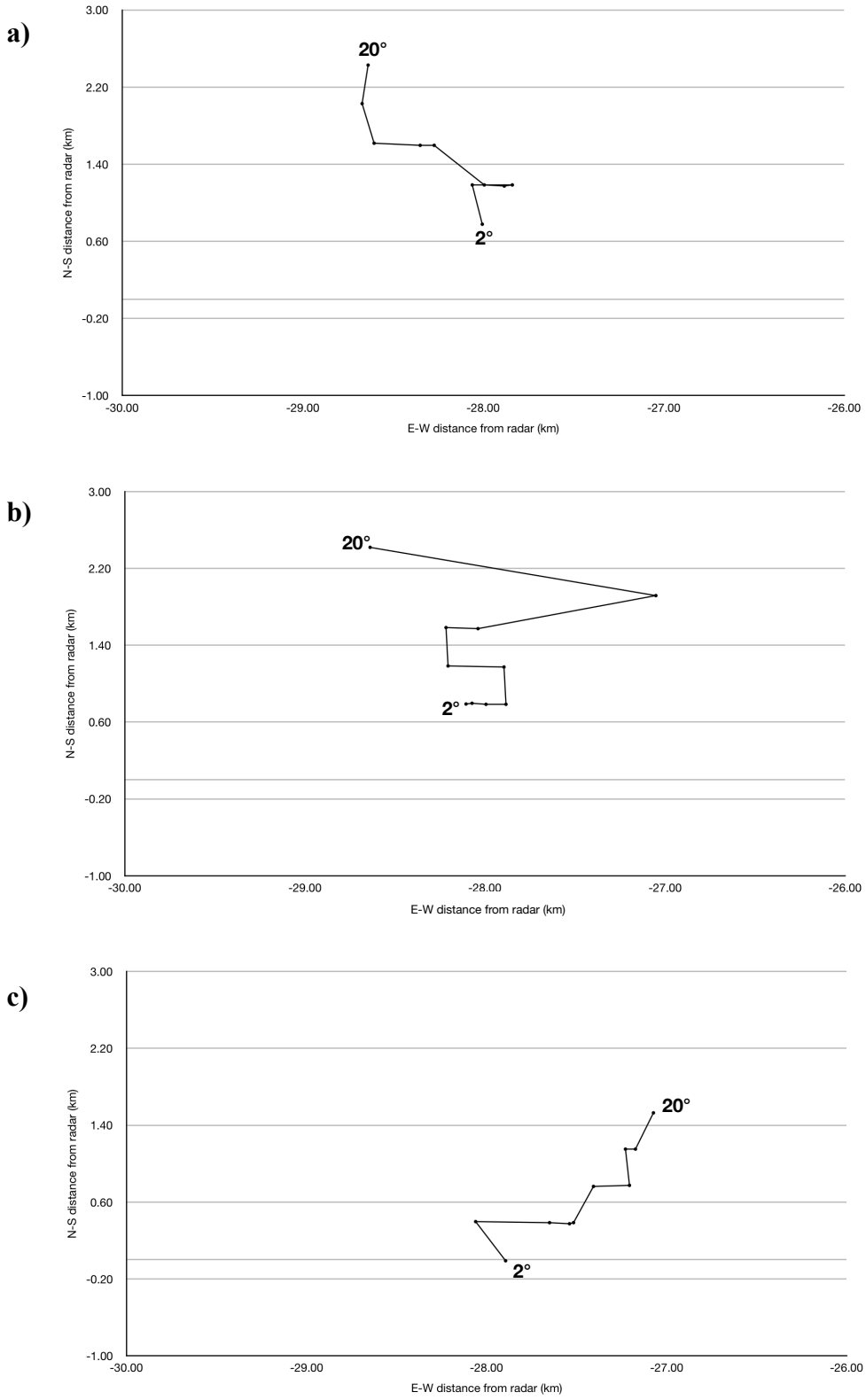

Figure 4.13: Graph of vortex tilt with height for TVS1 at a) 0203:24 UTC, b) 0203:48 UTC, c) 0205:00 UTC, and d) 0212:19 UTC.

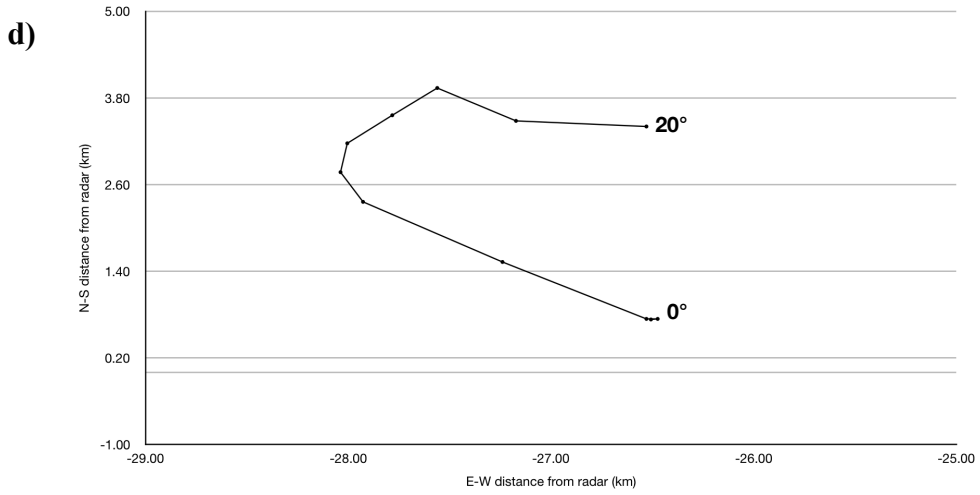

Figure 4.13 (continued).

remained the case until tornadogenesis at 0206 UTC (Fig. 4.13c). From the beginning of D2 through tornado decay, the vortex had regained its northwest tilt (approximately 65° from due north) with height up to 5 km ARL, above which it tilted toward the east-northeast or east (Fig. 4.13d). Similar oscillations in tilt during a tornado's life span were documented by Lee and Wurman (2005) in the 3 May 1999 Mulhall, OK, tornado, which varied between northwesterly and vertical tilting modes. However, unlike in the Amber-Bridge Creek case (Chapter 3), TVS1's northwesterly tilt mirrored neither the northeasterly 0-6 km environmental wind shear vector (not shown) as described in Griffin et al. (2019) nor the RAP model proximity hodograph from Watonga, OK, at 0200 UTC (Fig. 4.15). The Putnam supercell occurred in an environment of weak vertical wind shear; as a result, the vortex was likely not as sculpted by wind shear as other, higher-shear cases (e.g. the Amber-Bridge Creek case) and was, therefore, more chaotic in its vertical structure and affected more by transient near-storm and in-storm kinematics. In addition, the weak-shear environment may have enhanced outflow production in the

Putnam supercell, which may have displaced the low-level vortex from the mid- and upper-level vortex.

On the other hand, TVS2 was less chaotic in its tilt with height than TVS1. Between 0215:32 (immediately preceding tornadogenesis) and 0217:20 UTC (decay), the vortex generally displayed northeasterly tilt with height of 45-65° from due north (Fig. 4.14). This supports the findings of French et al. (2014) and Griffin et al. (2019), among others. Throughout the duration of TVS2, the vortex at 60 m ARL (0°) was located to the east of the vortex at 500 m ARL (1°), and a kink in the vortex in which a sharp bend to the east was followed by a bend back to the west or northwest was apparent from 1.5-2.5 km ARL. In general, TVS2 followed the 0200 UTC RAP proximity hodograph (Fig. 4.15) more closely than TVS1 did, at least up to approximately 3 km ARL, which is how high RaXPol scanned during D2. Thus, this vortex was likely less impacted by storm features, such as outflow or the RFGF, than the vortex associated with TVS1.

4.3.3 Selected Radar Signatures

4.3.3.1 Weak-echo Column

A WEC was coincident with TVS1, the first evidence of which occurred at 0158:54 UTC from 1.7-2.5 km ARL. Although the aforementioned sporadic data loss within TVS1 at the 0-2° elevation angles introduced some difficulty in assessing the existence of low-level WEHs during D1, the WEC appeared to gradually build downward to about 0.8 km ARL by 0201:14 UTC. After the scan strategy was changed at 0202:34 UTC, the WEC, or at least some form of a bounded weak-echo region (BWER), was

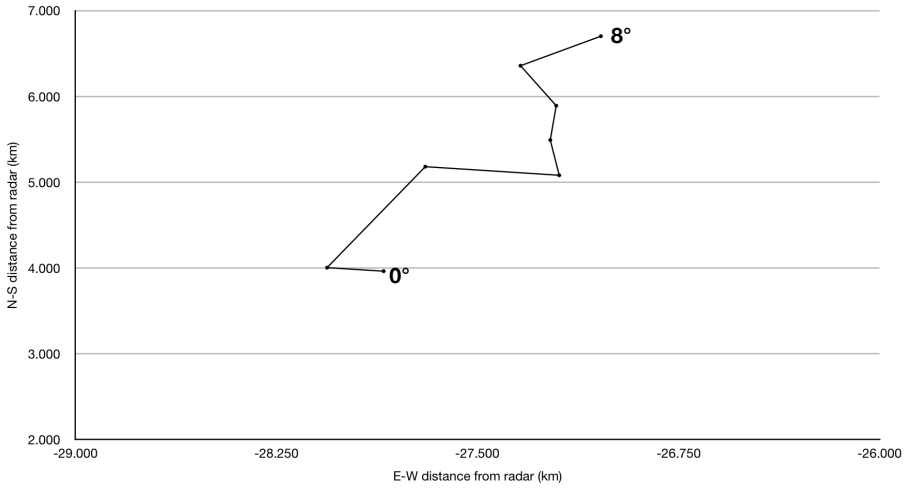

Figure 4.14: As in Fig. 4.12, but for TVS2 at 0216:08 UTC.

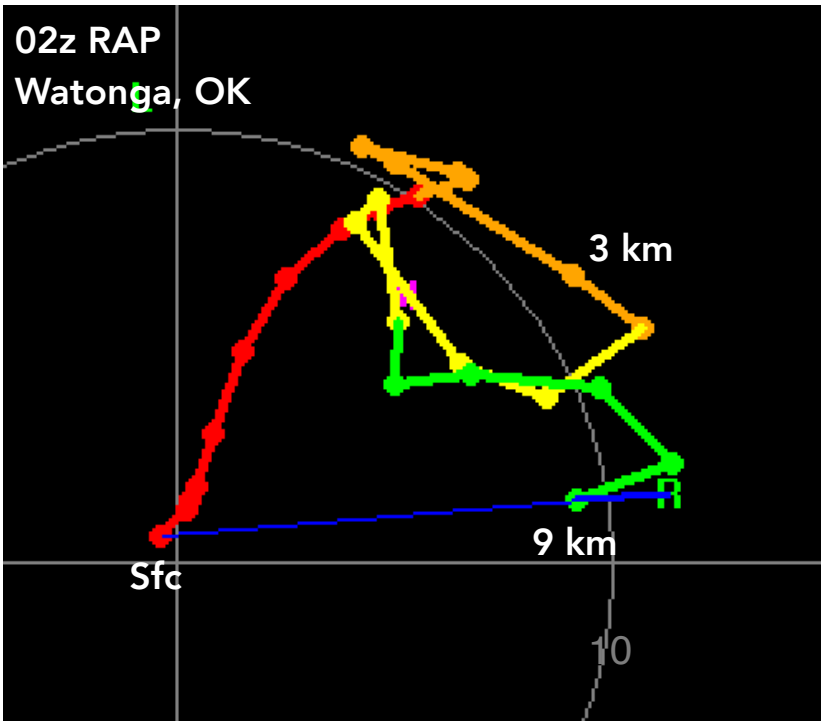

Figure 4.15: RAP proximity hodograph from Watonga, OK, valid at 0200 UTC 16 June 2019.

evident through the entire depth of each volume above 0.8 km ARL through the remainder of D1. By the beginning of D2, the WEC had reached the lowest elevation angle (60 m ARL) and continued to appear through the depth of the data (Fig. 4.16), although it was sometimes difficult to discern or not completely bounded by higher reflectivity. The WEC first began to decay above 7 km ARL at 0212:13 UTC, then from 2.3-3.3 km at 0213:13 UTC, and was no longer apparent at any height by 0214:19 UTC. A WEC was not evident with TVS2.

4.3.3.2 Tornado Debris Signature

Tornado #1 appeared to loft debris, as a well-defined TDS coincident with TVS1 was evident in ρ_{HV} data (Fig. 4.17b). Given the dearth of structures along its path, the TDS was likely composed of grass and tree debris. It was apparent from 0211:55-0215:30 UTC only at about 60 m ARL (0°) and was generally less than 1 km in width based on the criterion ($\rho_{HV} < 0.80$) employed in previous TDS studies using X-band radar[4] (e.g. Houser et al. 2016; Wienhoff et al. 2020). Until 0212:43 UTC, lowered Z_{DR} accompanied the lowered ρ_{HV} (Fig. 4.17c), which is a well-known feature of TDSs (Ryzhkov et al. 2005, Kumjian and Ryzhkov 2008). After this point, however, Z_{DR} increased, and no evidence of a TDS was apparent in the Z_{DR} data. This could be the result of precipitation mixing with the debris in the TDS, which is discussed by Kumjian and Ryzhkov (2008). In addition, the TDS was evident well after TVS1 dissipated due to debris fallout from the remnant circulation. Tornado #2 did not produce a TDS, likely because the tornado

[4] Bodine et al. (2014) determined the same criterion but for S-band radar.

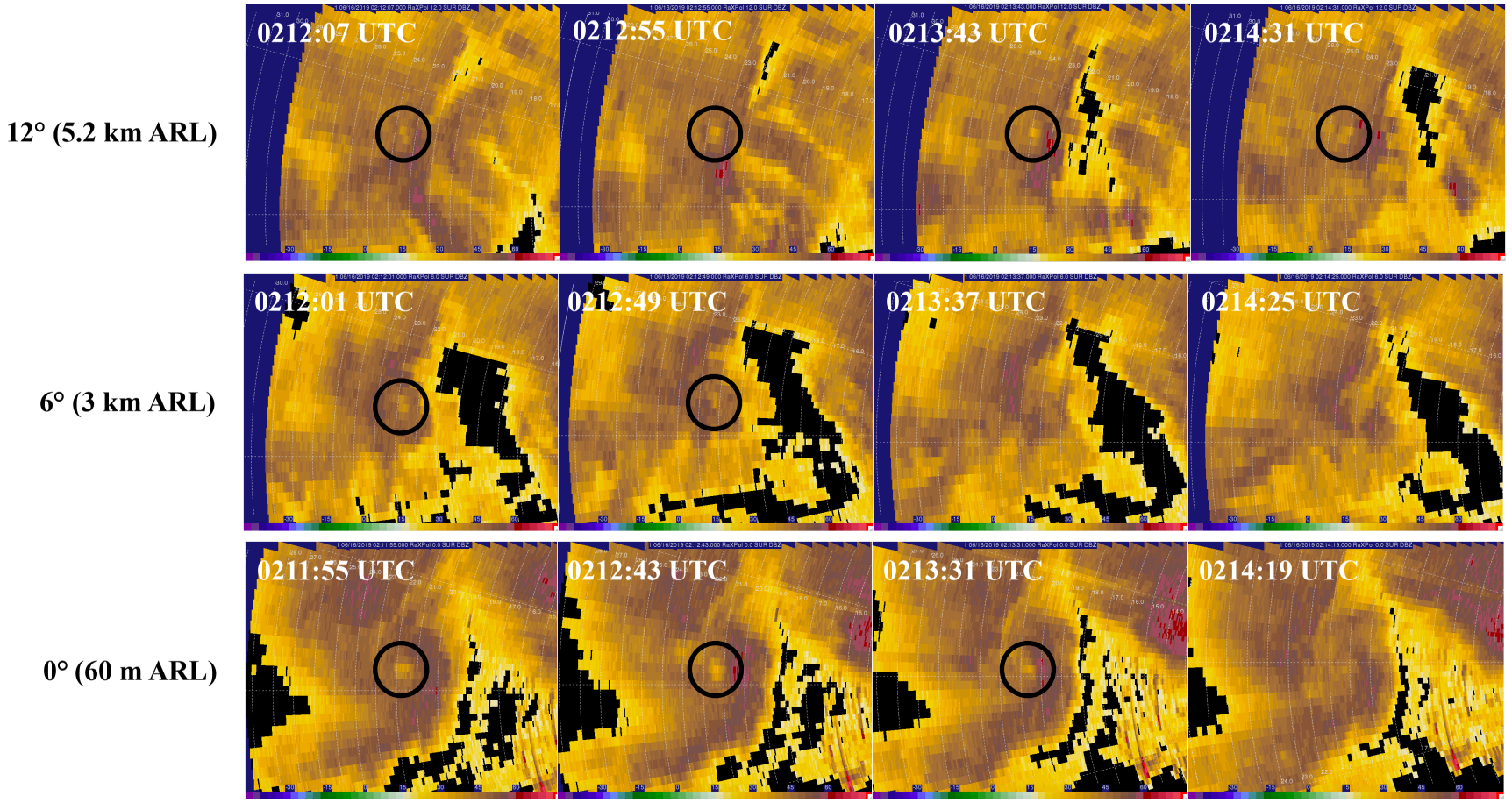

Figure 4.16: Sequence of reflectivity images (from bottom to top) at 0° (60 km ARL), 6° (3 km ARL), and 12° (5.2 km ARL) showing the evolution of the WEH (denoted by the black circles) during D2.

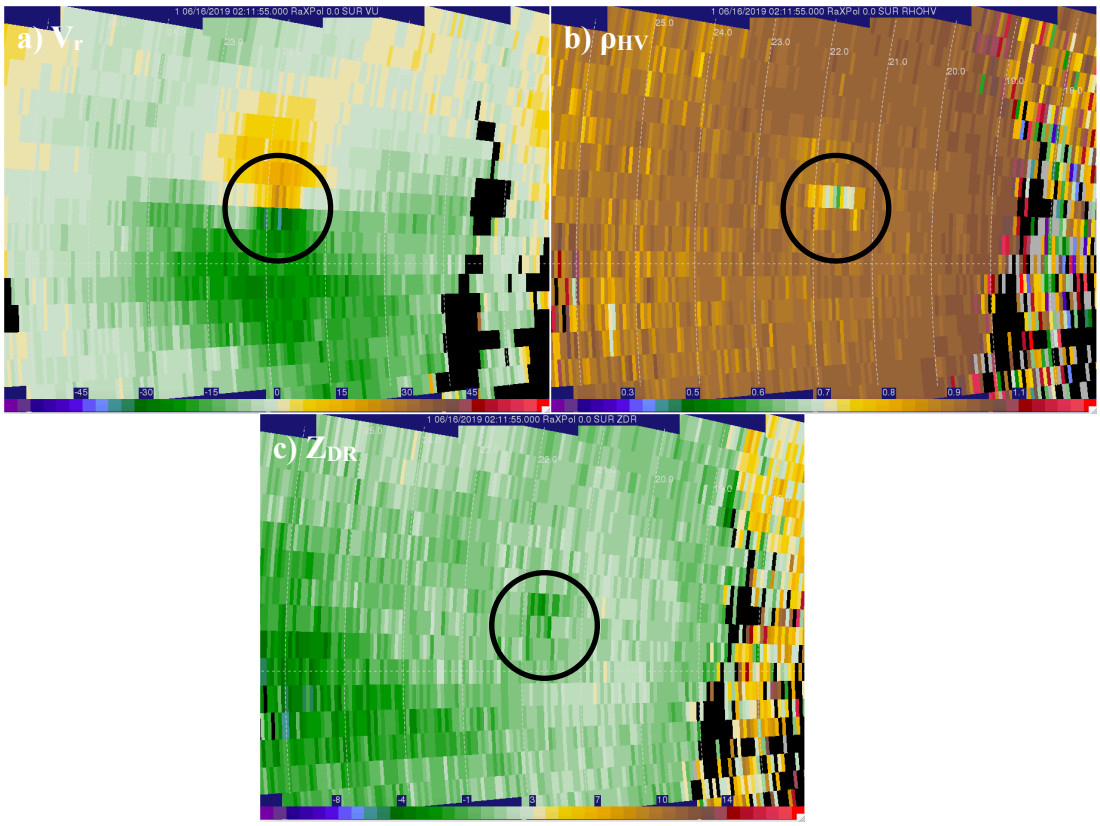

Figure 4.17: a) Radial velocity (m s^{-1}), b) ρ_{HV} (dimensionless), and c) Z_{DR} (dB) images at 0° in elevation of the TDS associated with TVS1 at 0211:55 UTC. Range rings are included at 1-km increments.

was relatively weak and, thus, debris was not lofted high enough to be detected by RaXPol.

4.4 Secondary Vortices

A small, anticyclonic vortex was apparent approximately 9 km northeast of TVS1 at the beginning of D2 (Fig. 4.18). It lasted until 0216:26 UTC, was generally only evident up to 1 km ARL, and failed to satisfy the criteria for a TVS throughout its life cycle. Similar anticyclonic vortices have been documented in previous studies (e.g. Fujita 1981, Bluestein et al. 2007) and in the Amber-Bridge Creek case discussed in this study;

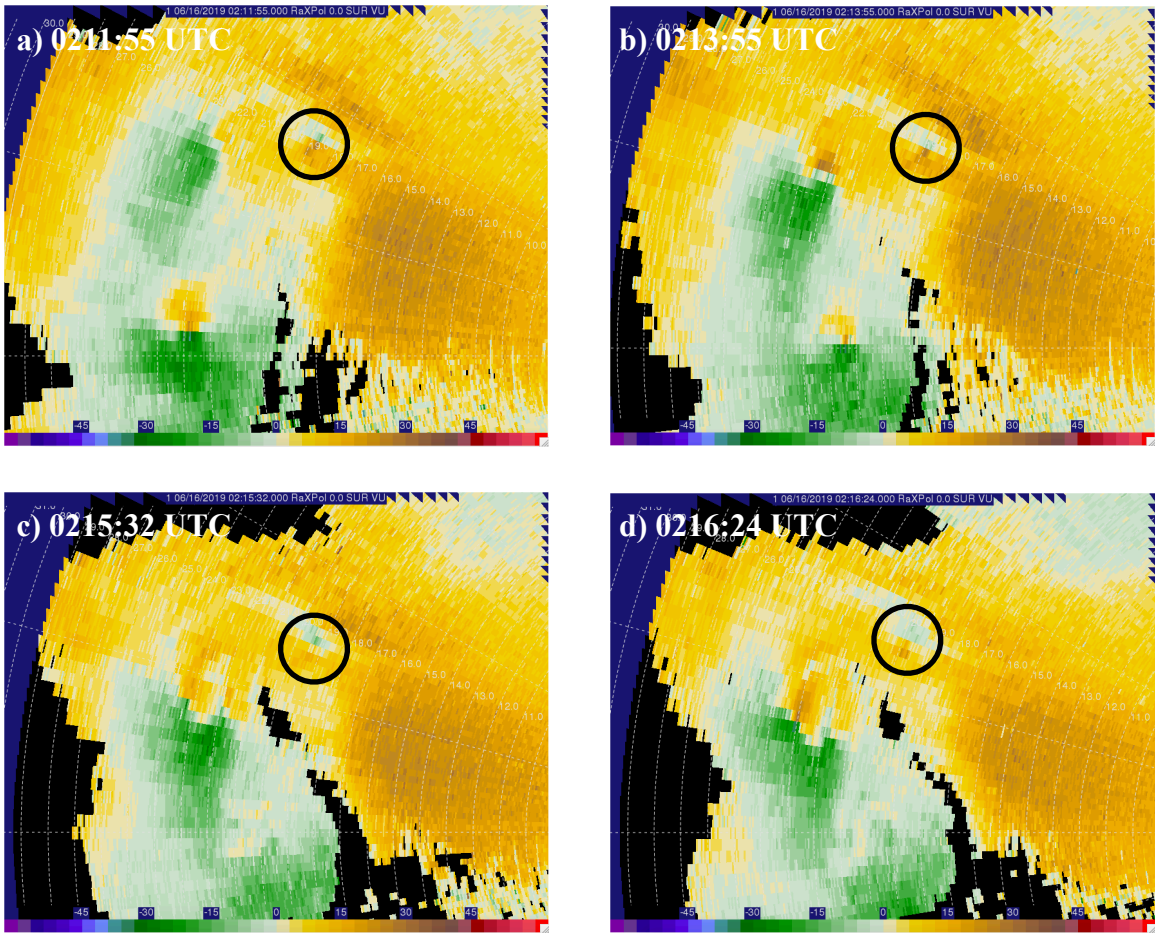

Figure 4.18: Radial velocity (m s^{-1}) at 0° in elevation at a) 0211:55, b) 0213:55, c) 0215:32, and d) 0216:24 UTC depicting the evolution of the anticyclonic vortex (black circle). Range rings are included at 1-km increments.

however, these vortices were all associated with an RFD gust front or in the vicinity of the main (cyclonic) hook echo of a supercell. In the case of the Putnam storm, the anticyclonic vortex was located near the interface between the inflow notch and the forward-flank precipitation region. Closer inspection suggests that the vortex occurred at the intersection of the leading gust front and a roughly northwest-to-southeast-oriented shear zone (Fig. 4.19). The vortex formed, potentially, as a roll-up of vorticity on the anticyclonic side of the shear zone and propagated slowly southward or south-southwestward (not shown), along with the shear zone but away from the leading gust

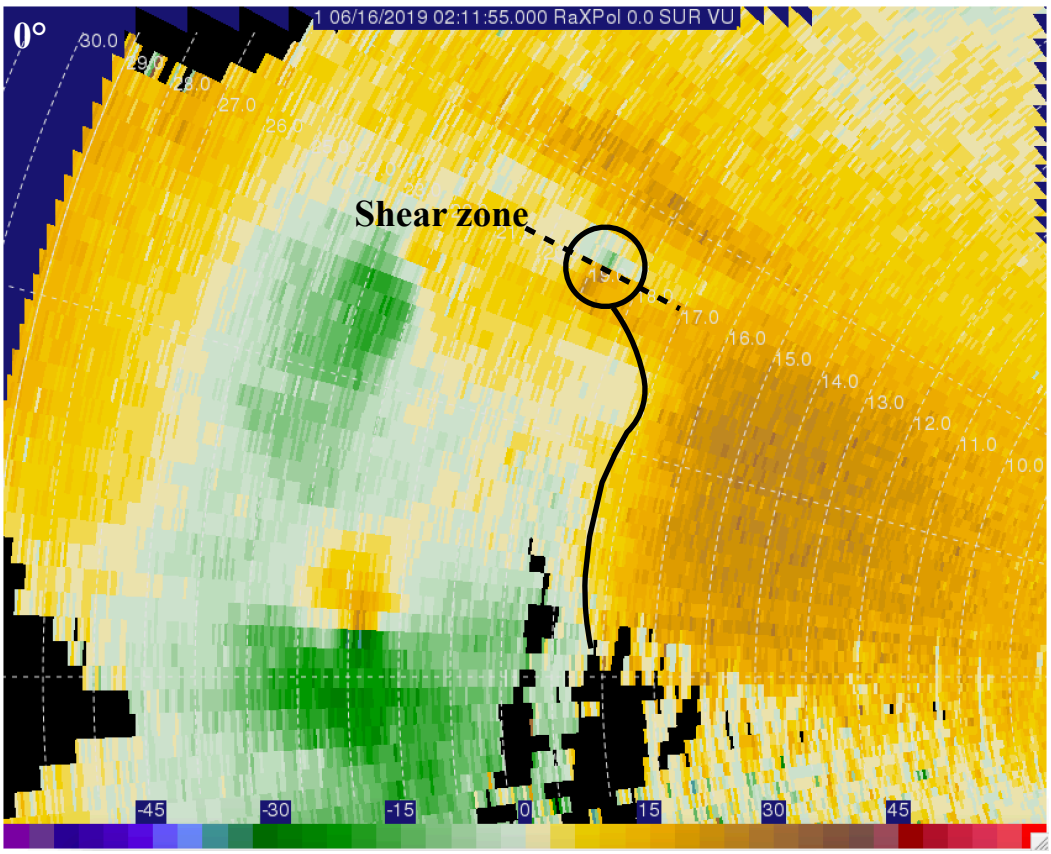

Figure 4.19: Zoomed-in view of radial velocity (m s^{-1}) at 0° in elevation at 0211:55 UTC. The leading gust front is denoted by the solid black line, and the shear zone is demarcated by the dashed black line. The anticyclonic vortex is denoted by the black circle.

front. Snyder et al. (2020) examined an ostensible anticyclonic vortex similarly located in the forward flank of a tornadic supercell near Sulphur, OK, on 9 May 2016. That study determined that it was likely a quasi-horizontal vortex centered approximately 1-1.5 km AGL, rather than an anticyclonic tornado as determined in damage surveys. Also, the anticyclonic vortex could be associated with the developing cyclonic circulation to its west that would become tornado #2, forming a cyclonic-anticyclonic vortex pair at the end of the leading gust front, similar to those described in Bluestein et al. (2016).

In addition, a separate, cyclonic vortex became evident from 0212:43-0214:19 UTC approximately 7 km due north of TVS1 (Fig. 4.20). From 0212:43-0213:55 UTC, it

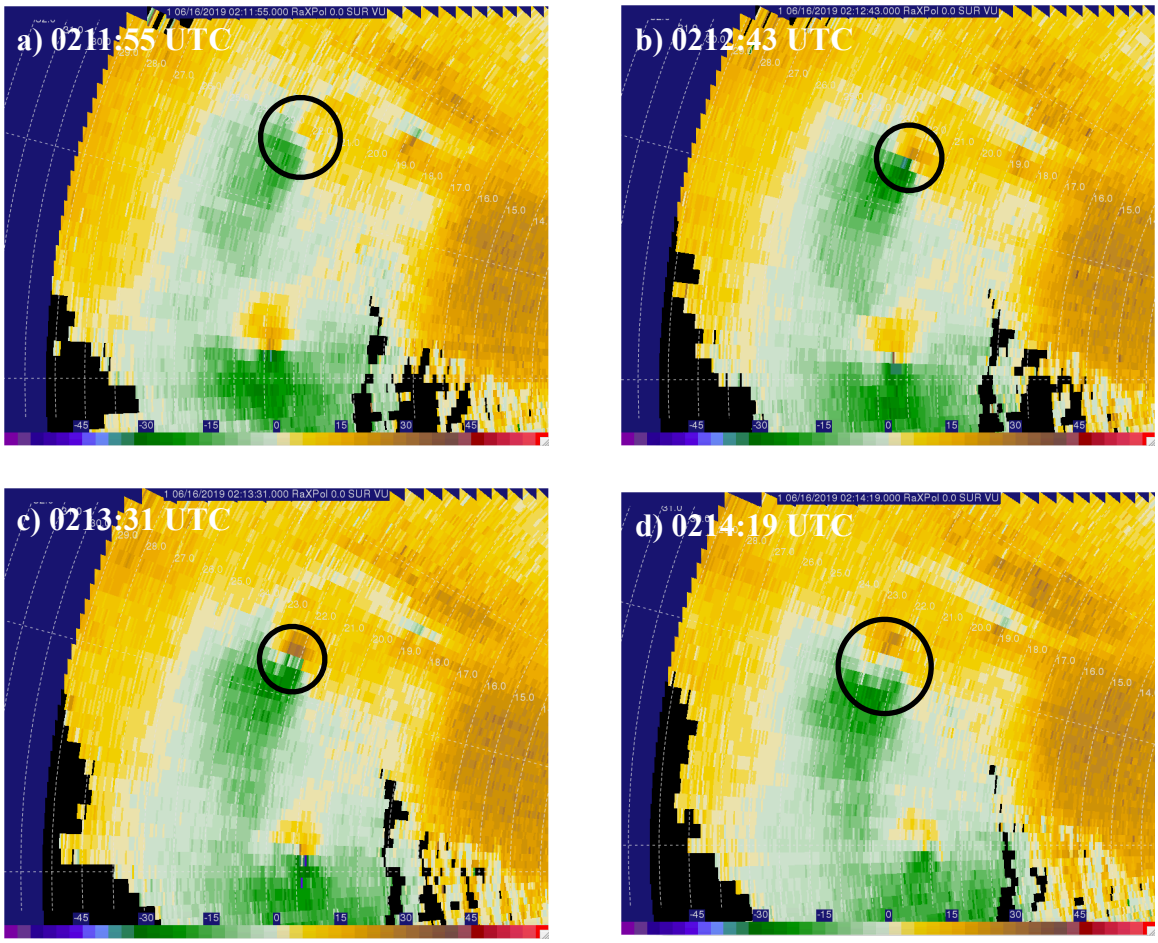

Figure 4.20: Radial velocity (m s^{-1}) at 0° in elevation at a) 0211:55, b) 0212:43, c) 0213:31, and d) 0214:19 UTC. The black circle denotes the location of the near-surface cyclonic vortex.

significantly exceeded the Alexander (2010) thresholds for a tornadic vortex with Δv_{max} between 55-70 m s^{-1} and Δr between 0.40-1.60 km. By 0214:19 UTC, the vortex had broadened to over 2 km in width; however, Δv_{max} remained well above the 40 m s^{-1} criterion. This vortex was colocated with the mesocyclone associated with TVS2; however, it was quite shallow, only evident at the 0° elevation angle (60 m ARL). Thus, it is possible that this vortex could have been a tornado or perhaps some sort of low-level vortex akin to a gustnado, although it was much stronger than most gustnadoes and it was not located along the leading edge of convective outflow (Grazulis 2001).

Chapter 5

The Elmer-Tipton, OK, Tornado: 16 May 2015

5.1 Synoptic Overview

On 16 May 2015, a large, progressive, 500-mb trough was centered over the northern Rockies with a well-defined speed maximum ejecting into southwest Oklahoma by 2200 UTC (Fig. 5.1a). A resultant lee trough was evident at 850 mb with cyclones located over northeast Wyoming and southeast Colorado (Fig. 5.1b). As illustrated in the 0000 UTC 17 May hodograph from Norman, OK, in Figure 5.3b, southeasterly surface winds and southerly 850-mb winds in excess of 15 m s^{-1} beneath southwesterly 500-mb winds yielded strong deep-layer (greater than 30 m s^{-1}) and low-level shear (ESRH greater than 400 m^2 s^{-2}) supportive of long-lived supercells with strong tornadoes.

Throughout the morning and early afternoon, an area of showers and thunderstorms impacted a large expanse from southern Nebraska to northwest Oklahoma, effectively stabilizing the atmosphere and substantially decreasing the afternoon severe weather threat in this region (Fig. 5.2). However, farther south along an eastward-moving Pacific cold front/dryline, northwest Texas and southwest Oklahoma were relatively undisturbed save for an area of high clouds, which began to erode by early afternoon. The

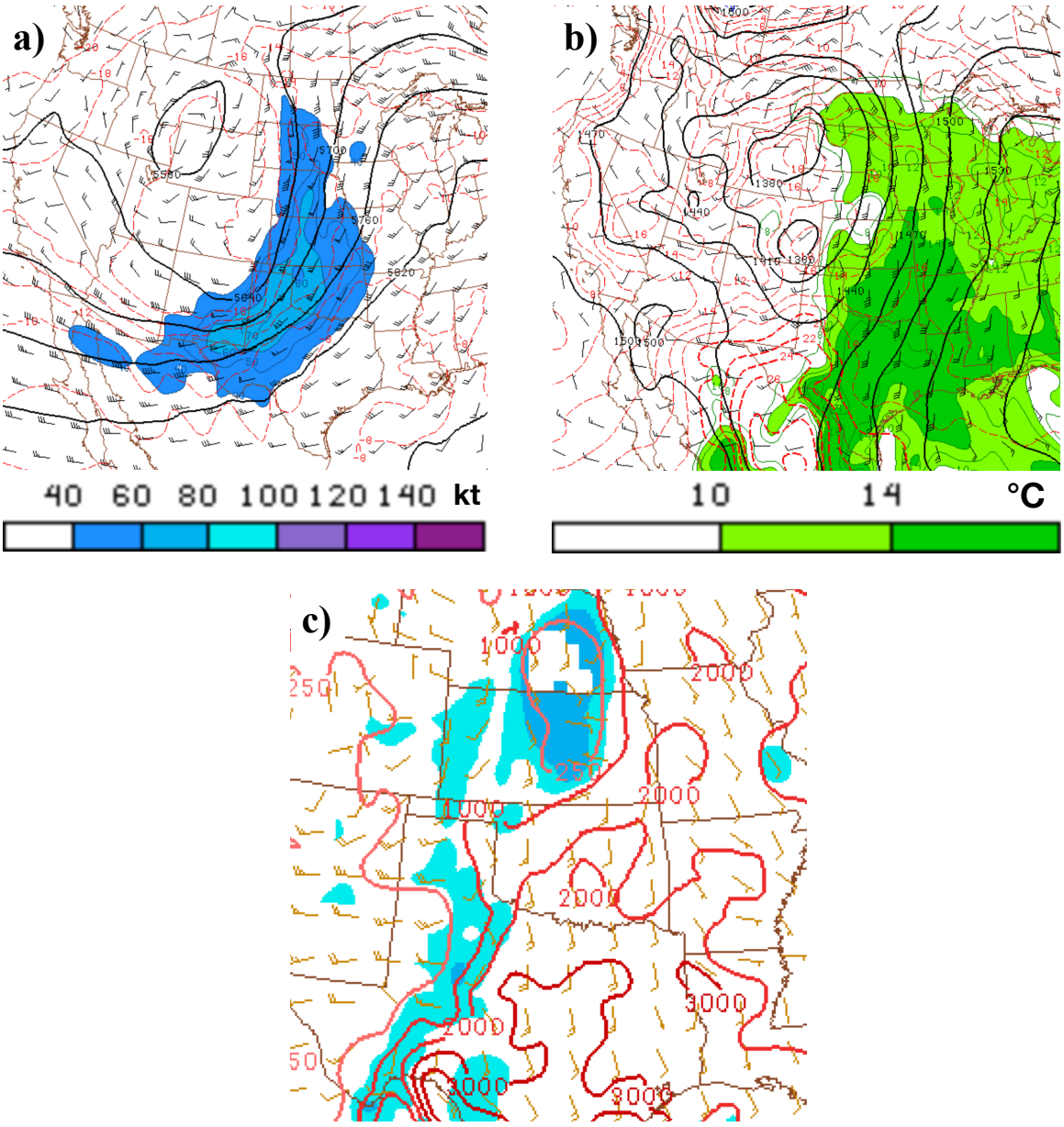

Figure 5.1: Overview of the synoptic environment on 16 May 2015. Pictured above are a) 500 mb winds, b) 850 mb winds and moisture, and c) MLCAPE and MLCIN, all valid at 2200 UTC. Adapted from the Storm Prediction Center Mesoanalysis Archive.

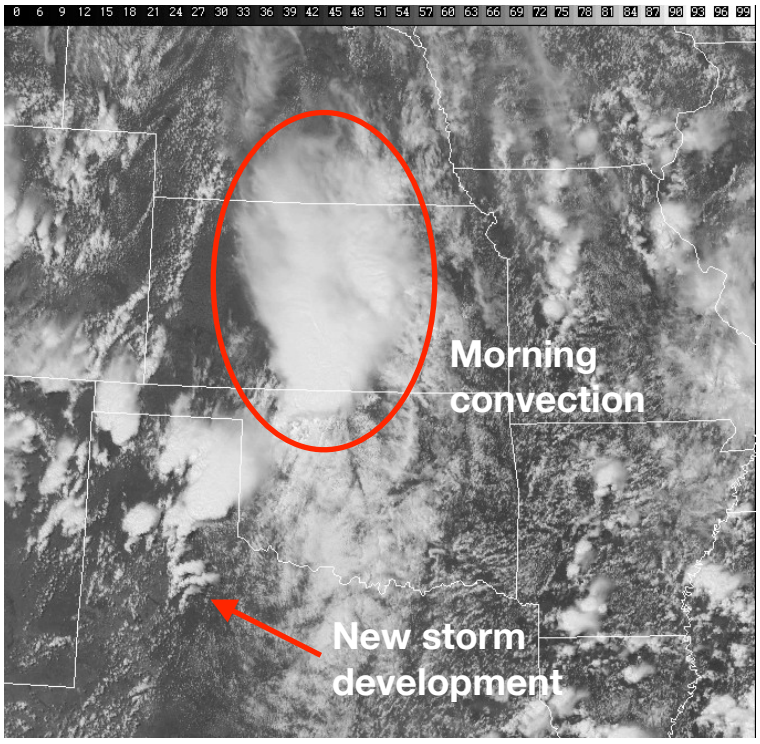

Figure 5.2: Visible satellite image taken at 1915 UTC. The morning storm complex and the area of new storm development along the dryline are demarcated.

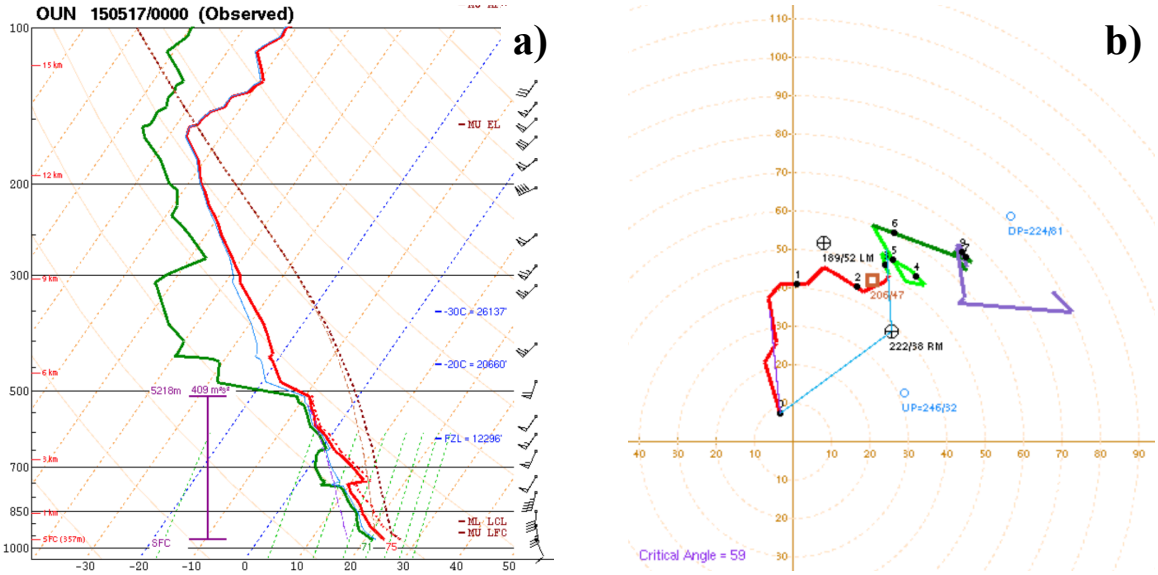

Figure 5.3: KOUN (Norman, OK) a) sounding and b) hodograph, valid at 0000 UTC 17 May 2015. Taken from the Storm Prediction Center Severe Weather Events Archive.

subsequent surface heating, along with a deep moist layer up to approximately 750 mb (Fig. 5.3a), generated MLCAPE values in excess of 2000 J kg^{-1} (Fig. 5.1c). MLCIN in excess of 150 J kg^{-1} sampled on the 1800 UTC sounding at Norman (not shown) suppressed convective initiation until midday, when storms began to develop in northwest Texas along the dryline (Fig. 5.2).

5.2 Supercell Formation and Evolution

Isolated storms were ongoing by 1700 UTC in the southern Texas Panhandle, and coverage increased in this area over the next hour. These storms traveled to the northeast and produced several tornadoes in the eastern Texas Panhandle and western Oklahoma between 1800 and 2200 UTC. Well to the south of this activity, showers developed at 1800 UTC and gradually strengthened; by 2000 UTC, a broken line of semi-discrete storms, including some supercells, extended from near McLean, TX, southward to near Matador, TX (Fig. 5.4a). A storm near the southern end of the line rapidly intensified between 2000 and 2040 UTC, at which point it attained the classic "kidney bean" shape exhibited by many supercells (Doswell 1998) as mid-level rotation increased (Fig. 5.4b). By 2115 UTC, the supercell developed a broad hook echo that became more well-defined over the next hour as low-level rotation increased (Fig. 5.4c, d).

5.3 The Elmer-Tipton Tornado

According to NWS Norman damage surveys (NWS Norman 2015), the Elmer-Tipton tornado began approximately 13 km north of Chillicothe, TX, at 2226 UTC and

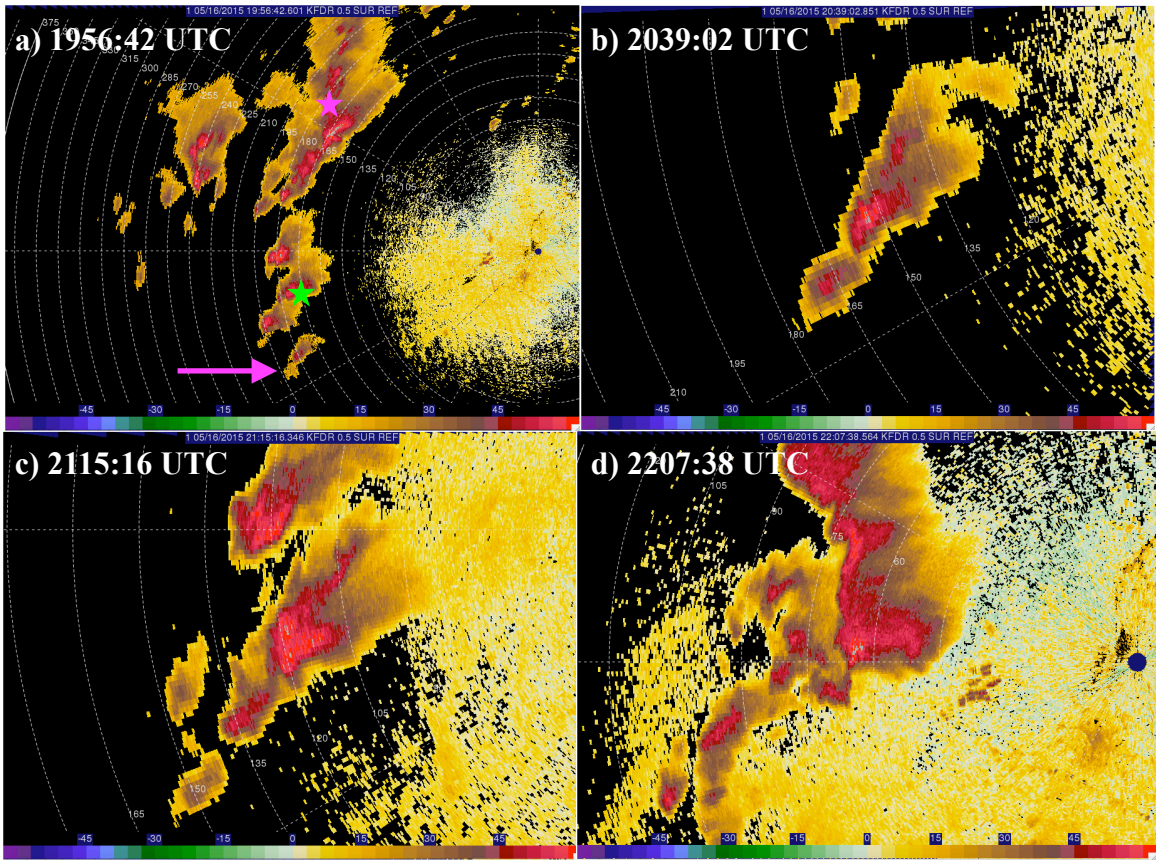

Figure 5.4: Evolution of the supercell that produced the Elmer-Tipton tornado using 0.5° reflectivity (dBZ) data from the KFDR radar. Included are a) the initial broken line of storms at 1956:42 UTC (the shower that would become Elmer-Tipton supercell is denoted by the pink arrow, and McLean and Matador, TX, are denoted by the pink and green stars, respectively), b) the Elmer-Tipton supercell as it attained a "kidney bean" shape at 2039:02 UTC, c) the Elmer-Tipton supercell as it developed a broad hook echo at 2115:16 UTC, and d) the supercell at 2207:38 UTC, several minutes before it produced the Elmer-Tipton tornado. Each panel follows the storm as it moves; therefore, the area displayed in each panel is different.

dissipated at 2345 UTC approximately 5 km east of Snyder, OK (Fig. 5.5), producing EF3 damage. Both RaXPol and the MWR-05XP collected data from the Elmer-Tipton tornado; however, this study will focus on the MWR-05XP data, unless noted otherwise, because the vertical continuity within each volume allows for analysis without correcting for storm motion. RaXPol data will be used to supplement MWR-05XP data when polarimetric variables reveal significant characteristics of the supercell or tornado. The

Figure 5.5: Damage path of the Elmer-Tipton tornado, denoted by the orange outline, identified from damage surveys. The location of the MWR-05XP during deployment has been labeled. Adapted from NWS Norman (2015).

Figure 5.6: Photograph of the Elmer-Tipton tornado taken at 2228 UTC approximately 21 km southwest of Tipton, OK. Courtesy of Stephen Jones.

MWR-05XP was deployed once in far northern Wilbarger County, TX, using three different scanning strategies: up to 28.6° from 2219:42-2228:17 UTC, up to 20° from 2229:53-2237:40 UTC, and up to 55° from 2238:16-2241:02 UTC. For simplicity, each deployment interval will be referred to as Deployment 1 (D1), Deployment 2 (D2), and Deployment 3 (D3), respectively, and data above 20° will be ignored to streamline data throughout the deployment. However, data up to approximately 7 km will be analyzed.

5.3.1 Evolution of the TVS with Height and Time

Fig. 5.7[1] features plots of Δv_{max}, Δr, and ζ_{pseudo}, as a function of height versus time for the latter half of D1 (2224:50-2228:17 UTC) and the entirety of D2. A low-level, pre-tornadic circulation first became discernible at 2224:50 UTC and, at 0° (0.4 km ARL), initially satisfied the Δv_{max} threshold at 2225:59 UTC (Fig. 5.8), which correlates well with the time of tornadogenesis determined by damage surveys. Through the end of D1, a steady increase in near-surface Δv_{max} occurred, followed by a gradual, nearly linear increase in Δv_{max} up to approximately 2 km ARL by the end of D1, and Δr, which remained generally near or above the 2 km threshold prior to 2227:00 UTC, rapidly decreased near the surface from 2.20 km at 2226:51 UTC to 0.32 km at 2227:08 UTC. A similar, abrupt decrease in Δr occurred simultaneously at all levels up to approximately 2.5 km ARL. Despite this, the TVS remained quite broad above 3.5 km ARL for several minutes after tornadogenesis, particularly in the 4.5-5 km ARL layer, in which Δr was as

[1] Similar plots were compiled in an analysis of the Elmer-Tipton tornado by Frost et al. (2018); however, those in Fig. 5.7 were created by the author.

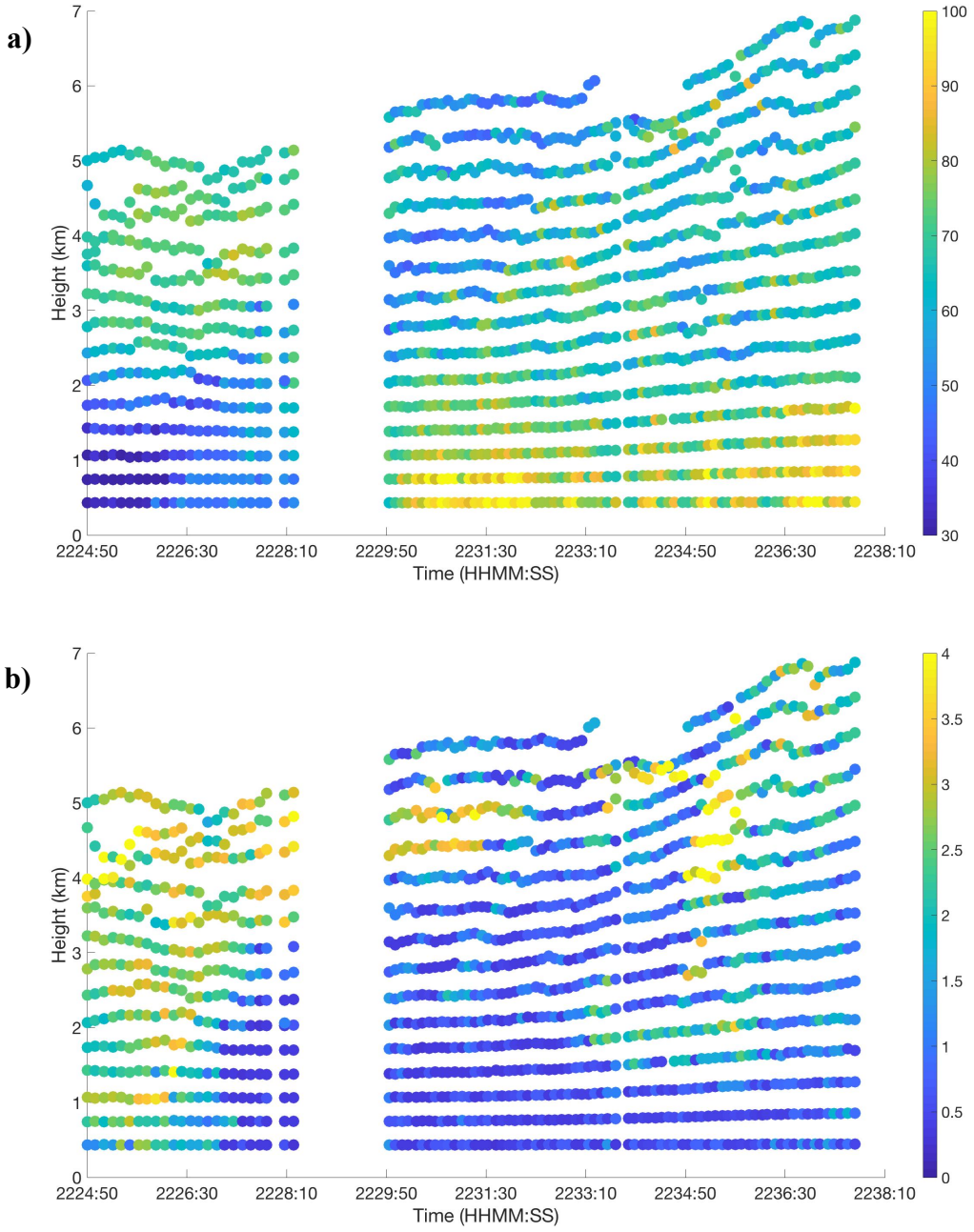

Figure 5.7: Scatterplots of a) Δv_{max} (in m s^{-1}), b) vortex diameter (in km), and c) ζ_{pseudo} (in s^{-1}) as a function of time versus height for D1 and D2.

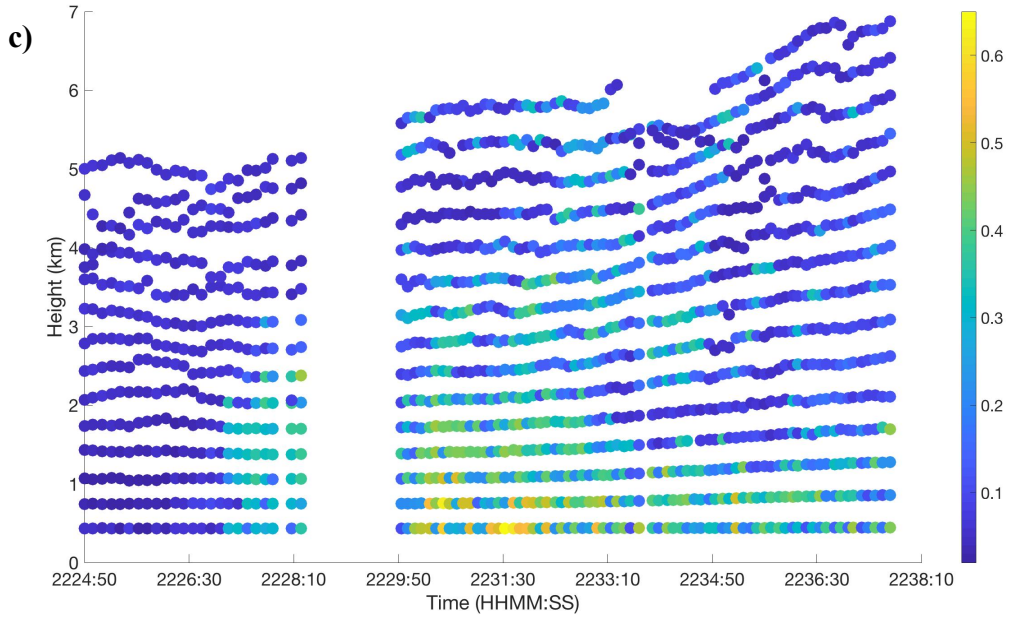

Figure 5.7 (continued).

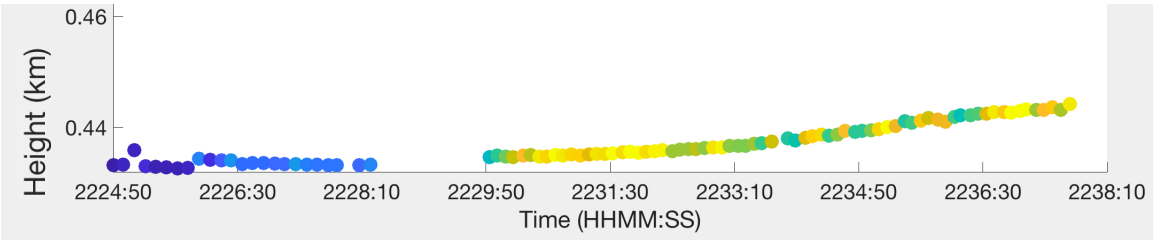

Figure 5.8: As in Fig. 5.7a, but for only the 0° elevation angle. The scale in Fig. 5.7a applies here.

great as 4.30 km at 2231:19 UTC. By 2232:12 UTC, the Δr threshold was satisfied throughout the entire vortex. Therefore, as in French et al. (2013) and Bluestein et al. (2019), the vortex appears to have begun first near the ground and built upward with time.

The initial intensification of the low-level TVS occurred in two distinct phases, the first of which coincides with tornadogenesis as described above. The second was a sudden, significant increase in near-surface Δv_{max} that began around 2230 UTC, about

three minutes after the abrupt contraction of the vortex. During this phase, Δv_{max} at 0° (0.4 km ARL) increased from 63.77 m s^{-1} at 2229:53 UTC to 95.83 m s^{-1} at 2230:33 UTC, eventually reaching a peak of 110.14 m s^{-1} at 2231:32 UTC. This two-phased intensification is a mirror image of the biphasic dissipation of the 9 May 2016 Sulphur, OK, tornado, which first rapidly dissipated over a five-minute period and then more gradually over a twelve-minute stretch (McKeown et al. 2020). Following the period of rapid intensification of the Elmer-Tipton tornado, near-surface Δv_{max} generally plateaued, save for periodic surges in vortex intensity (to be discussed further in section 5.3.3).

In addition, at all levels above 2 km ARL, Δv_{max} greatly exceeded the 40 m s^{-1} threshold through the end of D1. However, by the beginning of D2, Δv_{max} above 3 km ARL had decreased by 5-25 m s^{-1}, which continued through the aforementioned period of sudden near-surface vortex intensification before gradually increasing in the vertical until about 2233 UTC. This suggests that the vortex aloft weakened immediately preceding the second burst of low-level vortex intensification. Also, Δr at 2 km ARL increased between approximately 2233 and 2236 UTC, coincident with a sudden, significant increase in Δr from 4-5 km ARL between 2235 and 2236 UTC. However, Δv_{max} did not decrease appreciably throughout this period.

5.3.2 Vortex Tilt with Height

Unlike the Amber-Bridge Creek tornado, the Elmer-Tipton tornado was not highly tilted throughout D1 and D2; the vertical structure of the vortex was fairly chaotic (Fig. 5.9). At 2224:50 UTC, when the first evidence of a near-surface TVS appeared, the

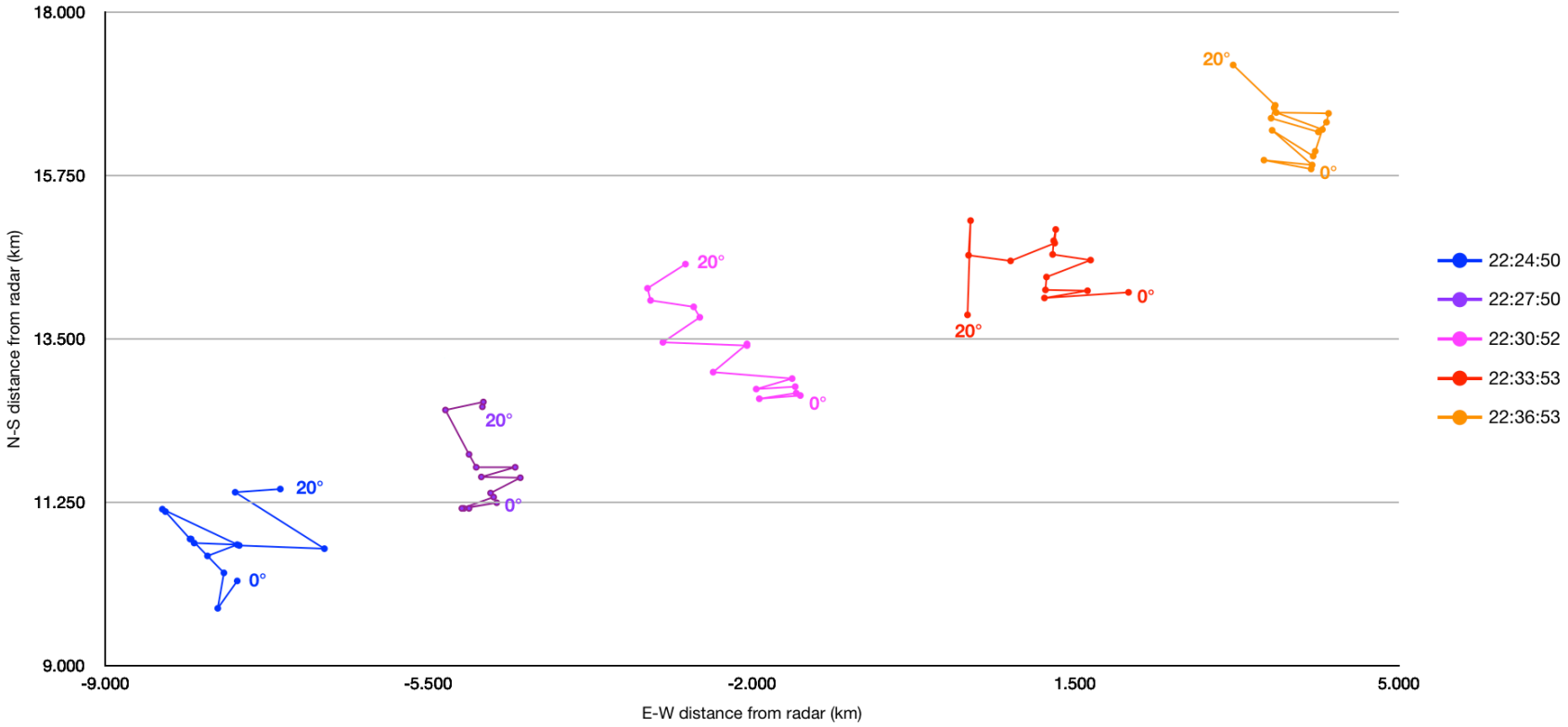

Figure 5.9: Graph of vortex tilt with height for the Elmer-Tipton tornado at five different times during its life cycle (2224:50, 2227:50, 2230:52, 2233:53, and 2236:53 UTC). Each colored line represents a different time (see legend for the time corresponding to each color), and each point on each line represents a different elevation angle from 0°-20°. Distances given are radar-relative; the x-axis represents the vortex's east-west distance from the MWR-05XP, and the y-axis represents its north-south distance from the MWR-05XP.

vortex tilted generally toward the northwest up to approximately 3.5 km ARL and then abruptly toward the east or southeast from 3.5-4 km ARL. Subsequently, the vortex became increasingly tilted toward the northwest (slightly upshear) with height through at least 2230:52 UTC, and by 2233:53 UTC, the low-level (0.4-0.8 km ARL) and upper-level vortex (above 4 km ARL) exhibited tilt toward due west. Tilt appeared to decrease throughout the vortex by 2236:53 UTC. Except for early in its life cycle, the TVS did not follow the direction of the southwesterly 0-6 km environmental wind shear vector (not shown), which contrasts the findings of Griffin et al. (2019) and those for the Amber-Bridge Creek tornado discussed in chapter 3. Given the generally limited tilt in the low levels and change in tilt in the midlevels, particularly at 2227:50 and 2233:53 UTC, the vortex followed, in a very crude sense, the RAP proximity hodograph taken 17 km east of Tipton, which featured an inflection point between 2 and 3 km AGL (Fig. 5.10). However, the frequent westerly or northwesterly tilt of the vortex is not reflected in the proximity hodograph. Perhaps the supercell's RFGF was impacting the vortex throughout D1 and D2, displacing the near-surface TVS to the east of the mid- and upper-level TVS, which would promote a general westward or northwestward tilt with height. The RFGF may have occluded around 2233:53 UTC, which would propel the low-level vortex well to the east of the mid- and upper-level vortex, a possible explanation for the extreme westward tilt of the vortex at this time.

5.3.3 Vortex Periodicity

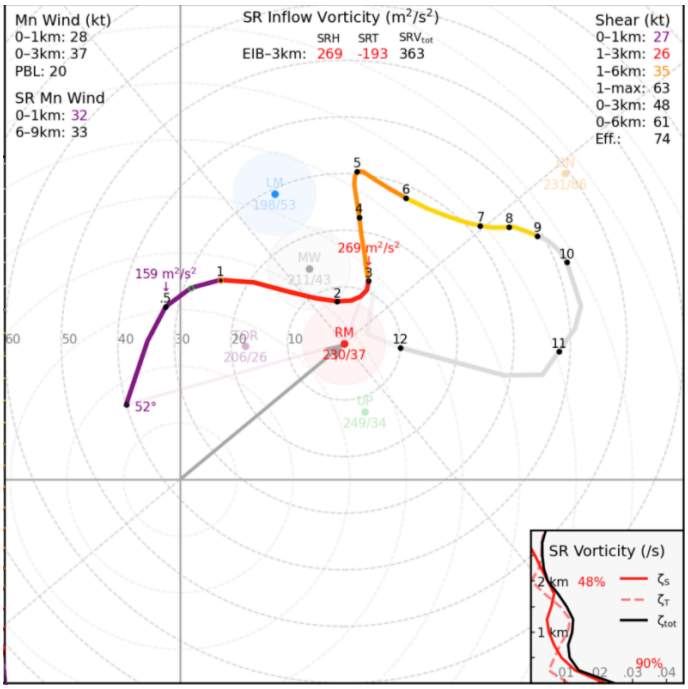

Figure 5.10: RAP model proximity hodograph from 17 km east of Tipton, OK, valid at 2300 UTC 16 May 2015. Taken from Nixon (2021).

The Elmer-Tipton tornado underwent frequent oscillations in low-level vortex intensity, particularly after the rapid intensification phase occurred. Fig. 5.11 illustrates the progression of Δv_{max} between 2230:20 (the approximate start of the rapid intensification phase) and 2237:40 UTC (the end of D2). The most significant oscillations began at 2232:06 UTC with an initial period of 54-81 s and amplitude of about 20-30 m s^{-1}. through 2234:20 UTC. Subsequently, the period decreased dramatically, varying between 19 and 34 s as the oscillations became more frequent through the end of D2, while the amplitude remained roughly the same (save for a brief increase in period and amplitude to 85 s and 38 m s^{-1}, respectively, between 2235:40 and 2237:05 UTC).

For the 2234:20-2235:40 UTC and 2237:05-2237:40 UTC intervals, the oscillatory period was much shorter than that observed by Wurman et al. (2013) in the

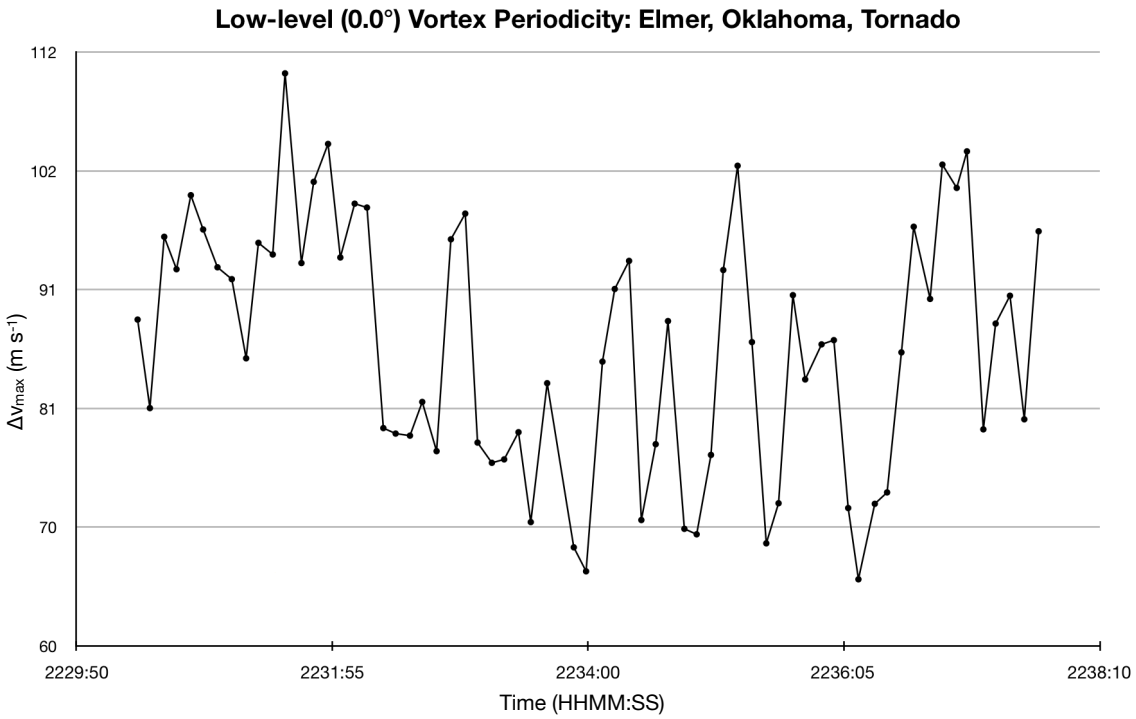

Figure 5.11: Graph of Δv_{max} at 0° (0.4 km ARL) from 2230:20-2237:40 UTC.

Goshen County, WY, tornado, which varied from 66-108 s; the amplitude of oscillations was significantly greater than that of the Goshen County tornado—approximately 4 m s^{-1}—for the entirety of the 2232:06-2237:40 UTC interval. In addition, Mahre et al. (2018) also studied the Elmer-Tipton tornado and discovered oscillations in low-level vortex intensity later in the tornado's life cycle with a period of approximately 60 s, similar to the Goshen County tornado. In these cases, the fluctuations were likely the result of longer-wavelength, Rossby-type waves slowly revolving around the vortex, rather than faster-orbiting subvortices within the main tornado (Wurman et al. 2013). However, given the much higher-frequency, higher-amplitude nature of the oscillations found in this study and that they were roughly on the order of the advective time scale of the tornado (about 20 s), it is possible that the oscillations depict subvortices rotating around the main

vortex. While MWR-05XP data did not explicitly indicate subvortices, perhaps due to resolution limitations, storm spotters near the tornado reported multiple-vortex structure just after the end of D2 (Fig. 5.12).

5.4 Selected Radar Signatures

The Elmer-Tipton supercell produced several radar signatures common among tornadic supercells. At 2224:24 UTC, a substantial increase in Z_{DR} began in the low levels (2°, RaXPol) on the southern edge of the forward flank and continued through tornadogenesis (Fig. 5.13), similar to the cases presented in Wilson (2019). This increase in Z_{DR} suggests size sorting of hydrometeors, particularly the melting graupel/hail field, within the forward flank by the storm relative winds (Dawson et al. 2014), yielding the formation of a Z_{DR} arc as described by Kumjian and Ryzhkov (2008). The Z_{DR} arc decreased in intensity (2-4 dB throughout the feature) and was no longer discernible by 2230:45 UTC, in part because of hail that began to fall on the southern edge of the forward flank at 2227:49 UTC.

In addition, a WEH was coincident with the TVS for a portion of D1 and D2. The WEH was slightly more difficult to resolve than that of the Amber-Bridge Creek case and often did not feature an area of 0 dBZ within its boundary. Therefore, the WEH will be analyzed in a more qualitative fashion for this case as opposed to the more quantitative approach used in the Amber-Bridge Creek case.

At 0° (0.4 km ARL), the Elmer-Tipton supercell exhibited a distinct hook echo well before tornadogenesis, and precipitation quickly wrapped around the TVS as

Figure 5.12: Video still image showing the multiple-vortex structure of the Elmer-Tipton tornado taken at between 2240 and 2245 UTC approximately 19 km west-southwest of Tipton, OK. At least three separate vortices are noted, indicated by the white arrows. Courtesy of Stephen Jones.

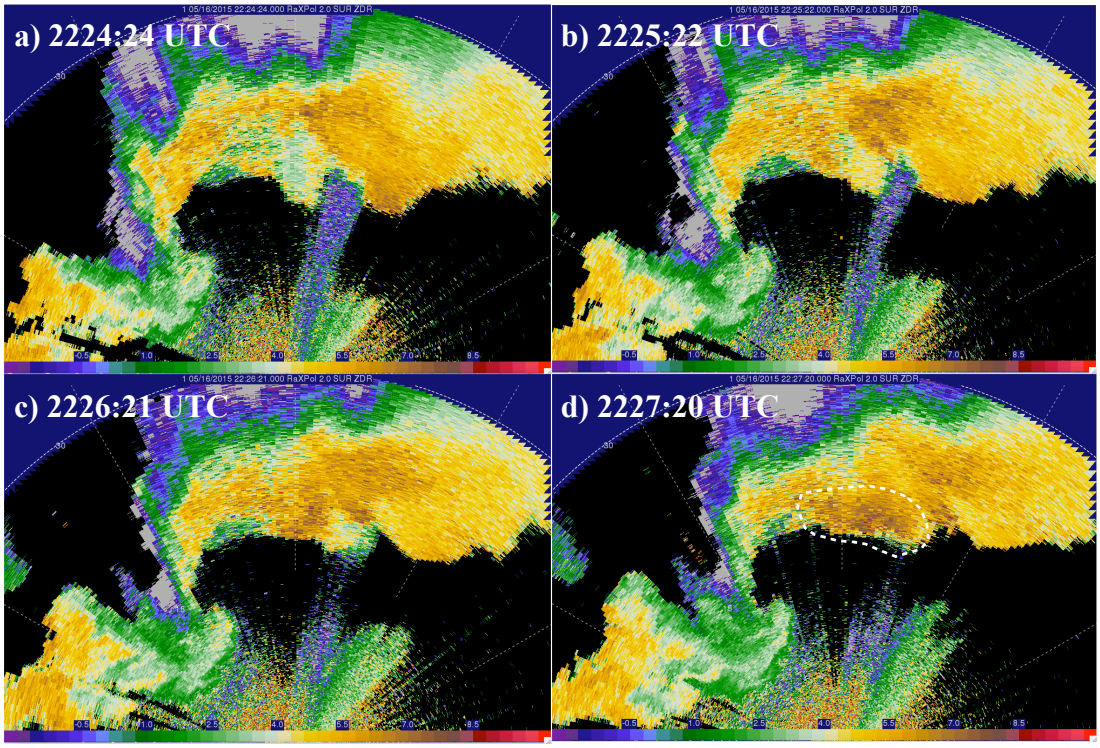

Figure 5.13: Z_{DR} (dB) imagery from RaXPol at 2° (1 km ARL) at approximately 1-min increments from 2224:24-2227:20 UTC. The white, dashed outline in (d) denotes the Z_{DR} arc.

tornadogenesis was ongoing. The hook echo closed off completely by 2226:51 UTC, producing a low-level WEH through 2227:34 UTC (Fig. 5.14). Subsequently, the WEH filled in, and an open hook echo reappeared through the end of D1. By the start of D2, a WEH had, once again, developed but had opened up again by 2230:12 UTC; a third and final cycle of the WEH occurred from 2231:19-2232:20 UTC before it devolved into a hook echo for the remainder of D2 (Fig. 5.15). The cyclical nature of the WEH could represent changes in the characteristics and intensity of the RFGF, periodic pulses of precipitation around the vortex, or debris centrifuging; the fluctuations roughly match the periods of intensification discussed in Section 5.3.1. The initial decrease in Δr during the first, more gradual intensification phase began at 2226:51 UTC, when the WEH first appeared, and at 2229:53 UTC, both the second, more rapid intensification phase and the second cycle of the WEH began. Above 0°, the presence of a coherent WEC was fairly inconsistent throughout D1 and D2, and there was evidence of a WEH coincident with the TVS only at elevation angles up to 6° (1.7 km ARL), at which a WEH was only evident during D1 from 2225:59-2226:34 UTC and then intermittently until about 2233 UTC. In addition, a well-defined bounded weak echo region (BWER; Marwitz 1972, Nelson and Braham 1975, Lakshmanan and Witt 1996) was present above 15° (Fig. 5.16), indicative of a very strong updraft. The BWER was roughly crescent-shaped, as is frequently noted in observed (Bluestein et al. 2010; Snyder et al. 2013; Houser et al. 2015) and simulated (Snyder et al. 2010; Dennis and Kumjian 2016) supercells.

By 2227 UTC, a second WEC developed above 9° (2.5 km ARL) up to 15° (4 km ARL); however, it was always displaced approximately 1 km from the TVS (Fig. 5.17).

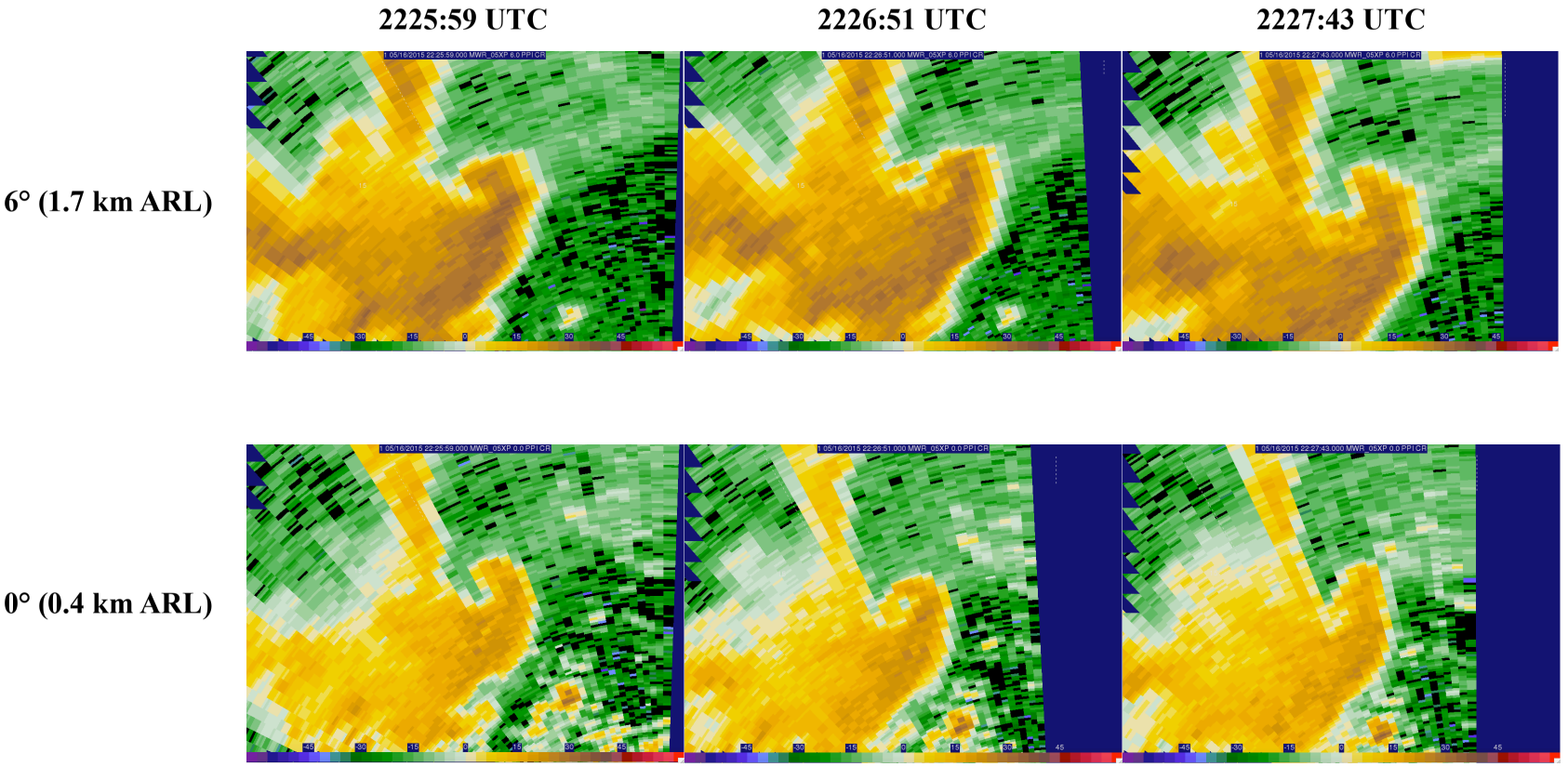

Figure 5.14: Sequence of reflectivity images (from top to bottom) at 0° (0.4 km ARL) and 6° (1.7 km ARL) showing the evolution of the WEH during D1.

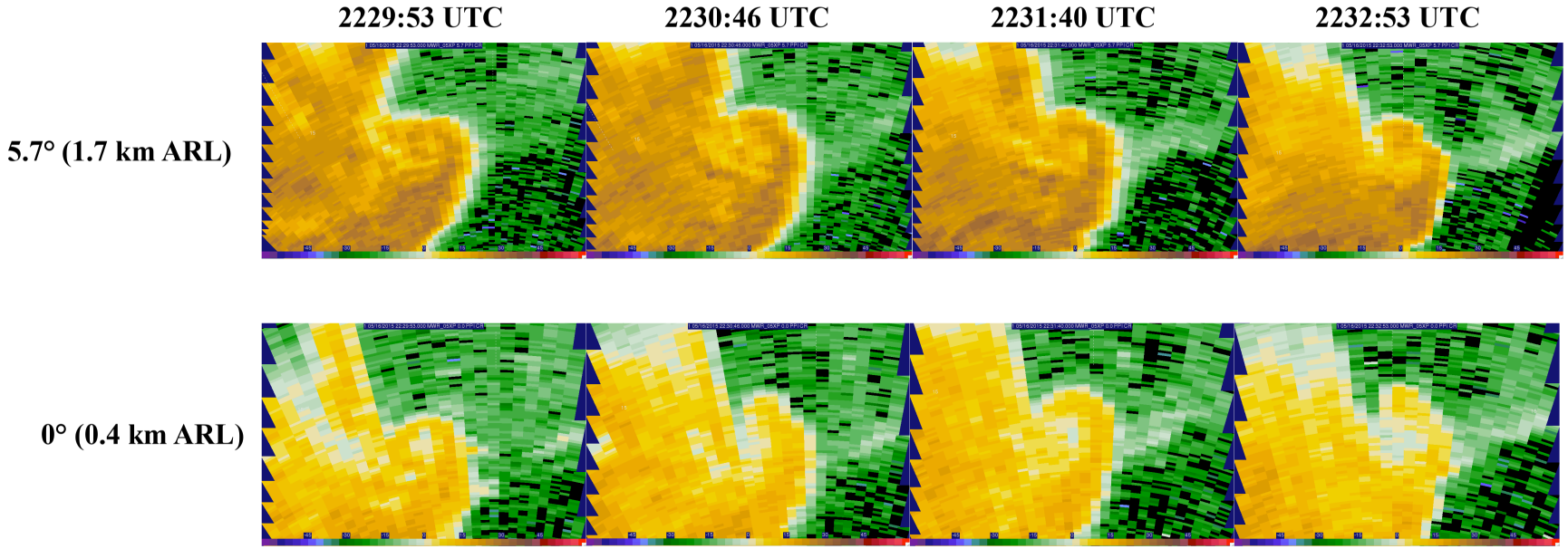

Figure 5.15: Sequence of reflectivity images (from top to bottom) at 0° (0.4 km ARL) and 5.7° (1.7 km ARL) showing the evolution of the WEH during D2.

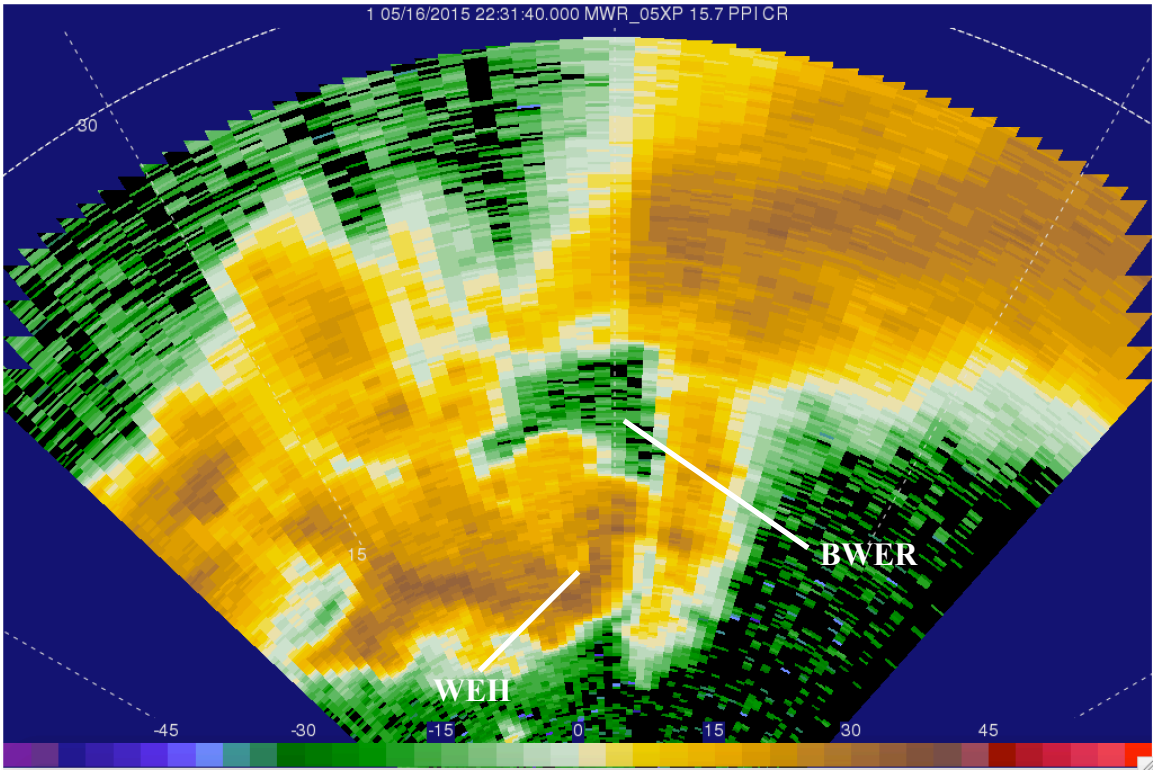

Figure 5.16: Reflectivity (dbZ) at 2231:40 UTC at 15.7° (4.5 km ARL) in elevation. The BWER and WEH are denoted.

The tornado appeared to rotate cyclonically around the second WEC. At 10°, the WEC lasted until about 2230:46 UTC, after which it opened up into a hook echo. By 2231:40 UTC, the hook echo closed off, and a band of lower reflectivity (referred to herein as the low-reflectivity band, or LRB) containing values about 10-30 dBZ less than surrounding areas developed on the southern and southwestern flank of the TVS, lasting until 2233:53 UTC (Fig. 5.18). The LRB was colocated with a gradient in intensity of inbound velocities, with higher (lower) values along its northern (southern) edge. There may have been an updraft in the location of the LRB that may have advected precipitation upward, yielding the region of lower reflectivity. A similar, though much more distinct, LRB was documented in the vicinity of a violent tornado near El Reno, OK, on 24 May 2011

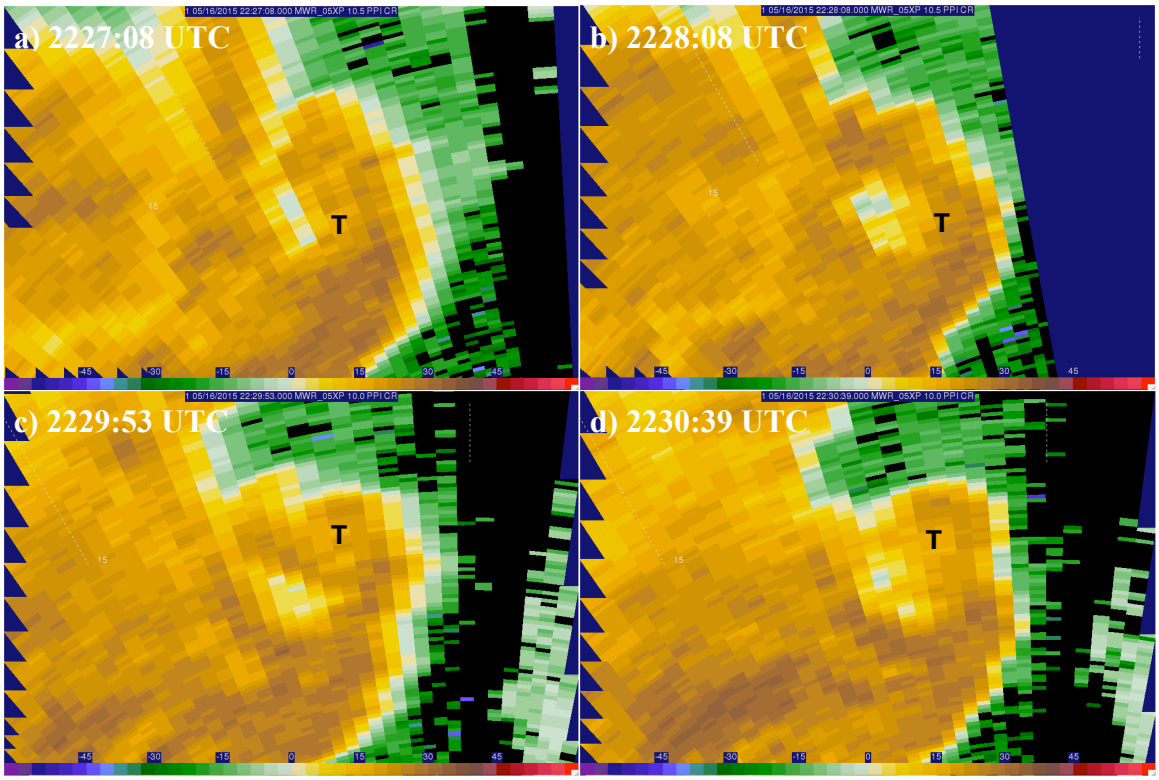

Figure 5.17: Reflectivity (dbZ) at a) 2227:08, b) 2228:08, c) 2229:53, and d) 2230:39 UTC at 10° (c, d) and 10.5° (a, b; 5 km ARL) in elevation. The location of the TVS at each time is denoted by the black "T".

(Houser et al. 2016). In that case, however, the LRB formed from a convergence zone associated with a SRFGF, whereas the LRB accompanying the Elmer-Tipton tornado was the result of inflow winds wrapping around the tornado. In addition, Snyder (2013) documented the low-reflectivity ribbon (LRR), a narrow band of decreased reflectivity and Z_{DR} located near where the hook echo along the upshear side of a supercell interacts with the rear part of the forward-flank downdraft. Griffin et al. (2018) hypothesized that the LRR represents a particle size distribution comprised of either small liquid hydrometeors or small concentrations of hail mixed with small drops, as in the El Reno, OK, tornado documented in Houser et al. (2016). Above 10°, the WEC never devolved

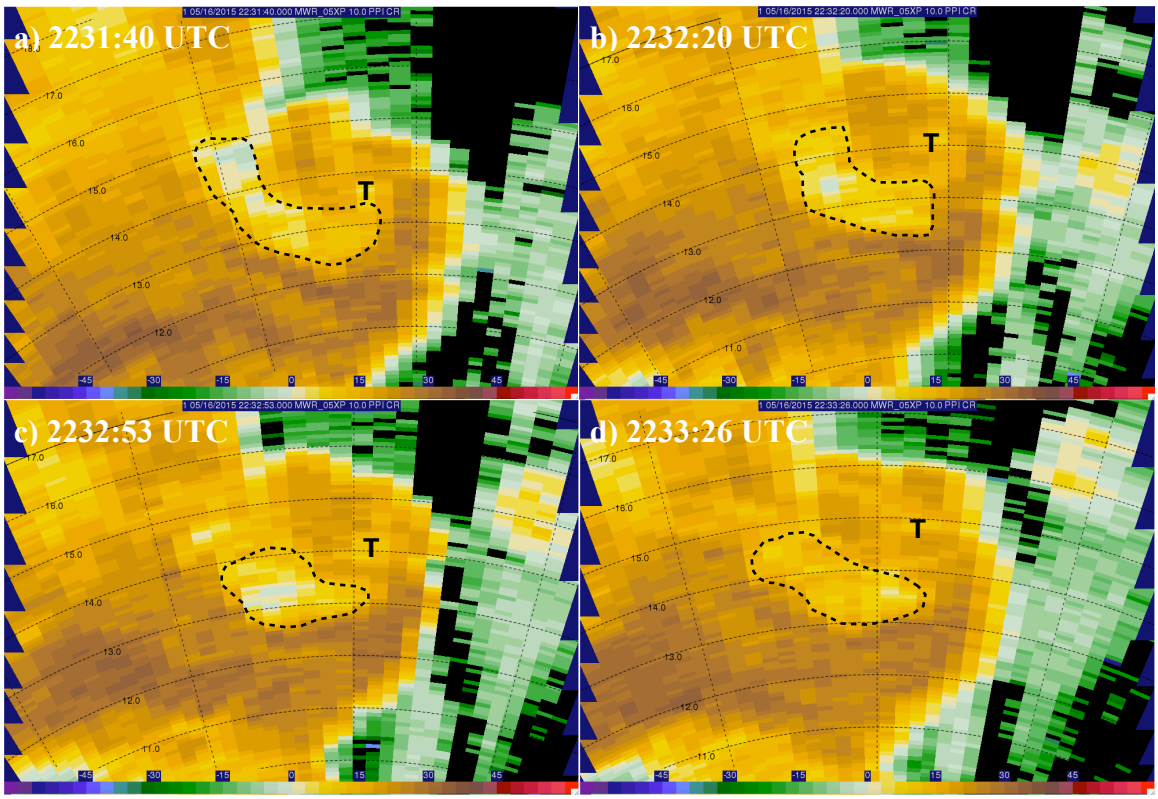

Figure 5.18: Reflectivity (dbZ) at a) 2231:40, b) 2232:20, c) 2232:53, and d) 2233:26 UTC at 10° (c, d) and 10.5° (a, b; 5 km ARL) in elevation. The LRB is demarcated by the black dashed line, and the location of the TVS at each time is denoted by the black "T".

into an open hook echo but did transform into an LRB, although not as well-defined as at 10°, over the same time period.

Chapter 6

The Marietta, OK, Tornadic Supercell: 1 May 2019

6.1 Synoptic Overview

On 1 May 2019, a large, high-amplitude 500-mb trough was situated across the western half of the United States with a belt of 25 m s^{-1} flow draped across the central and northern Great Plains (Fig. 6.1a). Southern Oklahoma and northern Texas were slightly removed from this zone of enhanced mid-level flow, but southwesterly 20 m s^{-1} 500-mb flow atop south-southeasterly surface winds produced deep-layer shear adequate for supercells in this region. However, low-level shear was modest (Fig. 6.3b) except along a well-defined outflow boundary (Fig. 6.2) stretching from the Memphis, TN, area southwestward into northeast Texas and far southern Oklahoma at 1800 UTC. This boundary was spawned and reinforced by a convective complex that impacted eastern Oklahoma and much of Arkansas throughout the morning.

Despite a modest low-level jet (10 m s^{-1} winds at 850 mb, as shown in Figure 6.1b), a very moist airmass was already established east of a dryline in the Texas Panhandle and south of a southwest-to-northeast oriented stationary front that bisected

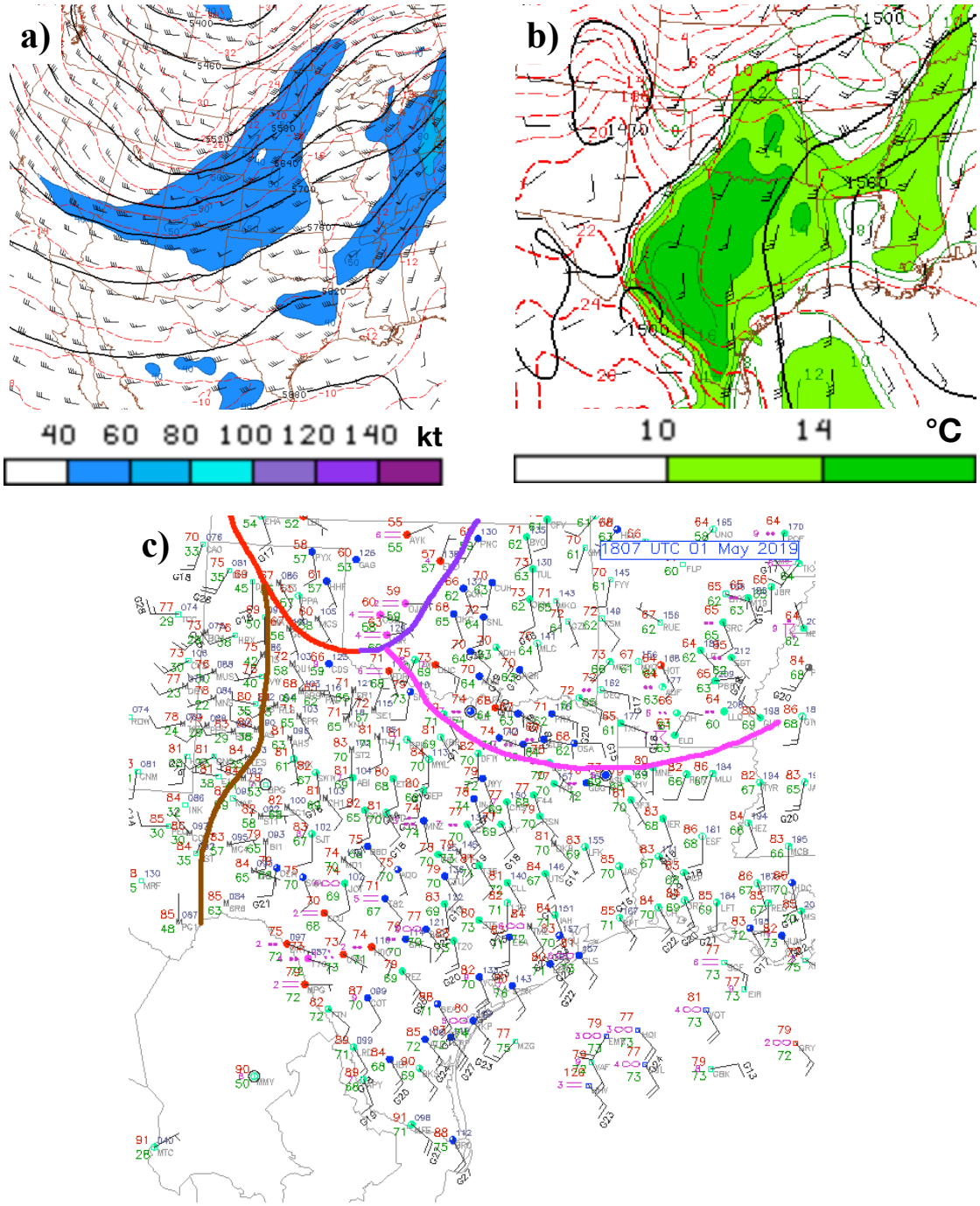

Figure 6.1: Overview of the synoptic environment on 1 May 2019. Pictured above are a) 500 mb winds and b) 850 mb winds and moisture, valid at 1800 UTC, and c) surface analysis with the approximate locations of key features valid at 1807 UTC. In (c), the red line represents a warm front associated with a surface low in southeast Colorado (not pictured), the brown line represents the dryline, and the purple and pink lines represent the stationary front and outflow boundary, respectively. Adapted from the Storm Prediction Center Mesoanalysis Archive.

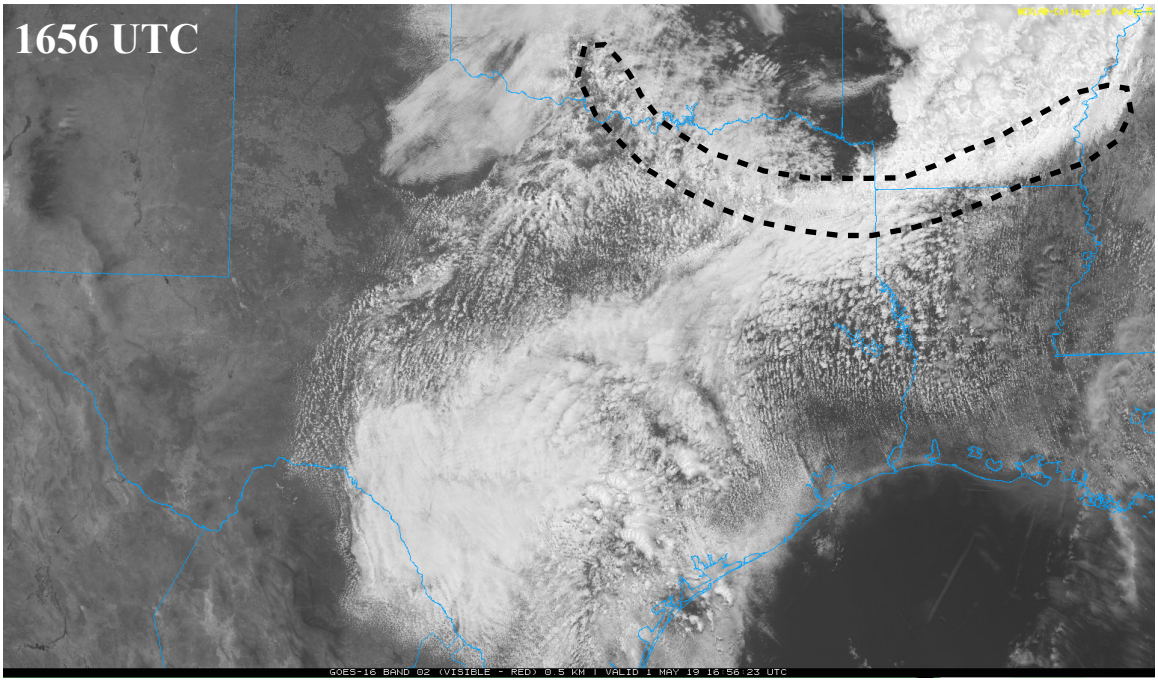

Figure 6.2: Visible satellite image taken at 1656 UTC 1 May 2019. The outflow boundary is clearly visible as a thin band of clouds (demarcated by the dashed black polygon) beginning in southwest Oklahoma and arcing through northeast Texas and far southern Arkansas.

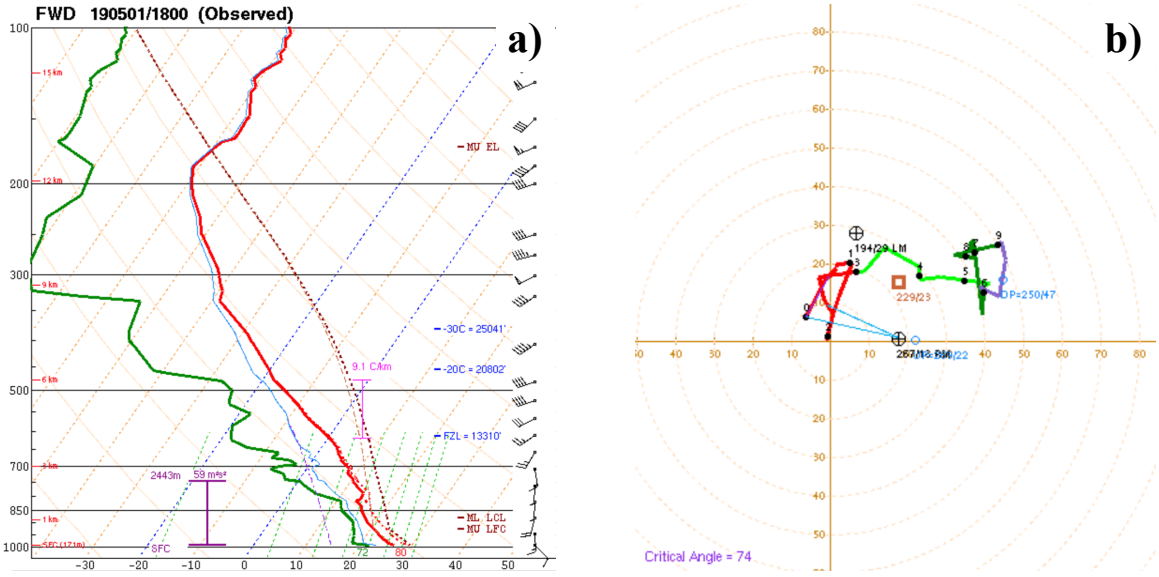

Figure 6.3: KFWD (Fort Worth, TX) a) sounding and b) hodograph, valid at 1800 UTC 1 May 2019. Taken from the Storm Prediction Center Severe Weather Events Archive.

Oklahoma. Just south of the outflow boundary, the 1800 UTC Fort Worth, TX, sounding (Fig. 6.3a) sampled a surface temperature and dewpoint of 80°F (27°C) and 72°F (22°C), respectively, beneath mid-level lapse rates exceeding 8°C km^{-1}. As a result, MLCAPE values of 3000-4000 J kg^{-1} were prominent in southern Oklahoma and northern Texas. The outflow boundary intersected the stationary front in southwest Oklahoma (Fig. 6.1c), producing an effective triple point on which convective initiation occurred by 1730 UTC given very weak MLCIN.

6.2 Supercell Formation and Evolution

After initiation, semi-discrete storms developed near and to the southwest of the effective triple point. These storms rapidly became supercellular given their proximity to the outflow boundary, and three tornadoes occurred in two separate storms near Throckmorton, TX, at 1839 and 1903 UTC, and near Loco, OK, at 1908 UTC. Over the next hour, the storm mode became less favorable for tornadoes, as new storms continued to form and cluster with the ongoing activity. However, by 1940 UTC, showers began to develop ahead of the ongoing broken line of storms; the Marietta supercell originated as one of these showers near Nocona, TX. As the shower moved northeastward, it quickly intensified and attained a kidney bean shape on radar as midlevel rotation increased. The storm remained discrete as it crossed the Red River into Oklahoma, and low-level rotation began to increase by 2046 UTC and continued to increase after 2100 UTC. Fig. 6.4 documents the evolution of the Marietta supercell using reflectivity imagery from the KFDR radar.

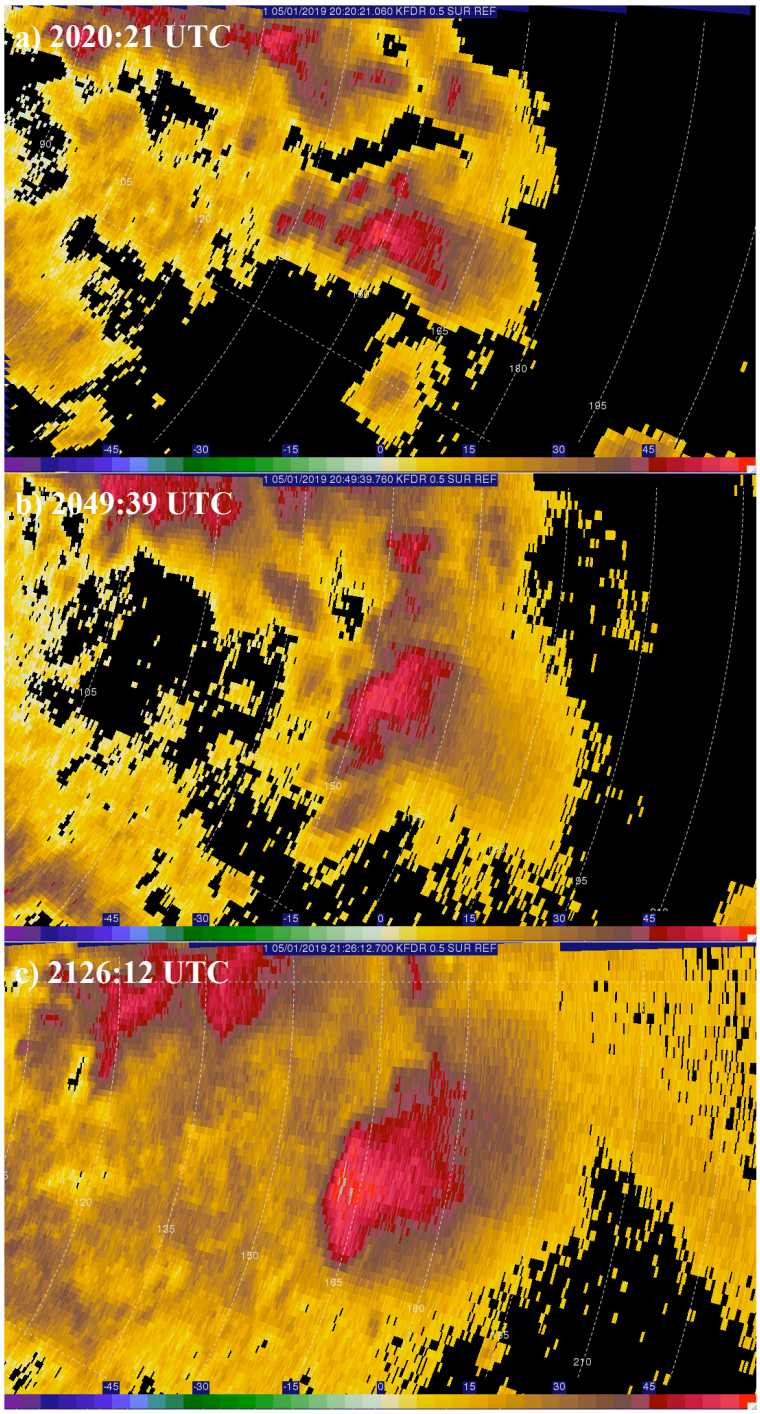

Figure 6.4: Evolution of the supercell that produced the Marietta tornado using 0.5° reflectivity (dBZ) data from the KFDR radar. Included are a) the storm as it began to take on a "kidney bean" shape at 2020:21 UTC, b) the supercell as low-level rotation began to increase at 2049:39 UTC, and c) the supercell as it was producing the Marietta tornado at 2126:12 UTC. Each panel follows the storm as it moves; therefore, the area displayed in each panel is different.

6.3 The Marietta Tornado

RaXPol was deployed six times along Oklahoma State Highway 32 between 2039 and 2245 UTC (Fig. 6.5). Initially, the storm intercept crew targeted the aforementioned Loco, OK, tornadic supercell but was unable to deploy before the tornado dissipated. Because the Throckmorton, TX, supercell was also out of reach, the crew decided to await further development in Southern Oklahoma. Once low-level rotation in the Marietta supercell began to increase, RaXPol was deployed and began collecting data. NWS Norman (2019) determined that the Marietta supercell produced two EF0 tornadoes, one 8 km west to 3 km west of Marietta from 2121-2129 UTC (Fig. 6.6) and one 8 km north of Marietta from 2146-2148 UTC. The third and fourth deployments (D3 and D4) captured the tornadoes spawned by the Marietta supercell from the west; this study will focus on the tornado and other significant features that occurred during D3, which lasted from 2123:53-2135:01 UTC and features data up to 20° in elevation[1]. The first, second, fifth, and sixth deployments did not include any tornadic activity; therefore, they will not be analyzed in this study.

6.3.1 Evolution of the TVS with Height and Time

The TVS coincident with the tornado that occurred during D3 was documented from 2123:53-2127:33 UTC and remained fairly steady state throughout the deployment, making significant trends in Δv_{max}, Δr, and ζ_{pseudo} difficult to ascertain. Δv_{max} at the lowest elevation angle did not meet the 40 m s^{-1} threshold until 2126:41 UTC (Fig. 6.7a), while

[1] The location at which D3 occurred was surrounded by trees that blocked the radar beam at the lowest elevation angle between 2124:41 and 2125:29 UTC.

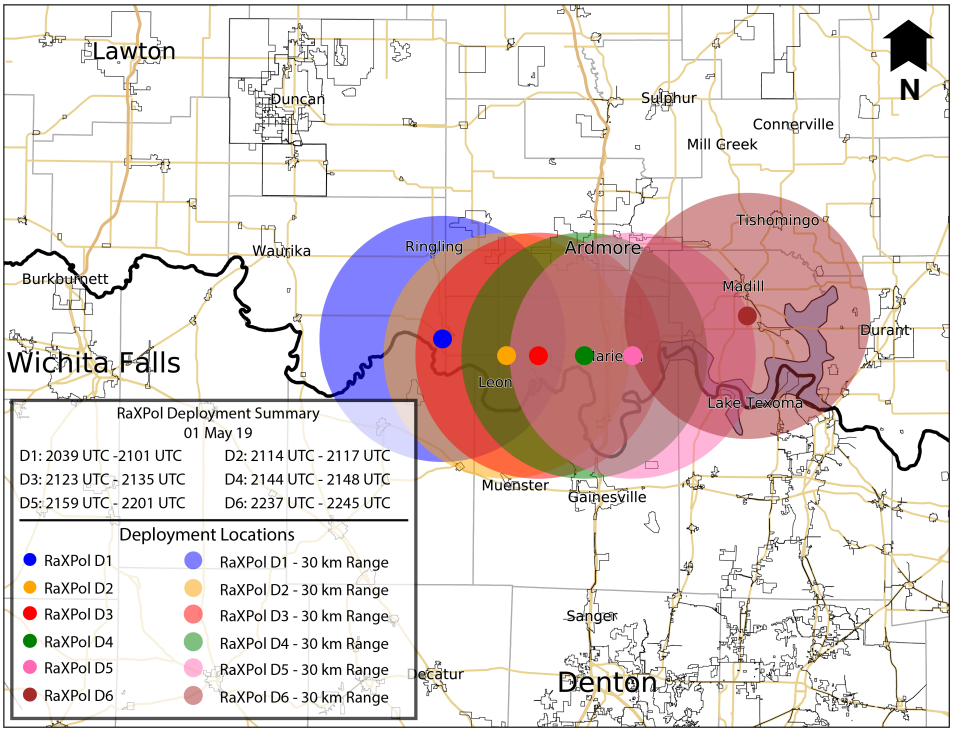

Figure 6.5: RaXPol deployment map for 1 May 2019. As illustrated in the legend, colored dots represent the locations of each RaXPol deployment, and the opaque, color-filled circles represent RaXPol's 30-km range. Courtesy of Dylan Reif.

Figure 6.6: Video still of the first Marietta tornado at approximately 2125 UTC. Courtesy of Adam Reagan.

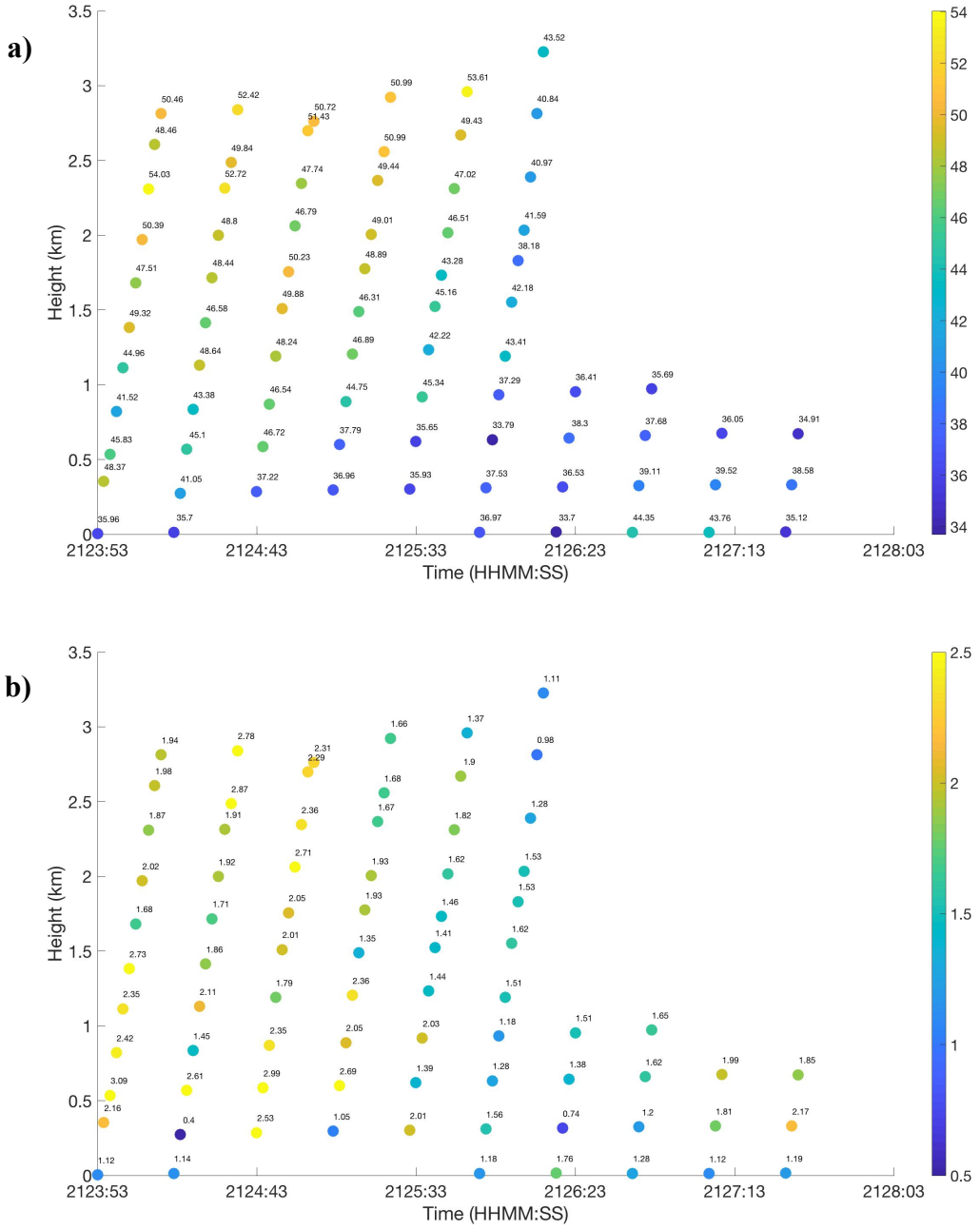

Figure 6.7: Scatterplots for the TVS that occurred during D3 of a) Δv_{max} (in m s^{-1}), b) Δr (in km), and c) ζ_{pseudo} (in s^{-1}; next page) as a function of time versus height.

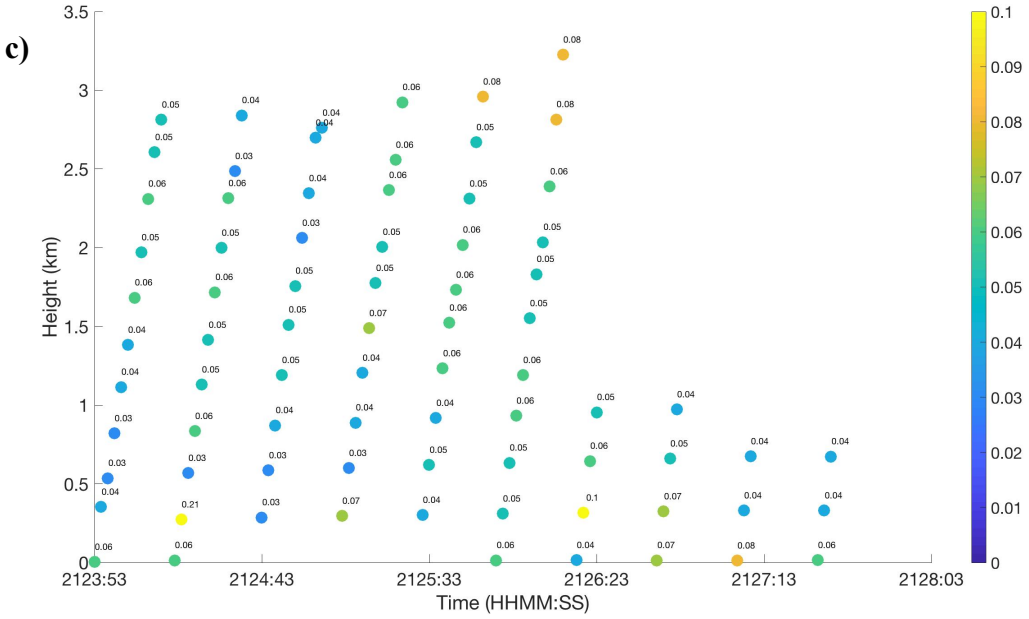

Figure 6.7 (continued).

the near-surface vortex met the Δr and ζ_{pseudo} criteria throughout the entire deployment (Figs. 6.7b, c). A dissipation phase appeared to be underway below 1 km ARL at the start of D3, first beginning just above the surface (approximately 0.3 km ARL) and gradually working upward with time until at least 2126:17 UTC, after which the TVS became ambiguous or nonexistent above 1 km ARL. Between 2125:39 and 2126:03 UTC, Δv_{max} decreased abruptly at all elevation angles above 1.5 km ARL; however, near-surface Δv_{max} increased from 33.70 m s^{-1} to 44.35 s^{-1} between 2126:17 and 2126:41 UTC. The near-surface vortex remained at tornado strength until 2127:05 UTC, after which it weakened below the 40 m s^{-1} threshold.

While the near-surface vortex satisfied the Δr threshold throughout D3, the vortex aloft was quite broad at the beginning of D3 before gradually decreasing in size. Between 2124:51 and 2125:25 UTC, Δr decreased at all levels within the TVS with the exception

of approximately 1.2 km ARL. This trend generally continued through the volume scan beginning at 2125:53 UTC, in which Δr met the 2 km threshold at all elevation angles. Throughout the deployment, near-surface Δr remained fairly steady, save for an abrupt increase between 2125:53 and 2126:17 UTC and succeeding decrease coincident with near-surface Δv_{max} first exceeding the 40 m s^{-1} threshold. This yielded a modest increase in near-surface ζ_{pseudo} from 2126:41-2127:05 UTC, although the ζ_{pseudo} field was fairly uniform throughout the TVS during D3.

6.3.2 Vortex Tilt with Height

The TVS exhibited varying tilt throughout D3. At the beginning of the deployment, the vortex tilted toward the south or southeast below approximately 0.8 km ARL and then generally toward the north above that level (Fig. 6.8a). The vortex then began to tilt toward the northwest or west for the remainder of the deployment (Figs. 6.8b, c). Unlike the Bridge Creek and Putnam tornadoes, the tilt of the Marietta TVS followed neither the ambient wind shear vector, as in Griffin et al. (2019; not shown), nor the general shape of the proximity environmental hodograph (Fig. 6.9; in this case, the observed sounding from Fort Worth, TX, at 2100 UTC). In fact, the vortex tilted in the opposite direction of the proximity hodograph, particularly in the latter half of the deployment. This tilt may have occurred because the RFGF may have displaced the low-level vortex to the east or southeast of the mid- and upper-level vortex, yielding the northwestward or westward tilt. In addition, the overall weaker-shear environment may have allowed stronger outflow production in the Marietta storm (Rasmussen and

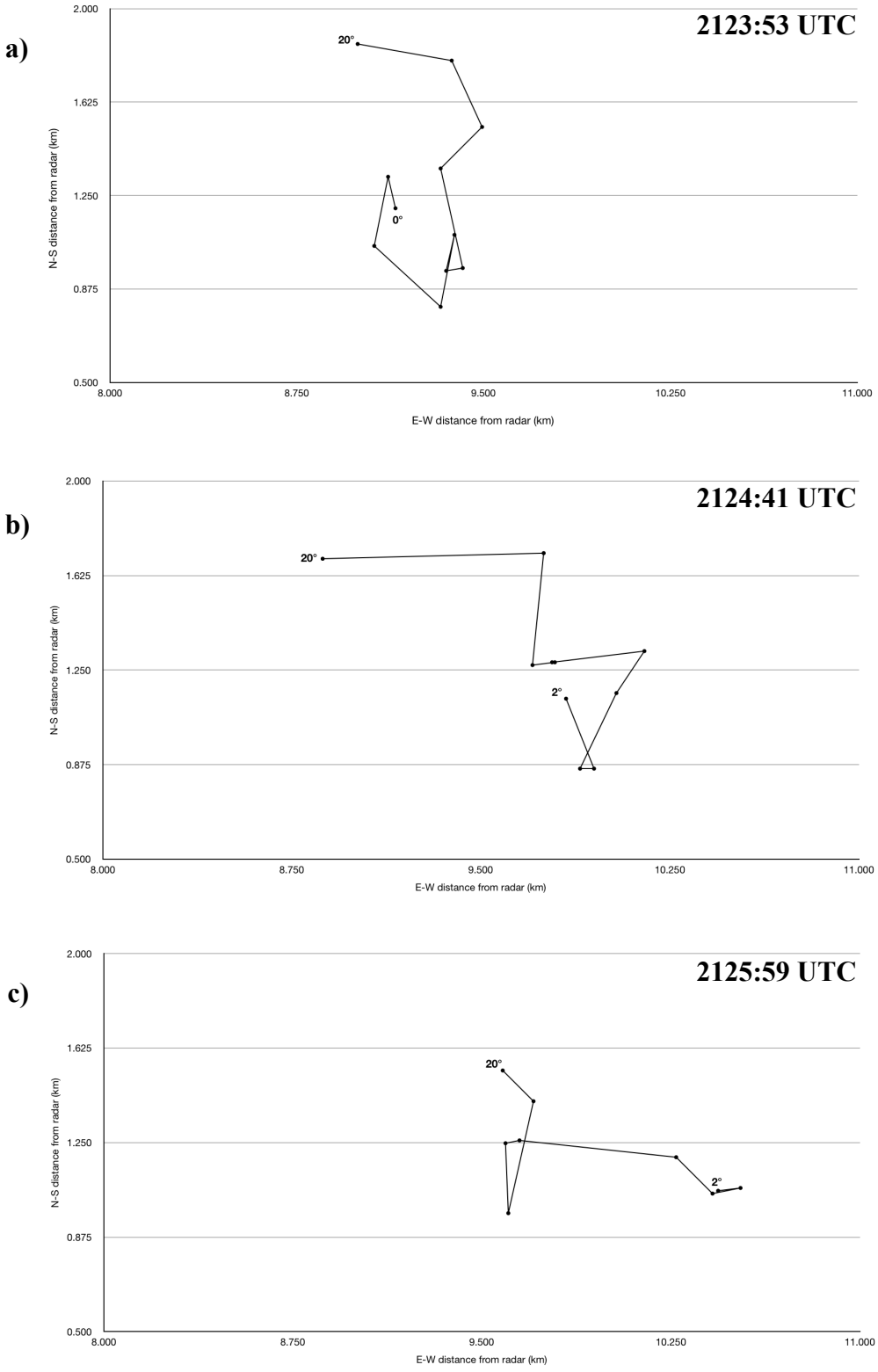

Figure 6.8: Graph of vortex tilt with height for the TVS during D3 at a) 2123:53 UTC, b) 2124:41 UTC, and c) 2125:29 UTC.

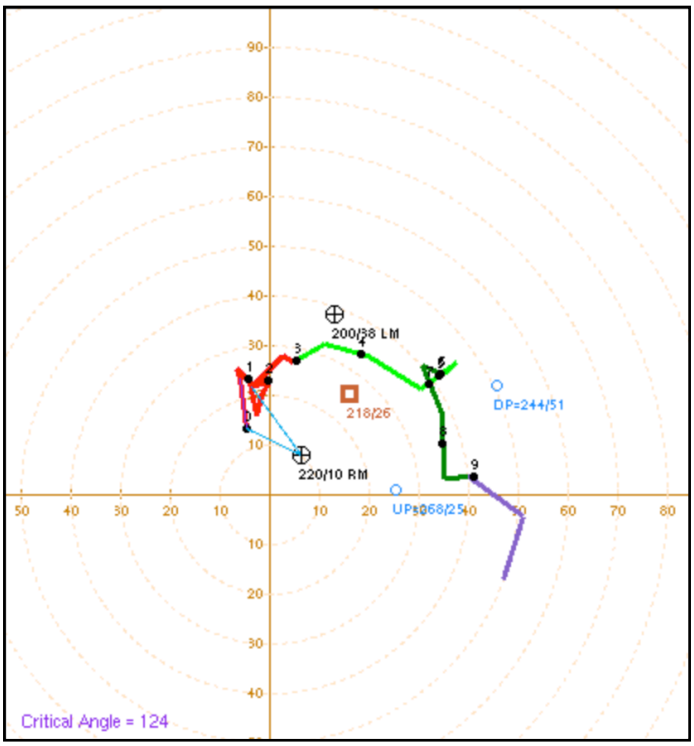

Figure 6.9: Proximity observed hodograph from Fort Worth, OK, valid at 2100 UTC 1 May 2019.

Blanchard 1998), which may also have impacted the tilt of the vortex.

6.4 Secondary Vortices

Perhaps the most distinct features of the Marietta supercell were the numerous subtornadic vortices that occurred aloft in tandem with the main TVS. RaXPol documented at least four of these secondary vortices (SVs), three of which were anticyclonic and one cyclonic. As in the Amber-Bridge Creek case, these vortices were only apparent above approximately 1 km ARL, and they lasted generally between 4-5 minutes. In addition, they were all embedded in precipitation[2], as was documented in the

[2] Similar vortices completely embedded in precipitation were documented by RaXPol in a supercell near Dickson, OK, on 3 May 2021.

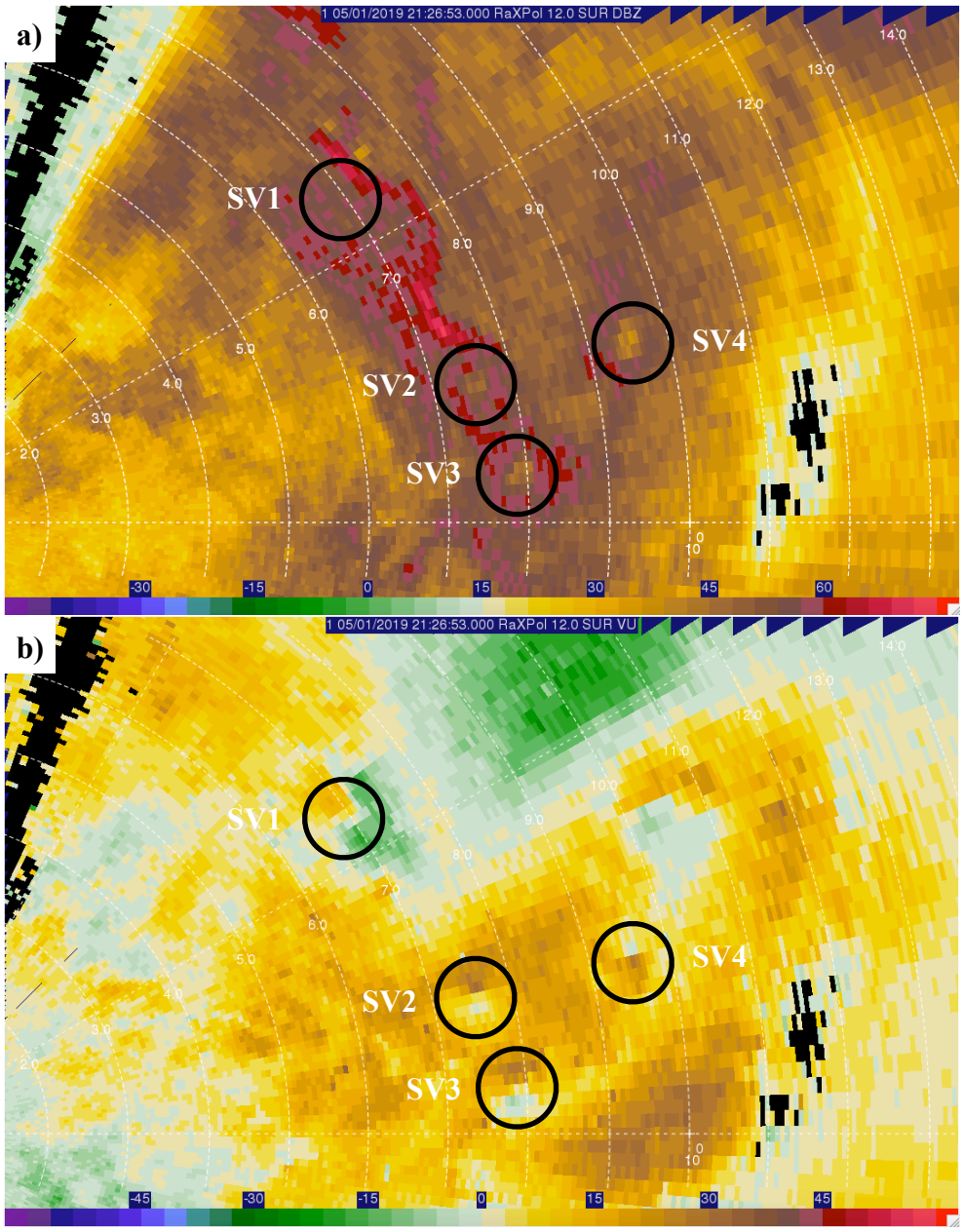

Figure 6.10: a) Reflectivity (dbZ) and b) radial velocity (m s^{-1}) at 12° (1.5 km ARL) in elevation at 2126:53 UTC. SV1-3 are anticyclonic, while SV4 is cyclonic. Black circles represent the locations of each secondary vortex. Range rings are included at 1-km increments.

Putnam case. Fig. 6.10 illustrates the location of and assigns labels to each vortex.

The three anticyclonic vortices (SV1, SV2, and SV3) were all located along a northwest-to-southeast-oriented band of enhanced reflectivity on the backside of the main mesocyclone. In general, they moved to the southeast along this high-reflectivity band, although there were notable deviations from this, one of which will be discussed shortly. It appears that the southerly mid- and low-level ambient winds west and southwest of the updraft (Fig. 6.3b) and the northerly and northwesterly winds wrapping around the rear of the mesocyclone created a vortex sheet (Kundu et al. 2012), denoted by the high-reflectivity band. However, there is no evidence of a vortex sheet in the radial velocity field, although the strong winds indicative of a vortex sheet would be aligned roughly normal to the radar beam, perhaps causing it to be mostly unobservable. Thus, there may have been a vortex sheet above the vertical domain of the radar that built downward. Assuming that there was, in fact, a vortex sheet, shearing instability likely caused the vortex sheet to break up into multiple anticyclonic vortices that rolled up along it (Krasny 1993).

RaXPol also documented vortex interaction between SV2 and SV3. Throughout its life cycle, SV2 traveled to the southeast along the possible vortex sheet, while SV3 moved slowly eastward. Between 2128:57 and 2129:21 UTC, SV3 attained a northward component of motion toward SV2, which continued to move south. The two vortices proceeded to rotate anticyclonically about each other, consistent with the Fujiwhara effect (Fujiwhara 1931), while the distance between the two vortices decreased (Fig. 6.11). After this occurred, both vortices abruptly dissipated over the remaining two volume

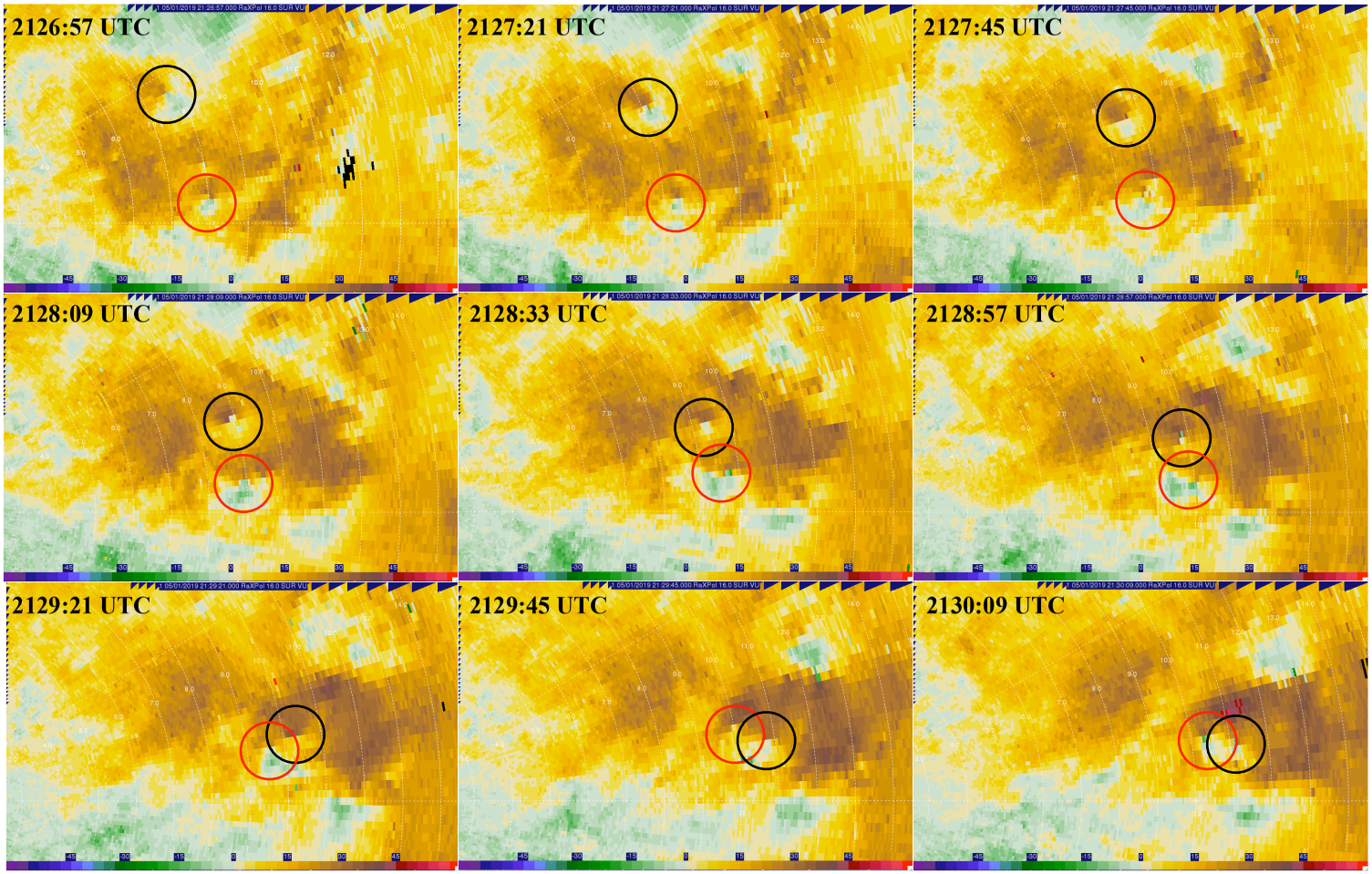

Figure 6.11: Radial velocity (m s^{-1}) at 16° (~2.3 km ARL) in elevation at 24-s increments between 2126:57 and 2130:09 UTC. Black circles represent the locations of SV2, and red circles represent the locations of SV3. Range rings are included at 1-km increments.

scans. Similar examples of vortex interaction via the Fujiwhara effect have been documented previously, including in dust devils (Bluestein et al. 2004) and misocyclones within boundaries (Marquis et al. 2007).

Chapter 7

Summary and Conclusions

During the springs of 2015 and 2019, four tornadic supercells in Oklahoma were documented by the MWR-05XP and/or RaXPol radars. The purpose of this thesis was to analyze the data collected from these storms to compare and contrast them with previous cases with the goal of identifying new features or behaviors that have yet to be documented. In particular, analyses focused on vortex behavior during tornadogenesis and decay, characteristics of each vortex during the supercell life cycle, and features that may have impacted tornado behavior or have rarely been documented previously. Also, this study aimed to identify features and behaviors that have been documented in the past to lend more credence to their roles in the supercell and tornado life cycles.

The most fruitful of the four cases was a supercell that produced an EF3 tornado from Amber to Bridge Creek, OK, on 6 May 2015. Analysis of MWR-05XP data revealed that, during dissipiation, the vortex widened and decayed an "inside-out" manner, first in the midlevels, then at slightly higher levels, and finally in the low-levels, similar to the findings of Wicker and Wilhelmson (1995), French et al. (2014) and Houser et al. (2015). As in Wurman and Gill (2000), Tanamachi et al. (2012), and others, the vortex tilted toward the northeast with height; however, it tilted much greater than the vortices studied

in these cases. The tilt of the vortex followed the 0-6 km environmental shear vector, as in Griffin et al. (2019), and, in a general sense, the RAP hodograph in proximity to the storm. The tornado also exhibited slight periodicity in its intensity, like the Goshen County, WY, tornado from VORTEX2 (Wurman et al. 2013), although the oscillations may not be significant. Finally, the Amber-Bridge Creek tornado and its parent supercell exhibited numerous significant features, including a weak-echo hole and pear-shaped weak-echo column that fluctuated in size and redeveloped after the tornado dissipated, a scalloped primary rear-flank gust front with multiple subtornadic vortices aloft, and a secondary rear-flank gust front.

The next case featured a supercell that produced at least three tornadoes, two of which were documented by RaXPol, near Putnam, OK, on 15 June 2019. The first tornado appears to have begun aloft and built downward, in contrast to French et al. (2013) and Bluestein et al. (2019), and decayed in an "inside-out" manner, like the Amber-Bridge Creek tornado. The vortex was slightly wider in the midlevels than it was in the low and upper levels, as in Bluestein et al. (2004). The nature of tornadogenesis (ascending or descending) could not be determined for the second tornado. The Putnam supercell may have undergone non-occluding cyclic mesocyclogenesis in which low-level mesocyclones move down the gust front rather than back into the precipitation core, making way for new mesocyclogenesis farther northward (Adlerman and Droegemeier 2005). Unlike the Amber-Bridge Creek case, the first Putnam tornado tilted generally toward the northwest, which followed neither the ambient wind shear vector nor RAP proximity hodograph, likely because of enhanced outflow production in the Putnam

supercell that may have displaced the low-level vortex from the mid- and upper-level vortex. However, the second tornado more closely followed the ambient shear vector and proximity hodograph. The first tornado produced a weak-echo hole and tornado debris signature, and secondary vortices formed along a shear zone and in the vicinity of the mesocyclone associated with the second tornado.

On 16 May 2015, both MWR-05XP and RaXPol probed a long-track, EF2 tornado that occurred near Elmer and Tipton, OK. Unlike the first Putnam tornado, the Elmer-Tipton tornado began near the surface and built upward with time, consistent with findings in French et al. (2013) and Bluestein et al. (2019). It intensified in a two-phased manner, the first featuring a gradual increase in intensity followed by a sudden, rapid intensification period. The vortex was not highly tilted but crudely followed the proximity hodograph. Significant periodicity with much higher frequency and amplitude than the Amber-Bridge Creek and Goshen County tornadoes (Wurman et al. 2013) was noted with the Elmer-Tipton tornado. A weak-echo hole was coincident with the tornado, and a differential reflectivity arc (Kumjian and Ryzhkov 2008) along the reflectivity gradient on the southern edge of the forward flank underwent an increase in areal extent, as in Wilson (2019), concurrent with tornadogenesis. Analysis also uncovered a band of lower reflectivity that flanked the southern and southwestern sides of the tornadic vortex, similar to the weak-reflectivity band found in Houser et al. (2016). However, the latter was hypothesized to be related to the descending branch of a horizontal roll circulation, potentially created by surface drag in the flow at the rear of the RFGF, whereas the low-

reflectivity band in the Elmer-Tipton tornado was simply caused by inflow winds (associated with clear air) wrapping around the vortex.

Finally, RaXPol documented a supercell that produced a brief, weak tornado near Marietta, OK, on 1 May 2019. Given the weak nature of the tornado, trends in vortex size and intensity were difficult to ascertain; however, the tornado exhibited varying tilt throughout the deployment. Its vertical orientation did not follow the environmental wind shear vector and opposed the proximity hodograph, likely because of enhanced outflow production, as in the Putnam supercell. The most distinct features of the Marietta supercell were several subtornadic vortices that occurred aloft along a band of high reflectivity that may have been a manifestation of a vortex sheet caused by the interaction between the southerly mid- and low-level ambient winds and the northerly and northwesterly winds wrapping around the rear of the mesocyclone. Two of these vortices appeared to undergo a Fujiwhara effect (Fujiwhara 1931) as they moved toward and rotated anticyclonically round each other.

These findings foster several points of discussion on tornado behavior. First, while the Putnam and Elmer-Tipton cases help ameliorate the relative dearth of tornadogenesis events captured by high-resolution, mobile radar, many more cases are needed to determine if ascending tornadogenesis is, indeed, favored in supercells, as documented in French et al. (2013), Bluestein et al. (2019), and others. While the Elmer-Tipton tornado first intensified near the surface and built upward with time, the first Putnam tornado appeared to build downward during its genesis. Perhaps this suggests that the degree of ambient wind shear plays a role in determining the mode of

tornadogenesis; the Putnam storm occurred in an environment characterized by weak shear, whereas the Elmer-Tipton storm occurred in a much higher-shear environment. In addition, descending tornadogenesis may be more common than previously thought because, in many cases, mobile radars may not scan high enough to discern increases in rotation in the mid- and upper levels of supercells.

Second, the varying degree of vortex tilt among the four cases poses questions about the relationship between ambient wind shear, storm-induced wind shear, and vortex tilt. The Elmer-Tipton tornado displayed a surprising lack of tilt and followed neither the proximity hodograph nor the 0-6 km environmental wind shear vector, while the Amber-Bridge Creek tornado, another strong vortex, exhibited extreme tilt and generally mirrored the background wind profile. It is well-established that tornadoes tend to tilt in the direction of the ambient wind shear vector (e.g. Wurman and Gill 2000, Tanamachi et al. 2012, French et al. 2014, and Griffin et al. 2019); thus, the fact that the Elmer-Tipton tornado, which occurred in an environment characterized by strong wind shear, did not suggests that the relationship between wind shear and vortex structure may not be as clear as previously thought. Perhaps intrinsic characteristics of the vortex play a more significant role in determining its tilt, or, perhaps more likely, how certain features of a supercell interact with a vortex may also impact vortex tilt; this would vary from case to case. In weaker-shear environments (i.e. those of the Putnam and Marietta cases), storms tend to produce increased outflow (Rasmussen and Blanchard 1998), which may be a factor in vortex tilt that does not follow the ambient wind profile. In addition, the RFGF may also displace the low levels of a vortex from its mid- and upper-levels. Once again,

investigations of tilt in many more tornado cases are needed to determine the relationship between environmental wind shear, storm-induced wind shear, and vortex tilt and what it means for tornadogenesis and storm behavior in general.

Finally, the secondary vortices that occurred during the Amber-Bridge Creek, Marietta, and Putnam cases raise questions about the how often these types of vortices occur and whether or not these vortices can become tornadic. Subtornadic vortices in supercells have been documented previously (e.g. Fujita 1981, Bluestein et al. 2007, Tanamachi et al. 2013); however, in these cases, they were most prevalent near the surface, whereas the vast majority of secondary vortices in this study were present only aloft. The formation mechanisms of the secondary vortices in this study were different from case to case, as well. Future studies are needed to determine how often these mid- and upper-level vortices occur and whether or not these vortices are a stepping stone to tornado formation in some supercells.

While numerous measures were taken to negate error within this study, there were some possible sources of error that may have impacted the results. First, as discussed in Chapter 2, Δv_{max} was calculated by manually selecting and adding the greatest inbound and outbound pixel within the TVS. Great care was taken in ensuring the most accurate Δv_{max} values were calculated; however, because an automated method to determine Δv_{max} was not employed as in some previous studies (e.g. Wienhoff 2016), some Δv_{max} values may have been slightly erroneous. However, these potential errors are not believed to have contributed to significant flaws in the analysis of vortex behavior for each case. In addition, the contour plots used to examine the behavior of Δv_{max} with respect to height

and time in the Amber-Bridge Creek case are quite noisy. The vortices analyzed in this study were generally tilted, as well, which introduced more uncertainty to the analysis gleaned from both the contour and scatterplots. As a result, another method of illustrating the relationship between Δv_{max}, height, and time may need to be employed in future studies. Finally, RAP proximity hodographs were used to represent the ambient environments near the supercells analyzed in this study; however, they may not be the most accurate depictions of near-supercell environments. Because the spatial and temporal distribution of RAP hodographs (point-based, every hour) are much greater than that of observed hodographs, which occur at fixed sites across the United States, RAP hodographs help illustrate the environment much closer to a given supercell than observed soundings can. However, they are merely models of the environmental wind field and, therefore, may not be as representative of the near-supercell environment as observed hodographs might be if they were taken proximate to a supercell.

In addition, one caveat in interpreting the behavior of Δv_{max}, particularly with respect to vortex periodicity, is that the role of convergence within the vortex was neglected in this study. It is possible that Δv_{max} remained relatively constant throughout the duration of the TVS, but the perpendicularity of the path connecting the maximum inbound and outbound velocity and the radial bifurcating the TVS decreases with increasing convergence, thus potentially falsely increasing Δv_{max} values. This enhancement to Δv_{max} may not be significant, especially given the high-amplitude, high-frequency periodicity noted in the Elmer-Tipton tornado, but additional studies may be needed to determine this.

Finally, the opportunities for future work are numerous. Myriad datasets collected by the MWR-05XP and RaXPol from previous tornadic supercell cases have yet to be examined, and RaXPol continues to collect data annually. These cases must be analyzed to lend credence to the behaviors and phenomena found in this study. In addition, constructing vertical cross-sections of reflectivity for the cases in this study, as well as any new cases, would help illuminate additional characteristics of each supercell that may have impacted the tornado life cycle, including descending reflectivity cores (Rasmussen et al. 2006) and bursts of precipitation in the forward flank (Bluestein et al. 2019). Polarimetric variables for the cases captured by RaXPol should also be studied in greater depth for evidence of updrafts, how debris impacts the tornadic vortex, and more.

Bibliography

Archive SPC Mesoscale Analysis (HTML5 JavaScript Version). https://www.spc.noaa.gov/exper/ma_archive/ (Accessed May 1, 2021).

Damage Assessment Toolkit. https://apps.dat.noaa.gov/StormDamage/DamageViewer/ (Accessed May 1, 2021).

SPC Severe Weather Events Archive. *Storm Prediction Center*. https://www.spc.noaa.gov/exper/archive/events/ (Accessed May 1, 2021).

Adlerman, E. J., and K. K. Droegemeier, 2005: The dependence of numerically simulated cyclic mesocyclogenesis upon environmental vertical wind shear. *Mon. Wea. Rev.*, **133**, 3595–3623.

Alexander, C. R., 2010: A mobile radar based climatology of supercell tornado structures and dynamics. https://hdl.handle.net/11244/319059 (Accessed May 1, 2021).

Alexander, C. R., and J. M. Wurman, 2008: 24th Conf. on Severe Local Storms. *Updated mobile radar climatology of supercell tornado structures and dynamics*, Savannah, GA, Amer. Meteor. Soc.

Alexander, C. R., and J. Wurman, 2005: The 30 May 1998 Spencer, South Dakota, storm. Part I: The structural evolution and environment of the tornadoes. *Mon. Wea. Rev.*, **133**, 72–97.

Ashley, W. S., 2007: Spatial and temporal analysis of tornado fatalities in the United States: 1880–2005. *Weather and Forecasting*, **22**, 1214–1228.

Barnes, S. L., 1978: Oklahoma thunderstorms on 29–30 April 1970. Part I: Morphology of a tornadic storm. *Mon. Wea. Rev.*, **106**, 673–684.

Bluestein, H. B., 4th European Conf. on Severe Storms. *Mobile Doppler radar observations of tornadoes*, Trieste, Italy.

Bluestein, H. B., A. L. Pazmany, J. C. Galloway, and R. E. Mcintosh, 1995: Studies of the substructure of severe convective storms using a mobile 3-mm-wavelength Doppler radar. *Bull. Amer. Meteor. Soc.*, **76**, 2155–2169.

Bluestein, H. B., and S. G. Gaddy, 2001: Airborne pseudo-dual-doppler analysis of a rear-inflow jet and deep convergence zone within a supercell. *Mon. Wea. Rev.*, **129**, 2270–2289.

Bluestein, H. B., and A. L. Pazmany, 2000: Observations of tornadoes and other convective phenomena with a mobile, 3–mm wavelength, Doppler radar: The spring 1999 field experiment. *Bull. Amer. Meteor. Soc.*, **81**, 2939–2951.

Bluestein, H. B., and Coauthors, 2010: A summary of data collected during VORTEX-2 by MWR-05XP/TWOLF, UMass X-Pol, and the UMass W-band radar. *25th Conf. on Severe Local Storms*, Denver, CO, Amer. Meteor. Soc.

Bluestein, H. B., and W. P. Unruh, 1989: Observations of the wind field in tornadoes, funnel clouds, and wall clouds with a portable Doppler radar. *Bull. Amer. Meteor. Soc.*, **70**, 1514–1525.

Bluestein, H. B., C. C. Weiss, and A. L. Pazmany, 2003: Mobile Doppler radar observations of a tornado in a supercell near Bassett, Nebraska, on 5 June 1999. Part I: Tornadogenesis. *Mon. Wea. Rev.*, **131**, 2954–2967.

Bluestein, H. B., C. C. Weiss, and A. L. Pazmany, 2004: Doppler radar observations of dust devils in Texas. *Mon. Wea. Rev.*, **132**, 209–224.

Bluestein, H. B., C. C. Weiss, and A. L. Pazmany, 2004: The vertical structure of a tornado near Happy, Texas, on 5 May 2002: High-resolution, mobile, W-band, Doppler radar observations. *Mon. Wea. Rev.*, **132**, 2325–2337.

Bluestein, H. B., C. C. Weiss, M. M. French, E. M. Holthaus, R. L. Tanamachi, S. Frasier, and A. L. Pazmany, 2007: The structure of tornadoes near Attica, Kansas, on 12 May 2004: High-resolution, mobile, Doppler radar observations. *Mon. Wea. Rev.*, **135**, 475–506.

Bluestein, H. B., J. C. Snyder, and J. B. Houser, 2015: A multiscale overview of the El Reno, Oklahoma, tornadic supercell of 31 May 2013. *Wea. Forecasting*, **30**, 525–552.

Bluestein, H. B., J. G. Ladue, H. Stein, D. Speheger, and W. P. Unruh, 1993: Doppler Radar Wind Spectra of Supercell Tornadoes. *Mon. Wea. Rev.*, **121**, 2200–2222.

Bluestein, H. B., K. J. Thiem, J. C. Snyder, and J. B. Houser, 2019: Tornadogenesis and early tornado evolution in the El Reno, Oklahoma, supercell on 31 May 2013. *Mon. Wea. Rev.*, **147**, 2045–2066.

Bluestein, H. B., M. M. French, I. PopStefanija, R. T. Bluth, and J. B. Knorr, 2010: A mobile, phased-array Doppler radar for the study of severe convective storms. *Bull. Amer. Meteor. Soc.*, **91**, 579–600.

Bluestein, H. B., M. M. French, J. C. Snyder, and J. B. Houser, 2016: Doppler radar observations of anticyclonic tornadoes in cyclonically rotating, right-moving supercells. *Mon. Wea. Rev.*, **144**, 1591–1616.

Bluestein, H. B., M. M. French, R. L. Tanamachi, S. Frasier, K. Hardwick, F. Junyent, and A. L. Pazmany, 2007: Close-range observations of tornadoes in supercells made with a dual-polarization, X-band, mobile Doppler radar. *Mon. Wea. Rev.*, **135**, 1522–1543.

Bluestein, H. B., S. G. Gaddy, D. C. Dowell, A. L. Pazmany, J. C. Galloway, R. E. McIntosh, and H. Stein, 1997: Doppler radar observations of substorm-scale vortices in a supercell. *Mon. Wea. Rev.*, **125**, 1046–1059.

Bodine, D. J., M. R. Kumjian, R. D. Palmer, P. L. Heinselman, and A. V. Ryzhkov, 2013: Tornado damage estimation using polarimetric radar. *Wea. Forecasting*, **28**, 139–158.

Brandes, E. A., 1981: Finestructure of the Del City-Edmond tornadic mesocirculation. *Mon. Wea. Rev.*, **109**, 635–647.

Brooks, H. E., and C. A. Doswell, 2001: Normalized damage from major tornadoes in the United States: 1890–1999. *Wea. Forecasting*, **16**, 168–176.

Brown, R. A., L. R. Lemon, and D. W. Burgess, 1978: Tornado detection by pulsed Doppler radar. *Mon. Wea. Rev.*, **106**, 29–38.

Burgess, D. W., L. R. Lemon, and R. A. Brown, 1975: Tornado characteristics revealed by Doppler radar. *Geophys. Res. Lett.*, **2**, 183–184.

Burgess, D. W., M. A. Magsig, J. Wurman, D. C. Dowell, and Y. Richardson, 2002: Radar observations of the 3 May 1999 Oklahoma City tornado. *Wea. Forecasting*, **17**, 456–471.

Byko, Z., P. Markowski, Y. Richardson, J. Wurman, and E. Adlerman, 2009: Descending reflectivity cores in supercell thunderstorms observed by mobile radars and in a high-resolution numerical simulation. *Wea. Forecasting*, **24**, 155–186.

Davies, J. M., and A. Fischer, 2009: Environmental characteristics associated with nighttime tornadoes. *Electronic J. Operational Meteor.*, **EJ3**, 1–29.

Davies-Jones, R., 1984: Streamwise vorticity: the origin of updraft rotation in supercell storms. *J. Atmos. Sci.*, **41**, 2991–3006.

Dawson, D. T., E. R. Mansell, Y. Jung, L. J. Wicker, M. R. Kumjian, and M. Xue, 2014: Low-level ZDR signatures in supercell forward flanks: the role of size sorting and melting of hail. *J. Atmos. Sci.*, **71**, 276–299.

Dennis, E. J., and M. R. Kumjian, 2017: The impact of vertical wind shear on hail growth in simulated supercells. *J. Atmos. Sci.*, **74**, 641–663.

Doswell, C. A., 1998: 14th Conf. Hydrology. *Seeing supercells as heavy rain producers*, Dallas, TX, Amer. Meteor. Soc..

Doviak, R. J., and Zrnić Dušan S., 2014: *Doppler radar and weather observations*. Academic Press, Inc.

Dowell, D. C., and H. B. Bluestein, 2002: The 8 June 1995 McLean, Texas, storm. Part II: cyclic tornado formation, maintenance, and dissipation. *Mon. Wea. Rev.*, **130**, 2649–2670.

Dowell, D. C., C. R. Alexander, J. M. Wurman, and L. J. Wicker, 2005: Centrifuging of hydrometeors and debris in tornadoes: radar-reflectivity patterns and wind-measurement errors. *Mon. Wea. Rev.*, **133**, 1501–1524.

Fiedler, B. H., 1998: Wind-speed limits in numerically simulated tornadoes with suction vortices. *Q. J. R. Meteor. Soc.*, **124**, 2377–2392.

Finley, C. A., and B. D. Lee, 2004: High resolution mobile mesonet observations of RFD surges in the June 9 Basset, Nebraska supercell during Project ANSWERS 2003. *22nd Conf. on Severe Local Storms*, Hyannis, MA, Amer. Meteor. Soc..

Finley, C. A., and B. D. Lee, 2008: Mobile mesonet observations of an intense RFD and multiple RFD gust fronts in the May 23 Quinter, Kansas tornadic supercell during TWISTEX 2008. *24th Conf. on Severe Local Storms*, Savannah, GA, Amer. Meteor. Soc.

French, M. M., H. B. Bluestein, I. PopStefanija, C. A. Baldi, and R. T. Bluth, 2013: Reexamining the vertical development of tornadic vortex signatures in supercells. *Mon. Wea. Rev.*, **141**, 4576–4601.

French, M. M., H. B. Bluestein, I. PopStefanija, C. A. Baldi, and R. T. Bluth, 2014: Mobile, phased-array, Doppler radar observations of tornadoes at X band. *Mon. Wea. Rev.*, **142**, 1010–1036.

Frost, K., H. B. Bluestein, J. McLintock, Z. B. Wienhoff, K. J. Thiem, and D. W. Reif, 2018: Tornadogensis in a supercell near the northwest Texas – southwestern Oklahoma border on 16 May 2015: A comparison of the evolution of vortex shear signatures from two nearby, mobile, rapid-scan, X-band, Doppler radars. Poster 176, *29th Conf. on Severe Local Storms*, Stowe, VT, 25 Oct. 2018.

Fujita, T. T., 1981: Tornadoes and downbursts in the context of generalized planetary scales. *J. Atmos. Sci.*, **38**, 1511–1534.

Fujita, T., 1958: Mesoanalysis of the Illinois tornadoes of 9 April 1953. *J. Meteor.*, **15**, 288–296.

Fujiwhara, S., 1931: Short note on the behavior of two vortices. *Proc. Phys.-Math. Soc. Japan*, **13**, 106–110.

Golden, J. H., and D. Purcell, 1977: Photogrammetric velocities for the Great Bend, Kansas, tornado of 30 August 1974: accelerations and asymmetries. *Mon. Wea. Rev.*, **105**, 485–492.

Grams, J. S., R. L. Thompson, D. V. Snively, J. A. Prentice, G. M. Hodges, and L. J. Reames, 2012: A climatology and comparison of parameters for significant tornado events in the United States. *Wea. Forecasting*, **27**, 106–123.

Grazulis, T. P., 1993: *Significant tornadoes, 1680-1991*. Environmental Films, St. Johnsbury, VT.

Grazulis, T. P., 2001: *The tornado: nature's ultimate windstorm*. University of Oklahoma Press, Norman, OK.

Griffin, C. B., C. C. Weiss, A. E. Reinhart, J. C. Snyder, H. B. Bluestein, J. Wurman, and K. A. Kosiba, 2018: In situ and radar observations of the low reflectivity ribbon in supercells during VORTEX2. *Mon. Wea. Rev.*, **146**, 307–327.

Griffin, C. B., D. J. Bodine, J. M. Kurdzo, A. Mahre, and R. D. Palmer, 2019: High-temporal resolution observations of the 27 May 2015 Canadian, Texas, tornado using the Atmospheric Imaging Radar. *Mon. Wea. Rev.*, **147**, 873–891.

Gunturi, P., and M. Tippett, 2017: Impact of ENSO on U.S. tornado and hail frequencies. *WillisRe*, March.

Hastings, R., and Y. Richardson, 2016: Long-term morphological changes in simulated supercells following mergers with nascent supercells in directionally varying shear. *Mon. Wea. Rev.*, **144**, 471–499.

Houser, J. L., H. B. Bluestein, and J. C. Snyder, 2015: Rapid-scan, polarimetric, Doppler radar observations of tornadogenesis and tornado dissipation in a tornadic supercell: the "El Reno, Oklahoma" storm of 24 May 2011. *Mon. Wea. Rev.*, **143**, 2685–2710.

Houser, J. L., H. B. Bluestein, and J. C. Snyder, 2016: A finescale radar examination of the tornadic debris signature and weak-echo reflectivity band associated with a large, violent tornado. *Mon. Wea. Rev.*, **144**, 4101–4130.

Kennedy, A., J. M. Straka, and E. N. Rasmussen, 2007: A statistical study of the association of DRCs with supercells and tornadoes. *Wea. Forecasting*, **22**, 1191–1199.

Klemp, J. B., 1987: Dynamics of tornadic thunderstorms. *Annu. Rev. Fluid Mech.*, **19**, 369–402.

Klemp, J. B., and R. Rotunno, 1983: A study of the tornadic region within a supercell thunderstorm. *J. Atmos. Sci.*, **40**, 359–377.

Klemp, J. B., R. B. Wilhelmson, and P. S. Ray, 1981: Observed and numerically simulated structure of a mature supercell thunderstorm. *J. Atmos. Sci.*, **38**, 1558–1580.

Kosiba, K., J. Wurman, Y. Richardson, P. Markowski, P. Robinson, and J. Marquis, 2013: Genesis of the Goshen County, Wyoming, tornado on 5 June 2009 during VORTEX2. *Mon. Wea. Rev.*, **141**, 1157–1181.

Krasny, R., 1993: Vortex sheet roll-up. *RIMS Workshop on Unstable and Turbulent Motion of Fluid*, Kyoto, Japan, S. Kida, Ed., World Scientific, 43–49.

Kumjian, M. R., 2013: Principles and applications of dual-polarization weather radar. Part I: Description of the polarimetric radar variables. *J. Oper. Meteor.*, **1**, 226–242.

Kumjian, M. R., and A. V. Ryzhkov, 2008: Polarimetric signatures in supercell thunderstorms. *J. Appl. Meteor. Climatol.*, **47**, 1940–1961.

Kumjian, M., and A. Ryzhkov, 2007: Polarimetric characteristics of tornadic and nontornadic supercell thunderstorms. *33rd Conf. on Radar Meteorology*, Cairns, Australia, Amer. Meteor. Soc.

Kundu, P. K., I. M. Cohen, and D. R. Dowling, 2012: *Fluid mechanics*. 5th ed. Elsevier, Amsterdam.

Lakshmanan, V., and A. Witt, 1996: Detection of bounded weak echo regions in meteorological radar images. *Proc. 13th Int. Conf. on Pattern Recognition*, Vienna, Austria, Institute of Electrical and Electronics Engineers.

Lee, B. D., C. A. Finley, and C. D. Karstens, 2012: The Bowdle, South Dakota, cyclic tornadic supercell of 22 May 2010: surface analysis of rear-flank downdraft evolution and multiple internal surges. *Mon. Wea. Rev.*, **140**, 3419–3441.

Lee, W.-C., and J. Wurman, 2005: Diagnosed three-dimensional axisymmetric structure of the Mulhall tornado on 3 May 1999. *J. Atmos. Sci.*, **62**, 2373–2393.

Lemon, L. R., and D. W. Burgess, 1993: Supercell associated deep convergence zone revealed by a WSR-88D. Preprints, *26th Conf. on Radar Meteorology,* Norman, OK, Amer. Meteor. Soc., 206– 208.

Lemon, L. R., and C. A. Doswell, 1979: Severe thunderstorm evolution and mesocyclone structure as related to tornadogenesis. *Mon. Wea. Rev.*, **107**, 1184–1197.

Lemon, L. R., and S. Parker, 1996: The Lahoma storm deep convergence zone: its characteristics and role in storm dynamics and severity. *18th Conference on Severe Local Storms*, San Francisco, CA, Amer. Meteor. Soc., 70–75.

Leslie, L. M., 1971: The development of concentrated vortices: a numerical study. *J. Fluid Mech.*, **48**, 1–21.

Lewellen, D. C., B. Gong, and W. S. Lewellen, 2008: Effects of finescale debris on near-surface tornado dynamics. *J. Atmos. Sci.*, **65**, 3247–3262.

Mahre, A., J. M. Kurdzo, D. J. Bodine, C. B. Griffin, R. D. Palmer, and T.-Y. Yu, 2018: Analysis of the 16 May 2015 Tipton, Oklahoma, EF-3 tornado at high spatiotemporal resolution using the Atmospheric Imaging Radar. *Mon. Wea. Rev.*, **146**, 2103–2124.

Markowski, P. M., and Y. P. Richardson, 2009: Tornadogenesis: Our current understanding, forecasting considerations, and questions to guide future research. *Atmos. Res.*, **93**, 3–10.

Markowski, P., and Coauthors, 2012: The pretornadic phase of the Goshen County, Wyoming, supercell of 5 June 2009 intercepted by VORTEX2. Part I: Evolution of kinematic and surface thermodynamic fields. *Mon. Wea. Rev.*, **140**, 2887–2915.

Markowski, P., and Coauthors, 2012: The pretornadic phase of the Goshen County, Wyoming, supercell of 5 June 2009 intercepted by VORTEX2. Part II: Intensification of low-level rotation. *Mon. Wea. Rev.*, **140**, 2916–2938.

Marquis, J. N., Y. P. Richardson, and J. M. Wurman, 2007: Kinematic observations of misocyclones along boundaries during IHOP. *Mon. Wea. Rev.*, **135**, 1749–1768.

Marquis, J., Y. Richardson, J. Wurman, and P. Markowski, 2008: Single- and dual-Doppler analysis of a tornadic vortex and surrounding storm-scale flow in the Crowell, Texas, supercell of 30 April 2000. *Mon. Wea. Rev.*, **136**, 5017–5043.

Marquis, J., Y. Richardson, P. Markowski, D. Dowell, and J. Wurman, 2012: Tornado maintenance investigated with high-resolution dual-Doppler and EnKF analysis. *Mon. Wea. Rev.*, **140**, 3–27.

Marquis, J., Y. Richardson, P. Markowski, J. Wurman, K. Kosiba, and P. Robinson, 2016: An investigation of the Goshen County, Wyoming, tornadic supercell of 5 June 2009 using EnKF assimilation of mobile mesonet and radar observations collected during VORTEX2. Part II: Mesocyclone-scale processes affecting tornado formation, maintenance, and decay. *Mon. Wea. Rev.*, **144**, 3441–3463.

Marwitz, J. D., 1972: The structure and motion of severe hailstorms. Part III: Severely sheared storms. *J. Appl. Meteor.*, **11**, 189–201.

Mashiko, W., 2016: A numerical study of the 6 May 2012 Tsukuba City supercell tornado. Part II: Mechanisms of tornadogenesis. *Mon. Wea. Rev.*, **144**, 3077–3098.

McKeown, K. E., M. M. French, K. S. Tuftedal, D. M. Kingfield, H. B. Bluestein, D. W. Reif, and Z. B. Wienhoff, 2020: Rapid-scan and polarimetric radar observations of the dissipation of a violent tornado on 9 May 2016 near Sulphur, Oklahoma. *Mon. Wea. Rev.*, **148**, 3951–3971.

Moller, A. R., 1978: The improved NWS storm spotters' training program at Ft. Worth, Tex. *Bull. Amer. Meteor. Soc.*, **59**, 1574–1582.

Nelson, S. P., and R. R. Braham, 1975: Detailed observational study of a weak echo region. *Pure Appl. Geophys.*, **113**, 735–746.

Nixon, C., 2021: Case Archive. *ustornadoes.com*. https://www.ustornadoes.com/case-archive/ (Accessed July 5, 2021).

NWS Norman, 2015: *Tornado table for the severe weather and flash flood event of May 6, 2015*. https://www.weather.gov/oun/events-20150506-tornadotable (Accessed July 3, 2021).

NWS Norman, 2019: *2019 Oklahoma Tornadoes*. https://www.weather.gov/oun/tornadodata-ok-2019 (Accessed May 1, 2021).

Oye, R., C. Mueller, and S. Smith, 1995: Software for radar translation, visualization, editing, and interpolation. *Preprints, 27th Conf. on Radar Meteor.*, Vail, CO, Amer. Meteor. Soc., 359–361.

Palmer, R. D., and Coauthors, 2011: Observations of the 10 May 2010 tornado outbreak using OU-PRIME: Potential for new science with high-resolution polarimetric radar. *Bull. Amer. Meteor. Soc.*, **92**, 871–891.

Pazmany, A. L., J. B. Mead, H. B. Bluestein, J. C. Snyder, and J. B. Houser, 2013: A mobile rapid-scanning X-band polarimetric (RaXPol) Doppler radar system. *J. Atmos. Oceanic Technol.*, **30**, 1398–1413.

Perez, A. H., L. J. Wicker, and R. E. Orville, 1997: Characteristics of cloud-to-ground lightning associated with violent tornadoes. *Wea. Forecasting*, **12**, 428–437.

Prasad, A., A. Manmohan, P. K. Shanmugam, and D. P. Kothari, 2018: Application of cubic spline interpolation technique in power systems: A review. *Topics in splines and applications*, Y.K.-N. Truong and M. Sarfraz, Eds., IntechOpen, London.

Rasmussen, E. N., 2003: Refined supercell and tornado forecast parameters. *Wea. Forecasting*, **18**, 530–535.

Rasmussen, E. N., and D. O. Blanchard, 1998: A baseline climatology of sounding-derived supercell and tornado forecast parameters. *Wea. Forecasting*, **13**, 1148–1164.

Rasmussen, E. N., J. M. Straka, M. S. Gilmore, and R. Davies-Jones, 2006: A preliminary survey of rear-flank descending reflectivity cores in supercell storms. *Wea. Forecasting*, **21**, 923–938.

Rasmussen, E. N., J. M. Straka, R. Davies-Jones, C. A. Doswell, F. H. Carr, M. D. Eilts, and D. R. MacGorman, 1994: Verification of the Origins of Rotation in Tornadoes Experiment: VORTEX. *Bull. Amer. Meteor. Soc.*, **75**, 995–1006.

Rotunno, R., and J. Klemp, 1985: On the rotation and propagation of simulated supercell thunderstorms. *J. Atmos. Sci.*, **42**, 271–292.

Ryzhkov, A. V., T. J. Schuur, D. W. Burgess, and D. S. Zrnic, 2005: Polarimetric tornado detection. *J. Appl. Meteor.*, **44**, 557–570.

Ryzhkov, A., D. Burgess, D. Zrnic, T. Smith, and S. Giangrande, 2002: Polarimetric analysis of a 3 May 1999 tornado. *21st Conf. on Severe Local Storms*, San Antonio, TX, Amer. Meteor. Soc.

Sanders, F., and C. A. Doswell, 1995: A case for detailed surface analysis. *Bull. Amer. Meteor. Soc.*, **76**, 505–521.

Sandifer, J. B., 2005: Meteorological measurements with a MWR-05XP phased array radar. Naval Postgraduate School.

Schenkman, A. D., M. Xue, and A. Shapiro, 2012: Tornadogenesis in a simulated mesovortex within a mesoscale convective system. *J. Atmos. Sci.*, **69**, 3372–3390.

Schenkman, A. D., M. Xue, and M. Hu, 2014: Tornadogenesis in a high-resolution simulation of the 8 May 2003 Oklahoma City supercell. *J. Atmos. Sci.*, **71**, 130–154.

Schultz, C.J., L.D. Carey, E.V. Schultz, B.C. Carcione, C.B. Darden, C.C. Crowe, P.N. Gatlin, D.J. Nadler, W.A. Petersen, and K.R. Knupp, 2012: Dual-polarization tornadic debris signatures part I: Examples and utility in an operational setting. *Electronic J. Operational Meteor.*, **13 (9)**, 120−137.

Shapiro, A., 2001: A centrifugal wave solution of the Euler and Navier-Stokes equations. *Zeitschrift für angewandte Mathematik und Physik*, **52**, 913–923.

Skinner, P. S., C. C. Weiss, M. M. French, H. B. Bluestein, P. M. Markowski, and Y. P. Richardson, 2014: VORTEX2 observations of a low-level mesocyclone with multiple internal rear-flank downdraft momentum surges in the 18 May 2010 Dumas, Texas, supercell. *Mon. Wea. Rev.*, **142**, 2935–2960.

Snyder, J. C., 2013: Observations and simulations of polarimetric, X-band radar signatures in supercells. University of Oklahoma.

Snyder, J. C., and H. B. Bluestein, 2014: Some considerations for the use of high-resolution mobile radar data in tornado intensity determination. *Wea. Forecasting*, **29**, 799–827.

Snyder, J. C., H. B. Bluestein, G. Zhang, and S. J. Frasier, 2010: Attenuation correction and hydrometeor classification of high-resolution, X-band, dual-polarized mobile radar measurements in severe convective storms. *J. Atmos. Oceanic Technol.*, **27**, 1979–2001.

Snyder, J. C., H. B. Bluestein, V. Venkatesh, and S. J. Frasier, 2013: Observations of polarimetric signatures in supercells by an X-band mobile Doppler radar. *Mon. Wea. Rev.*, **141**, 3–29.

Snyder, J. C., H. B. Bluestein, Y. Jung, S. Frasier, and V. Venkatesh, 2010: The structure and time evolution of polarimetric signatures in severe convective storms: High-resolution numerical simulations and data from a mobile, X-band Doppler radar. *25th Conf. on Severe Local Storms*, Denver, CO, Amer. Meteor. Soc.

Snyder, J. C., H. B. Bluestein, Z. B. Wienhoff, C. M. Kuster, and D. W. Reif, 2020: An analysis of an ostensible anticyclonic tornado from 9 May 2016 using high-resolution, rapid-scan radar data. *Wea. Forecasting*, **35**, 1685–1712.

Snyder, J. C., J. L. Salazar-Cerreno, H. B. Bluestein, N. A. Aboserwal, R. D. Palmer, and T. Y. Yu, 2015: Examining the effects of the ground on the radiation pattern of a parabolic reflector at very low elevation angles. *37th Conf. on Radar Meteorology*, Norman, OK, Amer. Meteor. Soc.

Speheger, D. A., C. A. Doswell, and G. J. Stumpf, 2002: The tornadoes of 3 May 1999: Event verification in central Oklahoma and related issues. *Wea. Forecasting*, **17**, 362–381.

Straka, J. M., E. N. Rasmussen, R. P. Davies-Jones, and P. M. Markowski, 2007: An observational and idealized numerical examination of low-level counter-rotating vortices in the rear flank of supercells. *Electronic J. Severe Storms Meteor.*, **2 (8)**, 1–22.

Tanamachi, R. L., H. B. Bluestein, J. B. Houser, S. J. Frasier, and K. M. Hardwick, 2012: Mobile, X-band, polarimetric Doppler radar observations of the 4 May 2007 Greensburg, Kansas, tornadic supercell. *Mon. Wea. Rev.*, **140**, 2103–2125.

Tanamachi, R. L., H. B. Bluestein, M. Xue, W.-C. Lee, K. A. Orzel, S. J. Frasier, and R. M. Wakimoto, 2013: Near-surface vortex structure in a tornado and in a sub-tornado-strength convective-storm vortex observed by a mobile, W-band radar during VORTEX2. *Mon. Wea. Rev.*, **141**, 3661–3690.

Trapp, R. J., and R. Davies-Jones, 1997: Tornadogenesis with and without a dynamic pipe effect. *J. Atmos. Sci.*, **54**, 113–133.

Trapp, R. J., E. D. Mitchell, G. A. Tipton, D. W. Effertz, A. I. Watson, D. L. Andra, and M. A. Magsig, 1999: Descending and nondescending tornadic vortex signatures detected by WSR-88Ds. *Wea. Forecasting*, **14**, 625–639.

Trapp, R. J., G. J. Stumpf, and K. L. Manross, 2005: A reassessment of the percentage of tornadic mesocyclones. *Wea. Forecasting*, **20**, 680–687.

Wakimoto, R. M., and B. E. Martner, 1992: Observations of a Colorado tornado. Part II: Combined photogrammetric and Doppler radar analysis. *Mon. Wea. Rev.*, **120**, 522–543.

Wakimoto, R. M., and Coauthors, 2016: Aerial damage survey of the 2013 El Reno tornado combined with mobile radar data. *Mon. Wea. Rev.*, **144**, 1749–1776.

Wakimoto, R. M., and N. T. Atkins, 1996: Observations on the origins of rotation: The Newcastle tornado during VORTEX 94. *Mon. Wea. Rev.*, **124**, 384–407.

Wakimoto, R. M., W.-C. Lee, H. B. Bluestein, C.-H. Liu, and P. H. Hildebrand, 1996: ELDORA observations during VORTEX 95. *Bull. Amer. Meteor. Soc.*, **77**, 1465–1481.

Wakimoto, R. M., Z. Wienhoff, H. B. Bluestein, D. J. Bodine, and J. M. Kurdzo, 2020: Mobile radar observations of the evolving debris field compared with a damage survey of the Shawnee, Oklahoma, tornado of 19 May 2013. *Mon. Wea. Rev.*, **148**, 1779–1803.

Wicker, L. J., and R. B. Wilhelmson, 1995: Simulation and analysis of tornado development and decay within a three-dimensional supercell thunderstorm. *J. Atmos. Sci.*, **52**, 2675–2703.

Wienhoff, Z. B., 2016: Doppler radar analyses of tornadic supercells on 19 May 2013. University of Oklahoma.

Wienhoff, Z. B., H. B. Bluestein, D. W. Reif, R. M. Wakimoto, L. J. Wicker, and J. M. Kurdzo, 2020: Analysis of debris signature characteristics and evolution in the 24 May 2016 Dodge City, Kansas, tornadoes. *Mon. Wea. Rev.*, **148**, 5063–5086.

Wilson, M. B., 2019: An analysis of differential reflectivity arc characteristics in 109 supercell storms. University of Nebraska.

Wurman, J., 2002: The multiple-vortex structure of a tornado. *Wea. Forecasting*, **17**, 473–505.

Wurman, J., and C. R. Alexander, 2005: The 30 May 1998 Spencer, South Dakota, storm. Part II: Comparison of observed damage and radar-derived winds in the tornadoes. *Mon. Wea. Rev.*, **133**, 97–119.

Wurman, J., and S. Gill, 2000: Finescale radar observations of the Dimmitt, Texas (2 June 1995), tornado. *Mon. Wea. Rev.*, **128**, 2135–2164.

Wurman, J., C. Alexander, P. Robinson, and Y. Richardson, 2007: Low-level winds in tornadoes and potential catastrophic tornado impacts in urban areas. *Bull. Amer. Meteor. Soc.*, **89**, 31–46.

Wurman, J., D. Dowell, Y. Richardson, P. Markowski, E. Rasmussen, D. Burgess, L. Wicker, and H. B. Bluestein, 2012: The Second Verification of the Origins of Rotation in Tornadoes Experiment: VORTEX2. *Bull. Amer. Meteor. Soc.*, **93**, 1147–1170.

Wurman, J., J. M. Straka, and E. N. Rasmussen, 1996: Fine-scale Doppler radar observations of tornadoes. *Science*, **272**, 1774–1777.

Wurman, J., J. Straka, E. Rasmussen, M. Randall, and A. Zahrai, 1997: Design and deployment of a portable, pencil-beam, pulsed, 3-cm Doppler radar. *J. Atmos. Oceanic Technol.*, **14**, 1502–1512.

Wurman, J., K. Kosiba, and P. Robinson, 2013: In situ, Doppler radar, and video observations of the interior structure of a tornado and the wind–damage relationship. *Bull. Amer. Meteor. Soc.*, **94**, 835–846.

Yao, D., Z. Meng, and M. Xue, 2019: Genesis, maintenance and demise of a simulated tornado and the evolution of its preceding descending reflectivity core (DRC). *Atmosphere*, **10**, 1–18.

Yu, T.-Y., Y. Wang, A. Shapiro, M. B. Yeary, D. S. Zrnić, and R. J. Doviak, 2007: Characterization of tornado spectral signatures using higher-order spectra. *J. Atmos. Oceanic Technol.*, **24**, 1997–2013.

Zrnic, D. S., and A. V. Ryzhkov, 1999: Polarimetry for weather surveillance radars. *Bull. Amer. Meteor. Soc.*, **80**, 389–406.

Zrnic, D. S., and Coauthors, 2007: Agile-beam phased array radar for weather observations. *Bull. Amer. Meteor. Soc.*, **88**, 1753–1766.

Zrnić, D., D. W. Burgess, and L. Hennington, 1985: Doppler spectra and estimated windspeed of a violent tornado. *J. Climate Appl. Meteor.*, **24**, 1068–1081.